國立臺灣大學 生命科學學院 生化科學研究所

博士論文

Institute of Biochemical Sciences

College of Life Sciences

National Taiwan University

Doctoral Dissertation

1-(4-(芳基乙烯羰基)苯基)-4-羧基-2-吡咯烷酮作為有效抗病毒和抗菌劑的合成、評估和機制

Synthesis, evaluation, and mechanism of 1-(4-(arylethylenyl carbonyl) phenyl)-4-carboxy-2-pyrrolidinones as potent antiviral and antibacterial agents

許寧

Srinivasa Rao Palla

指導教授: 梁博煌 博士

Advisor: Prof. Po-Huang Liang Ph.D.

中華民國 113 年 1 月

January, 2024

doi:10.6342/NTU202400256

Acknowledgment

Starting with the name of Vigneshwara, the most gracious, the most merciful...!!

I would like to thank my supervisor Prof. Po-Huang Liang for his amiable support and inspiration; I express my appreciation for his patience, invaluable advice, and persistent support during my Ph.D. research. His in-depth knowledge, experience, and awareness of modern-day requirements have encouraged me to pursue my research projects confidently. I wish to feel gratitude to all my collaborators, particularly Prof. Sui-Yuan Chang, Prof. Lily Hui-Ching Wang, and Prof. Chih-Jung Kuo for their biological studies and technical support. I would also like to thank TIGP staff members, especially Ms. Vicki, for her administrative support, and all my friends and lab-mates for their untiring motivation and consultation. Finally, I dedicate my Ph.D. thesis-dissertation to my family, including my father, mother, wife, and daughter, siblings, for believing in my skills and ability to pursue higher goals in life. Thanks to all of you for giving me support, encouragement, unconditional love, prayers, and guidance; you were all a source of inspiration and encouragement during this journey.

doi:10.6342/NTU202400256

Table of Contents

doi:10.6342/NTU202400256

doi:10.6342/NTU202400256

doi:10.6342/NTU202400256

Abbreviations

CoV	Coronavirus
COVID-19	Coronavirus disease 2019
SARS-CoV-2	Severe acute respiratory syndrome coronavirus 2
TMPRSS2	Transmembrane protease, serine 2
MERS	Middle East respiratory syndrome
SAR	Structure-activity relationship
ACE2	Angiotensin-converting enzyme 2
RBD	Receptor-binding domain
IPTG	Isopropyl β-d-1-thiogalactopyranoside
Ni-NTA	Nickel-nitrilotriacetic acid
$3CL^{pro}$	3C-like proteinase
PL^{pro}	Papain-like protease
RdRp	RNA-dependent RNA polymerase
MRSA	Methicillin-resistant *Staphylococcus aureus*
MSSA	Methicillin-sensitive *Staphylococcus aureus*
TLC	Thin-layer chromatography

doi:10.6342/NTU202400256

TMS	Tetramethylsilane
DMSO	dimethyl sulfoxide;
EC_{50}	Half maximal effective concentration
EcUPPS	Escherichia coli undecaprenyl pyrophosphate synthase
EtBr	ethidium bromide
FPP	farnesyl pyrophosphate
IPP	isopentenyl pyrophosphate
UPP	undecaprenyl pyrophosphate
UPPS	undecaprenyl pyrophosphate synthase
Hepes	4-2(-hydroxyethyl)-1-piperazineethanesulfonic acid
IC_{50}	half maximal inhibitory concentration
IPTG	isopropyl-β-thiogalactopyranoside
MANT-O-GPP	(2E,6E)-8-O-(N-methyl-2-aminobenzoyl)-3,7-dimethyl-2,6-octandien-1-pyrophosphate
mp	melting temperature
MRSA	methicillin-resistant Staphylococcus aureus
Ni-NTA	nickel nitrilo-tri-acetic acid
NMR	nuclear magnetic resonance
PCR	polymerase chain reaction
SaUPPS	Staphylococcus aureus undecaprenyl pyrophosphate synthase
SDS-PAGE	sodium dodecyl sulfate-polyacrylamide gel electrophoresis
TLC	thin-layer chromatography
Tris	tris(hydroxymethyl)aminomethane

doi:10.6342/NTU202400256

Part I

Synthesis, evaluation, and mechanism of 1-(4-(arylethylenylcarbonyl)phenyl)-4-carboxy-2-pyrrolidinones as potent reversible SARS-CoV-2 entry inhibitors

摘要

通過邁克爾加成、環化、醛醇縮合和去質子化設計並合成了一類**1-(4-(**芳基乙烯羰基**)**苯基**)-4-**羧基**-2-**吡咯烷酮，以抑制人跨膜蛋白酶絲氨酸**2 (TMPRSS2)**和弗林蛋白酶， 它們參與修飾 **SARS-CoV-2 Spike** 以便病毒進入。 發現最有效的抑制劑 **2f (81)** 可有效抑制 **VeroE6** 和 **Calu-3** 細胞中各種 **SARS-CoV-2 delta** 和 **omicron** 突變株的複製，通過與病毒預混合，抗病毒的**EC_{50}** 範圍可達 **0.001** 至 **0.026 μM**。 比蛋白酶抑制活性更有效的抗病毒活性顯示，合成的化合物主要以抑制 **Spike** 受體結合域（**RBD**）：血管緊張轉化酶 **2**（**ACE2**）相互作用作為靶標，並且通過抑制 **TMPRSS2** 和/或 **Furin** 增强其抗病毒活性。 為了進一步證實 **2f**（**81**）對病毒進入的阻斷作用，使用**SARS-CoV-2 Spike**假病毒進行進入檢測，結果表明該化合物通過**ACE2**依賴性途徑抑制假病毒進入，主要是抑制**Calu-3** 細胞中 **RBD**：**ACE2** 相互作用和 **TMPRSS2** 活性。 最後，在 **SARS-CoV-2** 感染的體內動物模型中，倉鼠口服 **25 mg/kg 2f (81)** 可減少體重減輕，感染三天後鼻甲中的病毒 **RNA** 水平降低了 **5** 倍。 我們的研究結果證明了先導化合物作為 **SARS-CoV-2** 治療進一步臨床前研究的潛力。

doi:10.6342/NTU202400256

Abstract

A class of 1-(4-(arylethylenylcarbonyl)phenyl)-4-carboxy-2-pyrrolidinones were designed and synthesized via Michael addition, cyclization, aldol condensation, and deprotonation to inhibit the human transmembrane protease serine 2 (TMPRSS2) and Furin, which are involved in priming the SARS-CoV-2 Spike for virus entry. The most potent inhibitor **2f** (**81**) was found to efficiently inhibit the replication of various SARS-CoV-2 delta and omicron variants in VeroE6 and Calu-3 cells, with EC_{50} range of 0.001 to 0.026 μM by pre-incubation with the virus to avoid the virus entry. The more potent antiviral activities than the proteases inhibitory activities led to the discovery that the synthesized compounds also inhibited Spike's receptor binding domain (RBD):angiotensin converting enzyme 2 (ACE2) interaction as a main target, and their antiviral activities were enhanced by inhibiting TMPRSS2 and/or Furin. To further confirm the blocking effect of **2f** (**81**) on virus entry, SARS-CoV-2 Spike pseudovirus was used in the entry assay and the results showed that the compound inhibited the pseudovirus entry in a ACE2-dependent pathway, via mainly inhibiting RBD:ACE2 interaction and TMPRSS2 activity in Calu-3 cells. Finally, in the *in vivo* animal model of SARS-CoV-2 infection, the oral administration of 25 mg/kg **2f** (**81**) in hamsters resulted in reduced body weight loss and 5-fold lower viral RNA levels in nasal turbinate three days post-infection. Our findings demonstrated the potential of the lead compound for further preclinical investigation as a potential treatment for SARS-CoV-2.

doi:10.6342/NTU202400256

1. Introduction

The coronavirus disease 2019 (COVID-19) was first reported in December 2019 (Huang et al., 2020; Wu et al., 2020; Zhu et al., 2020) has been declared a worldwide pandemic by the World Health Organization in March 2020 and is still ongoing causing an approximately 1% case mortality rate. The pathogen is the human severe acute respiratory syndrome-coronavirus-2 (SARS-CoV-2) that is highly similar (79.6% identity in the genome) to the previously (2002−2003) emerged SARS-CoV (Zhou et al., 2020; Lu et al., 2020). For infection, both SARS-CoV and SARS-CoV-2 utilize human angiotensin-converting enzyme 2 (ACE2) as the receptor to bind with the virus surface Spike glycoprotein through its receptor binding domain (RBD) located in the S1 domain (Jackson et al., 2022). After binding, the human protease Furin cleaves Spike at S1/S2 (P**R**RA**R**$_{685}$↓S) into two fragments S1 and S2. Then the human Type II transmembrane protease serine 2 (TMPRSS2) further cleaves S2 at KPS**KR**$_{815}$↓S, exposing the membrane fusion peptide and allowing the virus to fuse with the cell membrane for entry into the cell, where the virus replicates (Bestle et al., 2020; Essalmani et al., 2022). Alternatively, SARS-CoV-2 could enter the cell through the ACE2-mediated endocytosis and then the Spike protein could be cleaved by an endosomal human protease Cathepsin L to release the viral RNA into cytosol (Mondal et al., 2022). Therefore, RBD:ACE2 interaction, TMPRSS2, Furin, and Cathepsin L could serve as targets for inhibiting SARS-CoV-2 entry and infection.

Like SARS-CoV, SARS-CoV-2 is an enveloped, positive single-stranded RNA virus, belonging to β-CoVs. Their relatively large 29.7 kb genomes encode two polyproteins pp1a and pp1ab that can be processed into mature non-structural proteins

doi:10.6342/NTU202400256

(NSPs) to become functional by the virus-encoded proteases, 3C-like protease ($3CL^{pro}$) as homologous to the picornavirus 3C protease (also called main protease, M^{pro}) and papain-like protease (PL^{pro}). Both viral proteases are chymotrypsin-like but utilize Cys as a nucleophile for proteolysis. Mature NSPs, including NSP7, 8, 10, 12, 13, and 14 then form a replication-transcription complex with RNA-dependent RNA polymerase (RdRp), helicase, exonuclease etc. activities for making sub-genomic RNAs of the structural proteins, Envelop (E), Nucleocapsid (N), Membrane (M), and Spike (S) proteins, to be assembled with the (+)RNA into new virus particles (Kuo and Liang, 2015; de Wit et al., 2016). $3CL^{pro}$ and PL^{pro} cleave 11 and 3 sites on the polyproteins for maturation of NSP1−16 (Hsu et al., 2005; Kuo et al., 2022). Therefore, these two virus-encoded proteases are attractive drug targets and many drug discovery efforts have been made for developing covalent and non-covalent inhibitors (e.g. Kuo et al., 2021; Lee et al., 2021). Covalent peptidomimetic inhibitors against $3CL^{pro}$ contain different warheads such as α-ketoamide (Zhang et al., 2020), α,β-unsaturated ester (Jin et al., 2020), aldehyde (Dai et al., 2020), bisulfite (Kim et al., 2016; Vuong et al., 2020), keto (Hoffman et al., 2021) and its phosphate prodrug (Boras, 2020), as well as ester (Ghosh et al., 2021) for forming a covalent bond with the catalytic Cys145, where the P1 residue is strictly a cyclic lactam mimicking Gln to ensure tight binding. To date, Paxlovid developed by Pflizer Co., a nitrile-based covalent $3CL^{pro}$ peptidomimetic inhibitor combined with ritonavir for inhibiting CYP3A4, was approved for treatment. After maturation by $3CL^{pro}$, the viral RdRp essential for gene replication is the antiviral target of Remdesivir (Gordon et al., 2020; Wang et al., 2020) developed by Gilead Co., which showed a marginal efficacy in clinical trials (Grein et al., 2020). Another RdRp inhibitor, Molnupiravir developed by

doi:10.6342/NTU202400256

Merck Co., a prodrug of the nucleoside analogue N4-hydroxycytidine (Sheahan et al., 2020), has also been approved.

While using $3CL^{pro}$ and RdRp as targets has yielded three small-molecule drugs for combating COVID-19, only antibodies such as Bebtelovimab, which bind Spike to block RBD:ACE2 interaction and prevent virus entry into cells have been approved for therapy. Nevertheless, these neutralizing antibodies are largely evaded by BA.2 and BA.4/BA.5 owing to Spike D405N and F486V mutations, and react weakly to pre-Omicron variants, exhibiting narrow neutralization breadths (Cao et al., 2022). Targeting human Furin using a covalent inhibitor decanoyl-RVKR-chloromethylketone at 5 μM effectively inhibited virus production in SARS-CoV-2-infected VeroE6 cells by blocking virus entry (Cheng et al., 2020). By irreversibly inhibiting human TMPRSS2, Camostat and Nafamostat used a common warhead to block SARS-CoV-2 infection in vitro (Hoffmann et al., 2020a; Hoffmann et al., 2020b; Yamamoto et al., 2020). Moreover, covalent small-molecule ketobenzothiazole TMPRSS2 inhibitors (MM3122 as the lead) were shown to block SARS-CoV-2 viral entry and protect human epithelial lung cells (Mahoney et al., 2021). Specific TMPRSS2 ketobenzothiazole covalent peptidomimetic inhibitor N-0385 was effective against SARS-CoV-2 *in vitro* and *in vivo* using human ACE2 transgenic mouse model of severe COVID-19 (Shapira et al., 2022). However, their keto-reduced hydroxyl analogues not able to link covalently with the active-site essential Ser residue could not inhibit TMPRSS2 and the virus. Aiming to develop potent reversible inhibitors of SARS-CoV-2 entry, but a reversible inhibitor of TMPRSS2 or Furin alone was expected not to achieve the desired potency, we thus designed small molecules which might reversibly inhibit TMPRSS2 and Furin simultaneously. As reported herein, guided by computer

doi:10.6342/NTU202400256

modeling on a class of chalcones, we synthesized a series of 1-(4-(arylethylenylcarbonyl)phenyl)-4-carboxy-2-pyrrolidinones inhibiting TMPRSS2 and Furin, but later found they also inhibited RBD:ACE2 interaction, and studied their structure-activity relationship. The best inhibitor thus achieved potent half maximal effective concentrations (EC_{50}) of 0.023 and 0.002 μM as well as 0.026 and 0.001 μM against the SARS-CoV-2 delta and omicron variants infecting VeroE6 and Calu-3 cells, respectively, and CC_{50}>100 μM, representing a potential lead compound for further preclinical study.

2. Materials and methods

2.1. General methods

Reactions for synthesizing compounds were monitored by using thin-layer chromatography (TLC) on silica gel. Flash chromatography was performed on silica gel of 60–200 μm particle size for compound purification. Yields were reported for spectroscopically pure compounds. Melting points were recorded on the Fargo MP-1D Melting Point Apparatus. NMR spectra were recorded on Bruker AVIIIHD 400MHz FT-NMR in the Department of Chemistry, National Taiwan University. Chemical shifts were given in δ values relative to tetramethylsilane (TMS); coupling constants *J* were given in Hz. Internal standards were $CDCl_3$ (δ_H = 7.24) or DMSO-d_6 (δ_H = 2.49) for ^{1}H-NMR spectra, and $CDCl_3$ (δ_C = 77.0) or DMSO-d_6 (δ_C = 39.5) for ^{13}C-NMR spectra. The splitting patterns were reported as s (singlet), d (doublet), t (triplet), q (quartet), m (multiplet), br (broad) and dd (double of doublets). High resolution mass spectra were measurement by Bruker UPLC-MS in the TechComm core facility, Department of Chemistry, National Taiwan University.

doi:10.6342/NTU202400256

2.2. Chemicals

All the reagents were of the highest commercially available grade and used without further purification. 4-aminoacetophenone, itaconic acid, 3-nitrobenzaldehyde, 4-nitrobenzaldehyde, furan-2-carboxaldehyde, 5-nitrothiophene-2-carboxaldehyde and indole-4-carboxaldehyde were purchased from AK Scientific (Union City, CA, USA). Benzaldehyde and indole-3-carboxaldehyde were purchased from Acros Organics (NJ, USA).

2.3. TMPRSS2 preparation and IC_{50} measurements

Human TMPRSS2 is composed of an intracellular domain, a single-pass transmembrane domain, and a biologically active ectodomain with three subdomains, a low-density lipoprotein receptor type-A (LDLR-A) domain, a Class A Scavenger Receptor Cysteine-Rich (SRCR) domain, and a C-terminal trypsin-like serine protease (SP) domain with a canonical Ser441-His296-Asp345 catalytic triad. For expression of the TMPRSS2 ectodomain (residues 109–492) lacking the N-terminal transmembrane domain, a published procedure was followed (Fraser et al., 2022). The gene synthesized by Toolsbiotech Co. (Taiwan) was constructed into a pFastbac1 vector with a N-terminal honeybee melittin signal sequence and a C-terminal His_8-tag. The activation sequence SSQSR255↓IVGGE (arrow indicates the cleavage site) on the target protein was replaced with an enteropeptidase cleavable DDDDK255 graft by PCR with a forward primer 5'-GATGATGACGACAAGATTGTGGGCGGCGAGAGC-3' and a reverse primer 5'-GTTCAAGTTGACCCCGCAGGC-3' for generating S251D/R252D/Q253D/S254D/R255K mutations. The plasmid for TMPRSS2 expression was transformed into *E. coli* DH10Bac cells (catalog no. 10361012, Thermo Fisher

doi:10.6342/NTU202400256

Scientific, MA, USA) to generate recombinant viral Bacmid DNA. ExpiSf Baculovirus Expression System (catalog no. A38841, A39111, A39112, Thermo Fisher Scientific) was used for high-level protein expression in insect host cells. ExpiSf9 cells were transfected with Bacmid DNA using ExpiFectamine Sf Transfection Reagent to produce the recombinant baculovirus particles which were then amplified from P0 to P1 viral stocks. Recombinant P1 viruses were used to generate suspension culture of baculovirus infected ExpiSf9 insect cells in ExpiSf CD Medium to a density of 5×10^6 cells/ml and infected with the suspension culture of baculovirus infected insect cells before incubation on an orbital shaker (125 r.p.m., 27 °C).

After 4 days of infection, culture supernatant containing the secreted TMPRSS2(109–492)-EFVEHHHHHHH with S251D/R252D/Q253D/S254D/R255K mutations was harvested by centrifugation at 6,000g for 20 min. The pH of 1L cell-free medium was adjusted to pH 7.4 by addition of concentrated 10x phosphate buffered saline (PBS) stock, and loaded onto a HisTrap column (cytiva, MA, USA) to capture the target protein. The HisTrap column was washed separately with 10-column volume of PBS buffer (pH 7.4) containing 10 and 25 mM imidazole, and then eluted with 5-column volume of PBS buffer (pH 7.4) containing 50, 100, and 250 mM imidazole each. The eluted protein solution was pooled and concentrated to 5 mg/mL with a 30 kDa MWCO Amicon filter (Merck, Germany). The target protein was activated by adding 13 units of enteropeptidase (New England Biolabs, MA, USA) per mg of TMPRSS2, and dialyzed against assay buffer (25 mM Tris, pH 8.0, 75 mM NaCl, and 2 mM $CaCl_2$) at room temperature overnight. Activated TMPRSS2 ectodomain (referred as TMPRSS2 here) solution was exchanged to the size-exclusion chromatography buffer (50 mM Tris, pH 7.4, and 250 mM NaCl), spun

doi:10.6342/NTU202400256

down at 21,000g, and then loaded to a Superdex 75 10/300 GL column (GE Healthcare, Chicago, USA). The fractions spanning the dominant peak eluted at 9.74 mL was confirmed to be TMPRSS2 by reducing SDS-PAGE, and were subsequently pooled and concentrated. Aliquots of concentrated (0.19 mg/mL~4.3 μM) stock in the buffer (50 mM Tris pH 7.4, 250 mM NaCl, and 25% glycerol) were flash-frozen by liquid nitrogen and stored at -80 °C

TMPRSS2 activity was assayed using a fluorogenic substrate Boc-Gln-Ala-Arg-AMC (catalog no. 4017019.0025, Bachem, Bubendorf, Switzerland), and the signal was detected by the BioTek Synergy H1 microplate reader (Agilent Technologies, Inc., CA, USA). In the 96-well plate, the 100-μL reaction mixtures per well containing 1.3 nM TMPRSS2, 10 μM substrate, and different concentrations of inhibitors in the buffer of 20 mM Tris-HCl pH 7.4 with 1% DMSO for dissolving the compounds. The fluorescence was monitored for 5 min at excitation/emission of 355/460 nm. IC_{50} values, the concentrations of inhibitors required to reduce half of the enzymatic activities, were determined by pre-incubating TMPRSS2 with inhibitors at concentrations ranging from approximately half to 5-fold IC_{50} values for 5 min and fitting the concentration-dependent TMPRSS2 inhibition curves with the equation $A(I) = A(0) \times \{1-[I/(I + IC_{50})]\}$ using GraphPad Prism software (v.9.4.0). In this equation, A(I) is the enzyme activity with inhibitor concentration I, A(0) is the enzyme activity without inhibitor, and I is the inhibitor concentration. For each inhibitor, the measurements were repeated three times to yield the averaged IC_{50} and the standard deviation.

2.4. Furin IC_{50} measurements

Furin activity was assayed using a commercial Furin Protease Assay Kit (catalog #

doi:10.6342/NTU202400256

78040, BPS Bioscience, CA, USA). In 20-μL reaction mixture on a 384-well plate, it contained 0.25 ng/μL Furin, 2 μM fluorogenic substrate, and different concentrations of inhibitors in assay buffer with 1% DMSO for dissolving compounds. The fluorescence change was monitored for 30 min at excitation/emission of 380/460 nm. IC_{50} values were determined by pre-incubating Furin with inhibitors at concentrations ranging from approximately half to 5-fold IC_{50} values for 5 min and the concentration-dependent Furin activity inhibition curves were fitted with the equation $A(I) = A(0) \times \{1-[I/(I + IC_{50})]\}$ using GraphPad Prism software (v.9.4.0). In this equation, A(I) is the enzyme activity with inhibitor concentration I, A(0) is the enzyme activity without inhibitor, and I is the inhibitor concentration. For each inhibitor, the measurements were repeated three times to yield the averaged IC_{50} and the standard deviation.

2.5. Antivirus EC_{50} and cytotoxicity CC_{50} measurements

Two methods, the plaque reduction assay, and the yield reduction assay, were used to determine the EC_{50} of compounds against SARS-CoV-2. All experiments involving the SARS-CoV-2 virus were performed in the Biosafety Level-3 Laboratory of the First Core Laboratory, National Taiwan University College of Medicine. For the viral plaque reduction assay, Vero E6 cells were seeded into a 24-well culture plate in Dulbecco's Modified Eagle Medium (DMEM) with 10% Fetal Bovine Serum (FBS) and antibiotics one day before the infection. VeroE6 cells were infected by SARS-CoV-2 delta virus (NTU92) or omicron BA.1 (NTU128) at 50−100 pfu (plaque forming unit) for 1 h at 37 °C. After removal of the virus inoculum, the cells were washed once with PBS and overlaid with 1 mL overlay medium containing 1% methylcellulose for 5 days at 37 °C. After 5 days, the cells were fixed with 10% formalin overnight. After removal of the overlay

doi:10.6342/NTU202400256

medium, the cells were stained with 0.5% crystal violet, and the plaques were counted. The percentage of inhibition was calculated as $[1-(V_D/V_C)] \times 100\%$, where V_D and V_C refer to the virus titer in the presence and absence of the inhibitors, respectively. The minimal concentrations of the compounds required to reduce plaque numbers by 50% (EC_{50}) were calculated by regression analysis of the dose-response curves.

To characterize the EC_{50} of the compound against SARS-CoV-2 infecting human Calu-3 cells, yield reduction assays were performed because the virus could not form plaques on the Calu-3 cells. In brief, Calu-3 cells were seeded into 24-well culture plates and cultured for 4 days. About 6,000 pfu of viruses were pretreated with the compound or DMSO for 1 h before infection. After 1 h of infection, the virus-containing medium was removed, and cells were incubated in DMEM supplemented with 2% FBS and 1% antibiotics for 24 h. Afterward, culture supernatant was harvested for virus titration. Subsequently, the infectious virus titer in the culture supernatant was quantified by plaque assay in Vero E6 cells. The procedures of the plaque assay were described below. Vero E6 cells (2×10^5 cells/well) were seeded in 24-well plates in DMEM supplemented with 10% FBS and antibiotics one day before infection. The supernatant was 10-fold serially diluted and added to the cell monolayer for 1 h at 37 °C. Subsequently, the virus was removed, and the cell monolayer was washed once with PBS before overlay medium containing 1% methylcellulose was added. The cells were then incubated for 5 days. Afterward, the cells were fixed with 10% formaldehyde overnight. The overlay medium was removed, and the cells were stained with 0.5% crystal violet, and the plaques were counted. The inhibition percentage of compound **81** against viruses was calculated as $[1-(V_D/V_C)] \times 100\%$, where V_D and V_C refer to the virus titer in the presence and absence of the compound,

doi:10.6342/NTU202400256

respectively. The EC_{50} values were calculated by regression analysis of the dose-response curves.

Cytotoxicity of the inhibitors was determined by using the acid phosphatase assay. Briefly, Vero E6 or Calu-3 cells were seeded onto a 96-well culture plate at a concentration of 2 x 10^4 cells per well. Next day, the medium was removed and each well was washed once with PBS before addition of DMEM containing 2% FBS and different concentrations of inhibitors. After 3 days of incubation at 37 ºC, medium was removed and each well was washed once with PBS. Next, a buffer containing 0.1 M sodium acetate (pH = 5.0), 0.1% Triton X-100, and 5 mM p-nitrophenyl phosphate (P5994, Sigma-Aldrich/Merck, Germany) was added. After incubating at 37 °C for 30 min, 1 N NaOH was added to stop the reaction. The absorbance was determined by ELISA reader (VERSAmax, Molecular Devices, Sunnyvale, CA, USA) at a wavelength of 405 nm. The percentage of cytotoxicity was calculated using the following formula: cytotoxicity % = [(At/As)×100]%, where At and As refer to the absorbance of a tested substance and solvent control, respectively. The 50% cytotoxicity concentration (CC_{50}) was defined as the concentration reducing 50% of cell viability. For each data point, the measurements were repeated three times to yield the averaged number and the standard deviation. The CC_{50} values were calculated by non-linear regression analysis of the dose-response curves.

2.6. RBD:ACE2 interaction IC_{50} measurements and pseudovirus assay

Inhibition of RBD:ACE2 binding by the synthesized compounds were measured by using the commercial kit of NanoBiT technology (Promega, WI, USA). A stable cell line expressing SmBiT-tagged human ACE2 on HeLa cells was established and the recombinant RBD-LgBiT protein (amino acid 330–521 of Spike) was produced (Lee et al.,

doi:10.6342/NTU202400256

2022). To monitor the interaction between RBD and ACE2, SmBiT-ACE2 expressing cells were seeded onto a white 96-well plate at a density of 1×10^4 cells per well. For each binding assay, cells were washed once with PBS and pretreated with 50 µL of an indicated compound per well for 10 min. Next, a 50 µL reaction mixture containing 10 ng RBD-LgBiT, 0.5 µL of Nano-Glo luciferase assay substrate, and 9.5 µL of luciferase assay diluent (Promega) was added into each well. Luminescence signal was recorded every 2 min and continuously for 1 h by microplate reader (BioTek Synergy HTX, VT, USA) at 37 ^{o}C with time-lapsed kinetics program. For calculating RBD inhibition of all agents, luminescent data from the time point showing highest signal in negative control sample was chosen for downstream calculation. Inhibition (%) = [1- (luminescence signal of test sample)/(luminescence signal of negative control sample)] × 100%. The compound concentration for inhibiting 50% of the interaction was defined as IC_{50}. The measurements were performed in triplicate.

2.7. Pseudovirus assays

For producing lentivirus-based pseudoviruses (Lee et al., 2022), 5 µg transfer plasmid (pLAS2w.Nluc-T2A-RFP-C.Ppuro), 4 µg packaging plasmid (pCMVdeltaR8.91 from the RNAicore, Academia Sinica, Taipei, Taiwan), and 1 µg of the envelope glycoprotein of vesicular stomatitis virus (the VSV-G protein) or spike-expressing plasmid (delta derivatives of pcDNA3.1-2019-nCoV-S-d18, from the RNAicore, Academia Sinica, Taiwan) were co-transfected with Lenti-X 293T cells. Virus-containing supernatants were collected and quantitated by real-time PCR. For pseudovirus infection assays, Hela cell line stably expressed ACE2-SmBiT (Hela-ACE2) or Calu-3 cell line was seeded into the 96-well white plate at a density of 1×10^4 cells per well in the presence of 100 µL DMEM.

doi:10.6342/NTU202400256

After 16 h, cells were treated with 2×10^5 copies of VSV-G or spike pseudovirus containing delta Spike and NanoLuc reporter (Lee et al., 2022) along with a two-fold serial dilution compound **81**. After 6 h of incubation, cells were washed with PBS three times and then changed with complete DMEM for additional 24 h. To measure the NanoLuc activity of the pseudovirus particles inside the cells, a mixture of 50 μL OPTI-MEM containing 8 μM substrate of Nanoluc, furimazine (TargetMol) was added to each well. The luminescence signal was immediately recorded using a luminescent microplate reader (BioTek Synergy HTX, Agilent Technologies) at 37 ^{o}C with a time-lapsed kinetics program of 2-min intervals for 30 min. To calculate the percentage of infectivity, the luminescent data from the time point showing the highest signal in the wild-type ACE2 infected with indicated pseudoviruses sample was chosen. The inhibition (%) was calculated as follows: 1-(luminescence signal of the test sample)/ (luminescence signal of DMSO vehicle control) × 100%. The compound concentration for inhibiting 50% of the pseudovirus entry was defined as EC_{50}. The measurements were performed in triplicate.

2.8. Expression and purification of the recombinant SARS-CoV-2 delta variant RBD and human ACE2

Expression of RBD followed a reported procedure (Lan et al., 2020). The gene encoding delta strain RBD was PCR amplified with a ligation-independent cloning-compatible primer pair (forward primer 5'-TCTTACATCTATGCGAGAGTCCAACCAACAGAA-3' and reverse primer 5'-GTGCTCTACGAACTCGAAATTGACACATTTGTTTTT-3'). The PCR product containing sequences encoding an N-terminal melittin signal sequence for secretion and a C-terminal His_8-tag for purification, was cloned into pFastBac-1 vector. The sequencing-

doi:10.6342/NTU202400256

verified plasmid was transformed into DH10Bac competent cells to generate a bacmid encoding RBD (residues Arg319–Phe541). The ExpiSf Baculovirus Expression System with a chemically defined medium for suspension culture of high-density ExpiSf9 cells was used for virus production and protein overexpression. After 48–72 h of culturing, ExpiSf9 cells were collected by centrifugation and resuspended in HBS buffer (10 mM HEPES, pH 7.2, and 150 mM NaCl). The recombinant delta SARS-CoV-2 RBD was first captured by Ni-NTA resin (Agarose Bead Technologies , USA) and eluted with 500 mM imidazole in HBS buffer. Then, it was purified by gel filtration chromatography using a pre-equilibrated Superdex 75 10/300 GL column (GE Healthcare) and eluted with HBS buffer.

Expression of ACE2 was performed by a previously reported procedure (Lan et al., 2020). The gene was provided by Dr. Shang-Te Danny Hsu in our institute and PCR amplified with a ligation-independent cloning-compatible primer pair (foreard primer 5'-TCTTACATCTATGCGTCCACCATTGAGGAACAG-3' and reverse primer 5'-GTGCTCTACGAACTCGTCTGCATATGGACTCCA-3'). The PCR product containing sequences encoding an N-terminal melittin signal sequence for secretion and a C-terminal His_8-tag for purification, was cloned into pFastBac-1 vector. The sequencing-verified plasmid was transformed into DH10Bac competent cells to generate a bacmid encoding the N-terminal peptidase domain of human ACE2 (residues Ser19–Asp615). The ExpiSf Baculovirus Expression System with a chemically defined medium for suspension culture of high-density ExpiSf9 cells was used for virus production and protein overexpression. After 48–72 h, ExpiSf9 cells were collected by centrifugation and resuspended in HBS buffer (10 mM HEPES, pH 7.2, 150 mM NaCl). The N-terminal peptidase domain of

doi:10.6342/NTU202400256

human ACE2 was subsequently purified using the same protocol for RBD purification described above.

2.9. Thermal shift experiments

The experiments were performed as described (Bojadzic, 2021) to determine which of RBD or ACE2 bound **2f** (**81**). A RT-PCR machine (CFX Real-Time PCR System, Bio-Rad Laboratories, CA, USA) was programmed to equilibrate each sample at 25 °C for 90 s and then increase temperature to 95 °C by 0.5 °C every 10 s for taking a fluorescence reading of the denatured portion of protein stained with SYPRO Orange dye (Merck KGaA, Darmstadt, Germany). Melting point of each protein was the lowest point of the first derivative plot, as calculated by the software (Bio-Rad CFX Manager ver.3.0) included with the RT-PCR machine. After performing a series of preliminary scans at various concentrations of proteins, compound, and dye, optimal concentrations were determined to be 0.05 mg/mL RBD, 0.05 mg/mL ACE2, 50× SYPRO Orange, 1x PBS, and 10 μM compound **2f**. Using this optimal condition, the plots of -d(RFU)/dT (RFU is relative fluorescence units) vs. temperatures for RBD or ACE2 in the absence or presence of **81** were compared.

2.10. Molecular docking

The molecular docking was performed using the iGEMDOCK software to predict how compound **2f** binds with TMPRSS2, Furin, and RBD of SARS-CoV-2 delta variant Spike protein. The three-dimensional (3D) structures of TMPRSS2 (PDB: 7meq), Furin (PDB: 5jxg), and RBD (PDB: 7w92) were retrieved from the RCSB protein data bank (PDB, https://www.rcsb.org/). All water molecules and bound ligands were removed from these structures prior to docking. The binding cavity of TMPRSS2 were extracted by

doi:10.6342/NTU202400256

selecting the 12 Å residues around the catalytic triad (Ser441-His296-Asp345), and the binding cavity of Furin was extracted by selecting the 12 Å residues around the catalytic residues, Asp153, His194, Asn295, and Ser368. RBD domain (residues 319 to 541) was extracted from the open state of SARS-CoV-2 delta variant Spike protein. The cavities were then prepared by defining the residue atom types and charges assignment via iGEMDOCK method. Compound **2f**'s 3D structure was generated from Molview website (https://molview.org/), and the structural information was transformed into mol2 format by using Open Babel GUI software.

For molecular docking process, docking accuracy settings (GA parameters including population size: 800, generations: 80, and number of solutions: 10) were chosen, and iGEMDOCK software was used to generate protein-ligand interaction profiles of Electrostatic (E), Hydrogen-Bonding (H), and Van der Waals interaction (V). Once docking was finished, iGEMDOCK was used to analyze and rank all docked poses based on the estimated binding energy. The scores of the docked poses were estimated as the total energy of Electrostatic (E) + Hydrogen-Bonding (H) + Van der Waals (V) in the docking site. Each docked pose with the lowest energy was considered as the best pose for compound **2f** against the target cavity.

2.11. Drug likeness analysis

The 3D structure of **2f** was converted into a SMILES format by Open Babel GUI software (O'Boyle et al., 2011). To assess the drug likeness of compound **2f**, the online tool (http://www.scfbio-iitd.res.in/software/drugdesign/lipinski.jsp) was used for Lipinski rule of five estimation (Lipinski 2004; Jayaram et al., 2012). The ADMET profile of **2f** was estimated by pkcsm website (http://biosig.unimelb.edu.au/pkcsm/) (Pires et al., 2015).

doi:10.6342/NTU202400256

2.12. Animal studies

The prototype SARS-CoV-2 strain CGU4 (Taiwan/CGMH-CGU-01/2020; GISAID identifier: EPI_ISL_411915; NCBI accession number: MT192759) was kindly provided by the Taiwan CDC and propagated in Vero E6 cells (Tang et al., 2021). All animal procedures complied with the ARRIVE guidelines (www.arriveguidelines/org/) and were reviewed and approved by the National Defense Medical Center Animal Care and Use Committee (approval numbers: AN-111-24). Syrian hamsters were purchased from the National Laboratory Animal Center (Taipei, Taiwan) and fed a standard low-fat polysaccharide-rich chow diet (LabDiet 5053; Purina, St Louis, MO, USA). Intranasal inoculation of SARS-CoV-2 (strain CGU4) was performed under anesthesia (Zoletil® 40 mg/kg plus xylazine 4 mg/kg). The antiviral activity of compound **81** was assessed through the following parameters: daily changes in body weight and virus quantification in the nasal turbinates and lungs. Compound **81** was dissolved in DMSO and further diluted with sterile PBS. Syrian hamsters, ranging in age from 5 to 6 weeks, were divided into two groups. Treatment group (n = 6) received **81** by oral administration (25 mg/kg once per day) and vehicle group (n = 6) received PBS. The hamsters were challenged intranasally with SARS-CoV-2 (5.0×10^4 pfu in 50 μL PBS). The body weight of each hamster was recorded daily. Hamsters were euthanized on day 3 or day 6 post-viral challenge by Zoletil® overdosing, and nasal turbinate and lung samples were collected for analyses.

For the RNA extraction and qRT-PCR analysis, nasal turbinate and lung tissues were placed in RNAlater (Thermo Fisher Scientific, MA, USA) overnight at 4 °C and homogenized by bead-beating technology. Total RNA was extracted with TRIzol reagent (Thermo Fisher Scientific) and genomic DNA was removed by DNase (Promega, Madison,

doi:10.6342/NTU202400256

WI, USA) according to the manufacturer's instructions. RNA samples were further purified by phenol/chloroform method and ethanol precipitation. Equal amounts of total extracted RNA were subsequently reverse transcribed with the M-MLV reverse transcriptase system (Thermo Fisher Scientific) using random primers. Subsequently, qRT-PCR was performed on a QuantStudio3 qRT-PCR system (Applied Biosystems, Foster City, CA, USA) using the following the specific primers targeting E gene (forward primer 5'-ACAGGTACGTTAATAGTTAATAGCGT-3' and reverse primer 5'-ATATTGCAGTACGCACACA-3'). The hamster β-actin (internal control) primers were forward primer 5'-ACTGCCGCATCCTCTTCCT-3' and reverse 5'-TCGTTGCCAATGGTGATGAC-3'. Probe 5'-[6FAM]ACACTAGCCATCCTTACTGCGCTTCG[BHQ1]-3' was used for E gene subgenomic mRNA quantitation. The relative mRNA expression was calculated with the $2^{-\triangle Ct}$ method.

For pharmacokinetic studies, a total of eight K18-hACE2 transgenic mice (n = 4 for oral administration and n = 4 for intravenous injection via tail vein) at 12 weeks of age and 20.3-24.2 g body weight were used. Compound **81** was dissolved in DMSO and further diluted with sterile PBS to 1 mg/mL and then administered orally or intravenously via the tail vein as a single injection at a volume of 25 mL/kg. Both oral and intravenous (IV) administration groups were split in half to allow further repeated blood sampling at 0, 15, 30, 60, 120, and 240 min as follows: n = 2 were bled at 0, 15, and 30 min post injection from the facial vein, and at 60 min via cardiac puncture under anesthesia; the other n = 2 were bled at 0, and 120 min post-injection from the facial vein, and at 240 min via cardiac puncture under anesthesia. Blood samples were collected in a collection tube (365992, BD

doi:10.6342/NTU202400256

Microtainer BD bioscience, USA) and centrifuged at 3,000 g for 5 min at 4 °C to separate the serum. The serum samples were stored at -20 °C until LC-MS analysis. Pharmacokinetic analysis of serum compound **81** was performed by a non-compartmental analysis using PKSolver 2.0 software (China Pharmaceutical University, Nanjing, China).

For LC-MS analysis, serum samples were mixed with 100% MeOH (1:10, v/v) and sonicated for 30 min. After centrifuging at 20,000 g for 10 min at 4 °C, the supernatant was evaporated to dryness at 35 °C and then dissolved with 100 μL of MeOH and filtrated. The resulting supernatant was injected into the LC-MS system for analysis. All LC-MS analyses were carried out using the mass spectrometer Shimadzu 2020 LC-MS with both positive and negative mode electrospray ionization using a 10 min linear gradient of 5−95% MeCN-H_2O with 0.5 % formic acid followed by 95% MeCN-H_2O for 4 min at a flow rate of 0.5 mL/min (Kinetex® 2.6 μm Polar C18 100 Å, 100 × 2.1 mm column). Calibration curves used 7 concentration points prepared in the concentration ranges 0.25−30 μM of compound **81**. Analyte concentrations were determined using the internal standard method.

3. Results and discussion

3.1. Synthesis of 1-(4-(arylethylenylcarbonyl)phenyl)-4-carboxy-2-pyrrolidinones 2a–g

The preliminary product 1-(4-acetylphenyl)-4-carboxy-2-pyrrolidinone **1** was synthesized by heating of 4-aminoacetophenone with itaconic acid without any solvent (Scheme I). Then by following a similar procedure (Voskiene et al., 2007), the compounds **2a**–**g** were synthesized with good yields by base (NaOH)-catalyzed aldol condensation of **1** and the unsubstituted or substituted benzaldehydes or heterocyclic aldehydes in ethanol (Scheme I).

doi:10.6342/NTU202400256

Scheme I. Synthesis of 1-(4-(arylethylenylcarbonyl)phenyl)-4-carboxy-2-pyrrolidinones

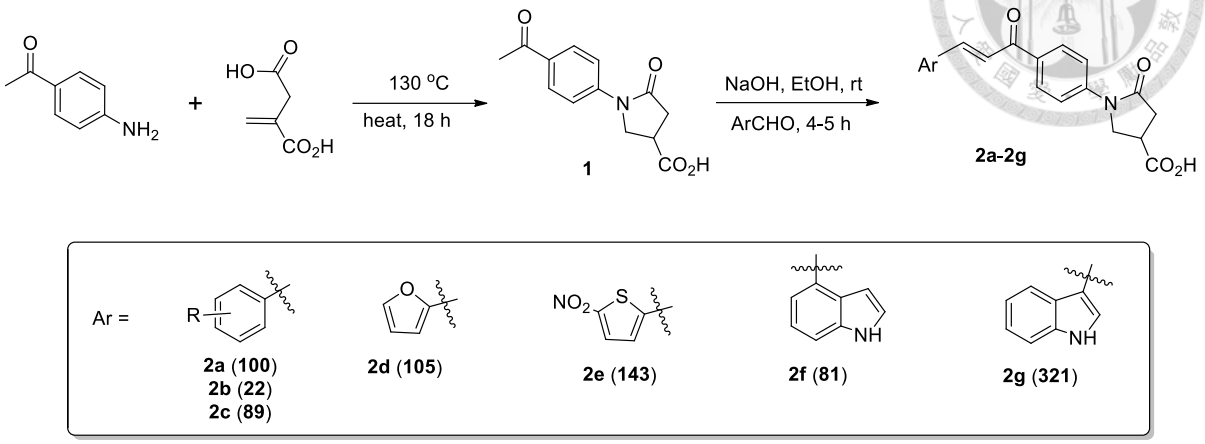

The chemical structures of synthesized compounds were confirmed by NMR and MS. The NMR assignment was made on the substituents additivity rules, spectral characteristics of structurally related compounds, signal intensities, and multiplicities. ^{13}C NMR spectra were used to prove the interpretation of the carbon resonances in some cases.

3.2. Synthesis of 4a and 4b without the carboxylate

The negatively charged carboxylate on the pyrrolidinone may impede the passage of compounds across cellular membrane. Therefore, the carboxylate group was removed from the two selected antiviral compounds to examine whether it could facilitate their cellular uptake. For synthesis of compound **3**, the non-carboxylate analogue of **1**, Scheme II was adopted by using a similar procedure (Jiang, 2014). Then, by following Scheme II, compounds **4a** and **4b**, the analogues of **2a** and **2f**, respectively, without the carboxylate group on the pyrrolidinone moiety were synthesized.

doi:10.6342/NTU202400256

Scheme II. Synthesis of 1-(4-(arylethylenylcarbonyl)phenyl)-2-pyrrolidinones

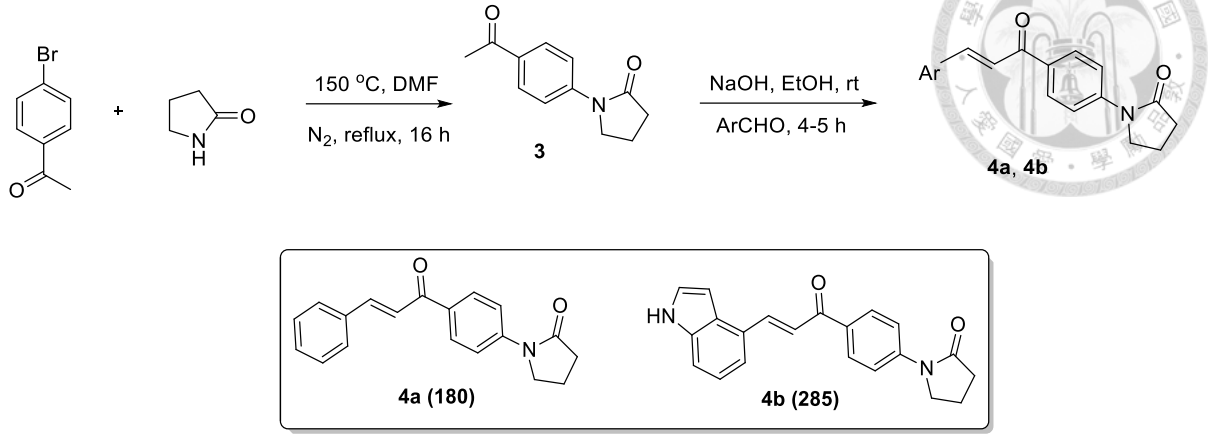

3.3. Evaluation of 2a–g and 4a–b against TMPRSS2 and Furin (by CW Li in Dr. PH Liang's laboratory)

TMPRSS2 and Furin are involved in SARS-CoV-2 entry by processing of the viral Spike protein. Since they both cleave the Arg-Ser amide bond, it may be possible to design common inhibitors for TMPRSS2 and Furin. Based on our computer modeling on a group of chalcones, we first synthesized **2a**–**g** and evaluated their IC_{50} against the recombinant human protease TMPRSS2 ectodomain that was expressed using the baculovirus system and activated by the enteropeptidase. The purity of recombinant TMPRSS2 was determined by SDS-PAGE as shown in Fig. S2A. The IC_{50} values of three representative inhibitors with the Ar groups, **2b** (**22**) (Ar = 4-nitrobenzene), **2e** (**143**) (Ar = 5-nitrothiophene-2-yl), and **2f** (**81**) (Ar = indol-4-yl), were 12.46, 3.52, and 1.27 μM, respectively (Fig. 1A–C). Other compounds exhibited less potent inhibitory effects against TMPRSS2. The does-dependent curves of **2a (100)** (Ar = benzene) and **2c (89)** are shown in Fig. S2B. **2g** (**321**) with Ar = indol-3-yl linked via different atom from that of **2f** (**81**), and **2d** (**105**) with Ar = furan-2-yl showed no inhibitory activity against TMPRSS2. As summarized in Table 1, while **2a** (**100**) (Ar = benzene) showed a poor IC_{50} of 28.35 μM,

doi:10.6342/NTU202400256

compounds **2b** (**22**) with a larger 4-NO_2 substituent on the benzene ring increased more than 2-fold of potency against TMPRSS2 (IC_{50} = 12.46 μM). Nevertheless, the 3-NO_2 substituent in compound **2c** (**89**) did not significantly increase the potency.

The inhibitory activities of the synthesized compounds against Furin and another human protease Cathepsin L were examined. Based on the does-dependent curves of **2b** (**22**), **2e** (**143**), and **2f** (**81**) against Furin (Fig. 1D–F), the IC_{50} values were 10.14, 4.55, and 3.31 μM, respectively. and other plots are shown in Fig. S3. All the data are summarized in Table 1. The compounds at 100 μM did not inhibit Cathepsin L (data not shown). From Table 1, the inhibitors of TMPRSS2 showed a similar trend on inhibiting Furin, indicating the two proteases may provide similar environments for binding with the compounds. Therefore, **2d** and **2g** which were inactive against TMPRSS2 did not inhibit Furin as well (Table 1). These indicated a similar structure-activity relationship of the synthesized compounds against TMPRSS2 and Furin, consistent with our modeling prediction.

To better understand the importance of carboxylate on the inhibition of TMPRSS2 and Furin, the carboxylate was removed from compound **2a** and **2f** to synthesize **4a** and **4b,** respectively. As shown in Fig. 1G, **4b** (**285**) inhibited TMPRSS2 with an IC_{50} of 31.64 μM, which was significantly higher than that of **2f**. Similarly, **4a** failed to inhibit TMPRSS2 and Furin. These data indicated that the carboxylate of **2a** and **2f** participated the binding with TMPRSS2 and Furin.

3.4. Evaluation of 2a–g and 4a–b against SARS-CoV-2 (by TL Chao and JT Fang in Dr. SY Chang's laboratory)

As mentioned above, the inhibitory activity of compounds on TMPRSS2 and Furin could endow them with antiviral activity because these proteases are essential for viral

doi:10.6342/NTU202400256

entry by trimming Spike. We then measured their EC_{50} against SARS-CoV-2 infection of VeroE6 cells under two different ways of treatment. Each compound was either pretreated with the virus and included during the virus infection of the VeroE6 cells (entry treatment), or added only after virus infection (post-entry treatment) to examine at which stage did these compounds blocked virus infection of the target cells. As expectedly, we found that the compounds suppressed the viral plaque formation by entry treatment, but not by the post-entry treatment. The EC_{50} values measured under "entry treatment" were obtained from the dose-dependent virus (SARS-CoV-2 delta strain) plaque reduction curves by using different concentrations of the compounds as shown in Fig. 2A−C for **2b** (**22**), **2e** (**143**), and **2f** (**81**), respectively. Among them, the best inhibitor **81** showed potent antiviral activities against two different variants, delta and Omicron BA.1 strains, with EC_{50} values of 0.023 and 0.002 μM, respectively, and CC_{50}>100 μM (Fig. 2C and D). The plots for other compounds against delta SARS-CoV-2 infecting VeroE6 cells are shown in Fig. S4. Furthermore, the antiviral activity of the most potent inhibitor **2f** (**81**) in human Calu-3 lung cells was determined, and the EC_{50} values against the delta and omicron SARS-CoV-2 infection were 0.026 and 0.001 μM, respectively, based on the dose-dependent SARS-CoV-2 yield reduction and CC_{50}>100 μM (Fig. 2E and F). All the measured EC_{50} and CC_{50} values were summarized in Table 1. To our surprise, **2d** showing no TMPRSS2 and Furin inhibitory activity at 50 μM still inhibited the virus with a less potent EC_{50} of 1.06 μM. This suggested other target for the active antivirals in this series of compounds. We then chose RBD:ACE2 interaction as a possible target to investigate the inhibitory power of all the active antivirals.

doi:10.6342/NTU202400256

3.5. IC_{50} of the compounds against RBD:ACE2 interaction (by MYC Pan in Dr. LHC Wang's laboratory)

A cell-based commercial assay kit (NanoLuc® Binary Technology, NanoBiT), composed of a Large BiT (LgBiT; 18kDa) subunit conjugated with delta SARS-CoV-2 RBD and SmBiT-ACE2 stably expressing Hela cells (HeLa-ACE2), was used to measure IC_{50} of test compounds on inhibiting RBD:ACE2 interaction. In the asssy, binding of RBD with ACE2 would bring Large BiT and small SmBiT together to form an active enzyme to generate a bright luminescent signal in the presence of substrate. The presence of inhibitor would weaken the signal, and the dose-dependent inhibition curves against delta virus RBD:ACE2 interaction by the potent antivirals **2b** (**22**), **2e** (**143**), and **2f** (**81**) are shown in Fig. 3A, B, and C, respectively. The plots for other compounds are shown in Fig. S5. As summarized in Table 1, all of the synthesized compounds, including the two inactive TMPRSS2 and Furin inhibitors **2d** (**105**) and **2g** (**321**), could inhibit RBD:ACE2 interaction with IC_{50} values between 2.81 and 33.99 μM. The analogues of **2a** and **2f**, **4a** (**180**) and **4b** (**285**), also inhibited RBD:ACE2 interaction (shown in Fig. 3D for **4b** and Fig. S5 for **4a**). From these in vitro inhibition studies, the most potent antiviral **2f** actually displayed potent inhibition on enzyme activities of TMPRSS2 and Furin, and RBD:ACE2 interaction, which are concordant with its most potent antiviral activity against SARS-CoV-2. Inhibition of RBD:ACE2 interaction provided the basic antiviral activity for **2d**, **2g**, **4a** (Fig. S5), and **4b** (Fig. 3D), which showed none or minimal inhibition on TMPRSS2 and Furin enzyme activities. For compounds which can inhibit TMPRSS2 and Furin activities, their antiviral activities could be further enhanced, such as **2b**, **2e**, and **2f**.

doi:10.6342/NTU202400256

3.6. Pseudovirus assays (by YT Chiu in Dr. LHC Wang's laboratory)

To clarify the contribution of inhibiting RBD:ACE2, TMPRSS2, and/or Furin on antiviral activities of our compounds, we examined the **81**-mediated inhibition of SARS-CoV-2 pseudoviral entry by using a pseudovirus containing delta Spike or VSV-G on the surface and NanoLuc reporter inside to infect the chosen cells. As shown in Fig. 3E, **2f** (**81**) effectively inhibited the pseudovirus entry into Calu-3 lung cells with an EC_{50} of 8.3 μM. As a control, entry of VSV-G bearing pseudovirus that is independent from RBD:ACE2, TMPRSS2, and/or Furin into Calu-3 cells was not inhibited by our compound **81** (Fig. 3F). We showed that the SARS-CoV-2 pseudovirus infected Hela-ACE2 stable cell line with an EC_{50} of 14.7 (Fig. 3G), but not its parental HeLa cells (Fig. not shown), indicating the requirement of inhibiting RBD:ACE2 for antiviral activity. We further showed that pseudoviral entry into Calu-3 cells that express TMPRSS2 could be potently inhibited by the specific TMPRSS2 inhibitor Camostat with an EC_{50} of 0.04 μM (Fig. 3H), but not by the specific Furin inhibitor decanoyl-RVKR-chloromethylketone (Fig. 3I). As expected, Camostat could not inhibit pseudoviral entry into HeLa-ACE2 cells that lack TMPRSS2 (Fig. 3J). Taken together, compound **81** inhibited mainly RBD:ACE2 and additionally by TMPRSS2, but not necessarily by Furin, for anti-pseudovirus activity on Calu-3 cells.

3.7. Thermal shift experiments to distinguish the target for RBD:ACE2 inhibitors (by HLV Lo in Dr. PH Liang's laboratory)

To determine whether the RBD:ACE2 inhibitors targeted RBD and/or ACE2, we expressed and purified recombinant RBD and ACE2 proteins (Fig. S6A). To prove the recombinant RBD and ACE2 were functional, RDB was coated on the CM5 chip and

doi:10.6342/NTU202400256

ACE2 was flown through to measure the ACE2 concentration-dependent sensograms using Biacore apparatus (Fig. S6B), which allowed the determination of RBD:ACE2 K_d of 81.28 nM, a tight binding. Nevertheless, **2f** (**81**) did not influence the concentration-dependent binding curves with either ACE2 or RBD coating on a chip, probably due to not sufficient mass change to be detected. Thermal shift experiments were conducted instead. When adding increasing concentrations of **2f**, no changes of the melting temperature (T_m) of ACE2 was observed (Fig. 4A), whereas T_m of RBD was shifted (Fig. 4B), indicating binding of **2f** with RBD only.

3.8. Binding modes of the inhibitor with TMPRSS2, Furin, and RBD (by JJ Liu in Dr. PH Liang's laboratory)

To rationalize the structure-activity relationship of the antivirals on inhibiting TMPRSS2, a docking study was conducted with the clues that the carboxylate on the pyrrolidinone ring and the indole ring on the other side are important for **81**-mediated inhibition. As shown in Fig. 5A, the best inhibitor **2f** (**81**) was docked into the active site of TMPRSS2. There are three major binding interactions contributed by the carboxylate of pyrrolidinone, the carbonyl group, and the indole ring, respectively. The carboxylate on the pyrrolidinone ring forms two hydrogen bonds with the hydroxyl group of Thr393. This explains why the compound showed a significantly weaker inhibitory activity against TMPRSS2 after removing the carboxylate. The carbonyl group forms a hydrogen bond with the side-chain N atom of His296. Moreover, the indole ring forms two hydrogen bonds with the backbone carbonyl oxygen of Gly462 and side-chain oxygen of Ser436.

Docking of **2f** (**81**) into Furin also revealed importance of the carboxylate on inhibition. As shown in Fig. 5B, **2f** was docked against the Furin protease (PDB: 5jxg).

doi:10.6342/NTU202400256

According to the docking result, the terminal carboxyl group of **2f** has strong interactions with Furin, including an electrostatic interaction with the guanidine group of Arg197 and a hydrogen bonding with Arg193 and His364. Besides, the nitrogen of the indole ring also forms a hydrogen bond with Pro256, and the oxygen of the ketone group forms a hydrogen bond with the nitrogen of the main chain of Ser368.

Since our thermal shift experiments showed RBD as the target, computer docking was performed to understand the binding mode of compound **2f** in RBD. As shown in Fig. 5C, **2f** (**81**) was docked against the RBD of SARS-CoV-2 delta variant Spike protein (PDB: 7w92). Compound **2f** has both hydrogen bonding and van der Waal's interaction with Gln493 of RBD, which plays an important role on contacting with Lys31 of ACE2. Besides, the oxygen on the pyrrolidinone group also interacts with Gly496 of RBD through hydrogen bonding. In the delta RBD:ACE2 complex, Lys353 of ACE2 forms a hydrogen bond with Gly496 of RBD. Therefore, by forming interactions with the key residues of RBD, compound **2f** might disrupt the contact between ACE2 and RBD.

3.9. Drug-likeness of the inhibitor as judged from Lipinski rule of five (by JJ Liu in Dr. PH Liang's laboratory)

Lipinski's rule was developed to determine the druggability of compounds for pharmaceutical development. For preparation of compound **2f**'s 3D structure, Molview website (https://molview.org/) was utilized, and the structure information was converted into a SMILES format by Open Babel (O'Boyle et al., 2011). To assess the drug likeness of compound **2f** (**81**), the online tool (http://www.scfbio-iitd.res.in/software/drugdesign/lipinski.jsp) was used for Lipinski rule of five estimation (Lipinski, 2004; Jayaram et al., 2012). Based on Lipinski rule of five, compound **2f** was

doi:10.6342/NTU202400256

accepted in parameters including molecular weight (less than 500 Da), logP (less than 5), hydrogen bond acceptors (less than 10) and donors (less than 5), and molar refractivity (between 40 to 130), indicating that the compound is likely to be a candidate for drug development.

3.10. Drug-likeness of the inhibitor as judged from ADMET properties (by JJ Liu in Dr. PH Liang's laboratory)

ADMET properties predicted in silico could be used to estimate the possibility of compounds to be used as therapeutic agents. There are 5 parameters involved in the ADMET prediction, including absorption, distribution, metabolism, excretion and toxicity. The ADMET profile of compound **2f** (**81**) was estimated by pkcsm website (http://biosig.unimelb.edu.au/pkcsm/) (Pires, 2015). Its absorption was portrayed by human colorectal adenocarcinoma cell line (Caco2) permeability and human intestinal absorption (HIA). The Caco2 permeability and the HIA scores are relatively high, indicating compound **2f** could be absorbed into the human intestine. Analysis of distribution progress, the blood brain barrier (BBB) and central nervous system (CNS) permeability of compound **2f** indicates that it is unable to penetrate BBB and CNS, and the volume of distribution at steady-state (VDss) implicates that compound **2f** has a higher possibility to distribute in plasma rather than in tissue. In human body, Cytochrome P450 (CYP) enzymes are responsible for the metabolism of drugs, and inhibitors of these CYP enzymes can significantly influence the effect of pharmaceuticals. The predicted results show that compound **2f** might be a substrate of CYP3A4 (an inhibitor of CYP3A4 might be co-administrated with **2f** to increase its half-life), but not other CYP enzymes. For excretion prediction, compound **2f** is not likely to be a renal organic cation transporter-2

doi:10.6342/NTU202400256

(OCT2) substrate, showing there is no potential contraindication. In the toxicity estimation, compound **2f** is not a mutagenic drug and a hERG I/II inhibitor, and it does not have acute toxicity and skin sensitization. However, compound **2f** is predicted to possess hepatotoxicity.

3.11. Preliminary animal study of 2f (animal experiments by Dr. WC Lin, CW Hu, CM Yang, and YY Chen in National Defense Medical Center; pharmacokinetic LC-MASS analysis by Dr. YT Lin in Dr. HC Lin's laboratory)

As predicted above, compound **2f** (**81**) could be a drug-like molecule obeying Lipinski rule of five and with suitable ADMET properties. To verify *in vivo* effectiveness and safety of **2f**, we used hamster, which has been shown to be a satisfactory animal model for SARS-CoV-2 infection (Imai et al., 2020; Sia et al., 2020). Oral administration with **2f** or vehicle began on the same day as infection with 5.0×10^4 pfu SARS-CoV-2 by intranasal inoculation. Body weights were monitored daily for each animal. All hamsters lost weight after inoculation with SARS-CoV-2. However, compared to the vehicle group, hamsters treated with 25 mg/kg of **2f** showed a slightly less weight loss with statistically significance ($P = 0.014$; Fig. 6A). Moreover, in **2f** treatment group, viral genomic copy assessment assays of homogenized hamster nasal turbinates revealed a 5.0- and 5.5-fold reduction in RNA copies at 3 and 6 days post-infection, respectively, in comparison with the vehicle group (Fig. 6B, left panel). However, viral RNA copies detected in lung tissue showed less reduction by the treatment at 3 and 6 days post-infection (Fig. 6B, right panel).

The pharmacokinetics of **81** was also accessed by analyzing the serum samples withdrawn from ACE2 transgenic mice via oral administration or intravenous injection of 25 mg/kg of compound. The serum samples before treatment and after 15, 30, 60, 120, and

doi:10.6342/NTU202400256

240 min of treatment were extracted with methanol and injected into LC-MS system to analyze the concentrations of **81** in the samples based on a linear standard curve generated by using purified **81** at the comparable concentrations. Following the intravenous injection, the serum concentration-time profile of compound **81** was depleted in a biphasic manner (Fig. 6C, left panel for linear and right panel for semi-logarithmic plots, respectively). The PK parameters are shown in Table 3. Through IV injection, compound **81** level was rapidly drop from 2.97 μM at 15 min to 0.78 μM at 60 min, then it was eliminated from the body with the terminal half-life of 1.59 h. Regarding the oral administration, compound **81** reached the peak of 1.13 μM at 15 min and declined to 0.067 μM at 4 h with the terminal half-life of 1.35 h. The oral bioavailability was determined to be 35.19%. Within the experimental period of 4 h, the serum concentrations of **81** were above the anti-SARS-CoV-2 EC_{50} of 0.001−0.026 μM. This could explain the effectiveness in reducing the viral load in tested animal nasal turbinates. The methanol extract of mice lung tissues taken at the end of experiments contained several overlapped peaks in HPLC profile around the MW of compound **81**, making it difficult to determine the real concentration of the compound (data not shown).

4. Discussion

While two RdRp inhibitors and a $3CL^{pro}$ inhibitor which inhibit virus replication have been approved by FDA for treatment of COVID-19 patients, no compound targeting other essential components for SARS-CoV-2 infection has been approved. Although many $3CL^{pro}$ and PL^{pro} covalent and non-covalent inhibitors have already been identified, the small-molecule reversible inhibitors targeting virus entry, such as TMPRSS2, Furin, and RBD:ACE2 interaction, are relatively limited. Previously, Camostat and Nafamostat, have

doi:10.6342/NTU202400256

been identified to irreversibly inhibit TMPRSS2 and thus SARS-CoV-2 infection by blocking viral entry into cells (Hoffmann et al., 2020a,b). Some covalent peptidomimetic ketobenzothiazole inhibitors, which were developed based on the substrate specificity of TMPRSS2, showed anti-SARS-CoV-2 activity (Mahoney et al., 2021; Shapira et al., 2022). Animal study demonstrated the effectiveness of the TMPRSS2 irreversible inhibitor *in vivo* via intranasal treatment (7.2 mg/kg) 1 day before virus inoculation It remained half-effective when treated (14.4 mg/kg) 12 h after virus inoculation. These data demonstrated that the covalent TMPRSS2 inhibitors can be used for effective anti-SARS-CoV-2 treatment *in vitro* and *in vivo* by blocking the virus entry. However, the covalent inhibitors with the keto warhead but not the reduced hydroxyl analogue showed inhibition on TMPRSS2 and SARS-CoV-2, indicating the difficulty to develop reversible TMPRSS2 inhibitors for anti-SARS-CoV-2. Furin peptidomimetic covalent inhibitor decanoyl-RVKR-chloromethylketone has also been shown to inhibit SARS-CoV-2 entry into VeroE6 cells and thus virus production (Cheng et al., 2020). Several dyes (Congo red, direct violet 1, Evans blue) and drug-like compounds (DRI-C23041, DRI-C91005) inhibited the interaction of ACE2 with the spike proteins of SARS-CoV-2 with IC_{50} of 0.2–3.0 μM in the cell-free ELISA-type assays (Bojadzic et al., 2021). Here, we demonstrate the reversible inhibition of RBD:ACE2, TMPRSS2, and/or Furin as a novel and workable strategy for preventing SARS-CoV-2 entry and production.

We originally designed TMPRSS2/Furin dual reversible inhibitors, and as expected the compounds were active antivirals only if pretreating SARS-CoV-2 to block the virus entry, but not added after infection. Because some analogues that did not inhibit TMPRSS2 and Furin still inhibited the virus entry and production (Table 1), we then identified them

doi:10.6342/NTU202400256

as also RBD:ACE2 inhibitors. Our results thus indicate that the compounds exert their antiviral activities by inhibiting RBD:ACE2 interaction as a major factor, and inhibiting TMPRSS2 and/or Furin enhances their antiviral activities. The best inhibitor **2f** (**81**) displays great inhibition against TMPRSS2, Furin, and RBD:ACE2 interaction, respectively, with IC_{50} values of 1.27, 3.31, and 3.76 μM. It achieves EC_{50} values of 0.023 and 0.002 μM against SARS-CoV-2 delta and omicron variants, respectively, while infecting VeroE6 cells and CC_{50} >100 μM, giving the largest therapeutic index of >50000. By using lung Calu-3 cells, the EC_{50} were measured to be 0.026 and 0.001 μM, respectively, against SARS-CoV-2 delta and omicron variants. The preliminary animal study also demonstrates the effectiveness in reducing the viral load by 5−5.5-fold in nasal turbinate and safety without causing the animal weight loss while orally given a dose of 25 mg/kg into hamsters. Pharmacokinetics study shows higher concentrations of **81** in serum samples by IV injection than oral treatment, and both gave the concentrations above the antiviral EC_{50}. Further animal studies through different doses and ways of administration, and even in the presence of cytochrome P-450 inhibitor Ritonavir can be conducted to optimize the treatment effect in vivo.

For the antiviral mechanism, we show that compound **81** could inhibit the entry of SARS-CoV-2 pseudovirus into Calu-3 cells with an EC_{50} of 8.3 μM (Fig. 3E), but did not inhibit VSV-G pseudovirus into Calu-3 cells (Fig. 3F) as a control experiment because VSV-G pseudovirus entry is not dependent on RBD:ACE2, TMPRSS2, and Furin. We then show that the SARS-CoV-2 pseudovirus could only infect the HeLa-ACE2 stable cell line with enforcedly expressed ACE2 (Fig. 3G), but not the parental HeLa cells. These indicate that compound **81** only blocks ACE2-dependent entry of SARS-CoV-2 pseudoviruses by

doi:10.6342/NTU202400256

blocking RBD:ACE2 interaction. Moreover, we confirm that viral entry of Calu-3 could be inhibited by the specific TMPRSS2 inhibitor Camostat with an EC_{50} of 0.04 μM (Fig. 3H), but not by the Furin inhibitor decanoyl-RVKR-chloromethylketone (Fig. 3I). This is probably because Calu-3 cells express TMPRSS2 to replace the function of Furin in cleaving Spike for virus entry. As expected, Camostate did not inhibit pseudovirus entry into Hela-ACE2 cells that lack TMPRSS2 (Fig. 3J). However, as ACE2 and TMPRSS2 are both required for the viral entry into Calu-3 cells, to what extent blockade of ACE2 and/or TMPRSS2 by **81** accounted for inhibition of pseudoviral entry into Calu-3 cells is unclear. On the other hand, the anti-SARS-CoV-2 entry effect of decanoyl-RVKR-chloromethylketone was observed in TMPRSS2-limited VeroE6 cells where Furin is likely essential for virus entry (Cheng et al., 2020). Taken together, these data indicate that the entry of SARS-CoV-2 pseudovirus on Calu-3 cells is dependent on RBD:ACE2 interaction and TMPRSS2, but probably not Furin protease, although our compound **81** can inhibit all of these targets. Therefore, besides inhibiting RBD:ACE2 as the main factor for antiviral activity, the TMPRSS2 inhibitory activity of **81** could enhance its antiviral activity in Calu-3 cells, but inhibiting RBD:ACE2 and Furin could account for the antiviral activity of **81** in VeroE6 cells.

Our compounds contain a 4-styrylcarbonylphenyl, chalcone basic skeleton (chemical structure shown in Fig. 7A). Different chalcone derivatives have been shown to have anti-bacterial and anti-cancer activities by *in vitro* and *in vivo* experiments (Xu et al., 2019; Ouyang et al., 2021). Recently, chalcone derivatives (a chemical structure shown in Fig. 7B) were shown to inhibit SARS-CoV-2 replication in Vero E6 cells, and the targets were predicted to be RdRp, $3CL^{pro}$, and Spike's RBD by computer docking (Duran et al.,

doi:10.6342/NTU202400256

2021). A 7-(4-(N-substituted-carbamoyl-methyl)piperazin-1yl) ciprofloxacin-chalcone (chemical structure shown in Fig. 7C) was shown to inhibit $3CL^{pro}$ and SARS-CoV-2 (Alaaeldin et al., 2022). Besides chalcone, our best inhibitor **2f** also contains an indole moiety. There are few reports of similar indole chalcones (chemical structures shown in Fig. 7D–F) showing anti-inflammatory (Özdemir et al., 2015), anti-tumor (Yan et al., 2016), and anti-*Mycobacterium tuberculosis* (Mtb) (Ramesh et al., 2020) activities, respectively. Some indole chalcones were predicted by docking to target SARS-CoV-2 RdRp, $3CL^{pro}$, and/or Spike's RBD (Vijayakumar et al., 2020), but further experiments are required to confirm the prediction. Indole seems to increase the compound affinity with the SARS-CoV-2 $3CL^{pro}$ and a compound with indole ring was shown to reversibly bind with the protease (Hattori, 2021). Ghosh et al. also reported indole chloropyridinyl ester-derived SARS-CoV-2 $3CL^{pro}$ inhibitors (Ghosh et al., 2021). On the other hand, indole derivatives were shown by silicon screening to bind Spike protein of SARS-CoV-2 (Gobinath et al., 2021).

In summary, compound **2f** (**81**) containing chalcone and indole moieties obeys the Lipinski's and Veber's rules and hence displays drug-like molecular nature. Not only the lung Calu-3 cell-based assay, our preliminary *in vivo* animal study also shows the promising effectiveness and safety of the lead compound. While the therapeutic antibody drugs used to prevent virus entry into cells are expensive and are prone to reduce treatment sensitivity once encountering the mutations on Spike, our small-molecule potent antiviral effective among different variants of SARS-CoV-2 could be a useful alternative for treatment. In conclusion, we have successfully identified promising inhibitors of SARS-CoV-2 by reversibly blocking the essential targets at the virus entry.

doi:10.6342/NTU202400256

Table 1. Compounds **2a**–**g** inhibiting TMPRSS2, Furin, RBD:ACE2 and SARS-CoV-2

Entry	Compd	Ar	IC_{50} (μM)			EC_{50} (μM)	CC_{50} (μM)
			RBD:ACE2	Furin	TMPRSS2	SARS-CoV-2	VeroE6
1	**2a** (**100**)		16.55 ± 3.92	23.12 ± 2.35	28.35 ± 2.46	0.26 ± 0.06	>100
2	**2b** (**22**)	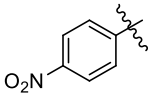	7.15 ± 1.52	10.14 ± 1.12	12.46 ± 0.95	0.15 ± 0.10	>100
3	**2c** (**89**)	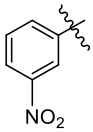	16.97 ± 4.92	18.89 ± 2.30	18.20 ± 1.45	0.70 ± 0.18	>100
4	**2d** (**105**)		28.14 ± 8.17	>50	>50	1.06 ± 0.54	>100
5	**2e** (**143**)	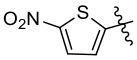	2.81 ± 0.49	4.55 ± 0.69	3.52 ± 0.55	0.087 ± 0.010	59.9 ± 0.99
6	**2f** (**81**)	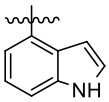	3.76 ± 0.84	3.31 ± 0.52	1.27 ± 0.08	0.023 ± 0.005/0.002 ± 0.002[a] 0.026 ± 0.012/0.001 ± 0.0007[b]	>100
7	**2g** (**321**)	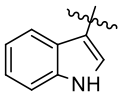	33.99 ± 11.42	>50	>50	3.78 ± 0.60	>100

[a]The EC_{50} of **81** for inhibiting delta/omicron BA.1 SARS-CoV-2 infecting VeroE6 cells.
[b]The EC_{50} of **81** for inhibiting delta/omicron BA.1 SARS-CoV-2 infecting Calu-3 cells.

doi:10.6342/NTU202400256

Table 2. Compounds **4a** and **4b** inhibiting TMPRSS2, RBD:ACE2, and SARS-CoV-2

Entry	Compd	Ar	IC_{50} (μM)			EC_{50} (μM)	CC_{50} (μM)
			RBD:ACE2	Furin	TMPRSS2	SARS-CoV-2	VeroE6
1	**4a** (**180**)		25.04 ± 9.26	>50	>50	2.09 ± 0.06	>100
2	**4b** (**285**)	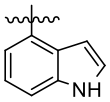	51.72 ± 51.84	>50	31.64 ± 2.93	0.67.± 0.38	>100

Table 3. Pharmacokinetic parameters of compound **81** in K18-hACE2 transgenic mice following oral administration or intravenous (IV) injection (25 mg/kg)

Parameters	Unit	oral administration	IV injection
λ	1/h	0.51	0.43
$t_{1/2\,\lambda}$	h	1.35	1.59
AUC	μM·h	1.58	4.48
MRT	h	2.00	1.79

Note: The pharmacokinetic parameters of compound **81** were determined by a non-compartmental model. λ, terminal rate constant; $t_{1/2\lambda}$, terminal half-life; AUC, area under the serum concentration-time curve; MRT, mean residence time.

doi:10.6342/NTU202400256

Table 4. The properties of **2f** (**81**) analyzed using Lipinski rule of five

Properties	Predicted value
Molecular weight	374 Da
Hydrogen bond donors	2
Hydrogen bond acceptors	5
LogP	3.501499
Molar refractivity	106.200974

Table 5. The ADMET profile of compound **2f** (**81**)

Properties	Predicted value
Absorption	
Water solubility (log mol/L)	-4.836
Caco2 permeability (log Papp in 10^{-6} cm/s)	1.029
Intestinal absorption (human) (% Absorbed)	97.014
Skin Permeability (log Kp)	-2.722
P-glycoprotein substrate	Yes
P-glycoprotein I inhibitor	No
P-glycoprotein II inhibitor	No
Distribution	
VDss (human) (log L/kg)	-0.674
Fraction unbound (human) (Fu)	0

doi:10.6342/NTU202400256

BBB permeability (log BB)	-0.395
CNS permeability (log PS)	-2.301
Metabolism	
CYP2D6 substrate	No
CYP3A4 substrate	Yes
CYP1A2 inhibitor	No
CYP2C19 inhibitor	No
CYP2C9 inhibitor	No
CYP2D6 inhibitor	No
CYP3A4 inhibitor	No
Excretion	
Total Clearance (log ml/min/kg)	0.477
Renal OCT2 substrate	No
Toxicity	
AMES toxicity	No
Max. tolerated dose (human) (log mg/kg/day)	0.703
hERG I inhibitor	No
hERG II inhibitor	No
Oral Rat Acute Toxicity (LD_{50}) (mol/kg)	3.186
Oral Rat Chronic Toxicity (LOAEL) (log mg/kg_bw/day)	1.879
Hepatotoxicity	Yes

doi:10.6342/NTU202400256

Skin Sensitization	No
T.Pyriformis toxicity (log ug/L)	0.415
Minnow toxicity (log mM)	0.443

doi:10.6342/NTU202400256

5. Figure Legends

Fig. 1

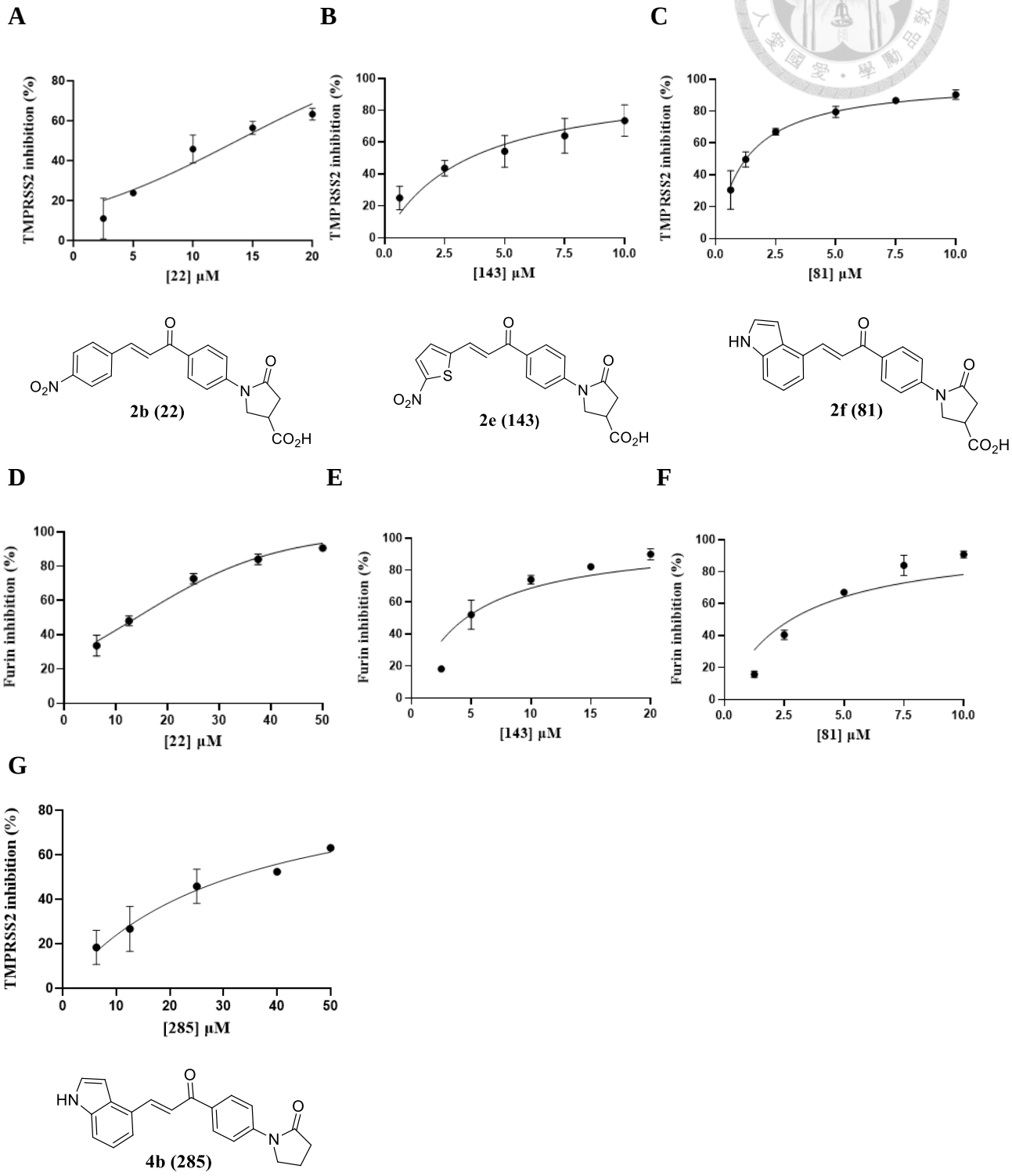

doi:10.6342/NTU202400256

Fig. 1. Dose-dependent inhibition curves of the representative inhibitors **2b** (**22**), **2e** (**143**), and **2f** (**81**) against TMPRSS2 (A−C) and Furin (D−F). In (A−C), the increasing inhibition percentages of TMPRSS2 activity in the presence of increasing concentrations of **2b**, **2e**, and **2f** were fitted with the equation to yield the IC_{50} of 12.46 ± 0.95, 3.52 ± 0.55, and 1.27 ± 0.08 μM, respectively. In (D−F), the increasing inhibition percentages of Furin activity in the presence of increasing concentrations of **2b**, **2e**, and **2f** were fitted with the equation to yield the IC_{50} of 10.14 ± 1.12, 4.55 ± 0.69, and 3.31 ± 0.52 μM, respectively. (G) The increasing inhibition percentages of TMPRSS2 activity in the presence of increasing concentrations of **4b** (**285**) were fitted with the equation to yield the IC_{50} of 31.64 ± 2.93 μM. All the measurements were performed in triplicate to yield the averaged IC_{50} values and the standard deviations.

doi:10.6342/NTU202400256

Fig. 2

A

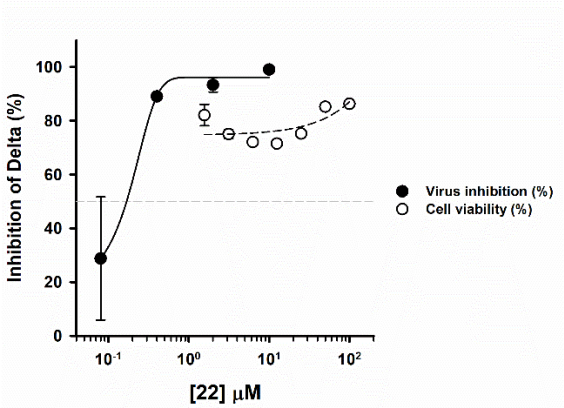

B

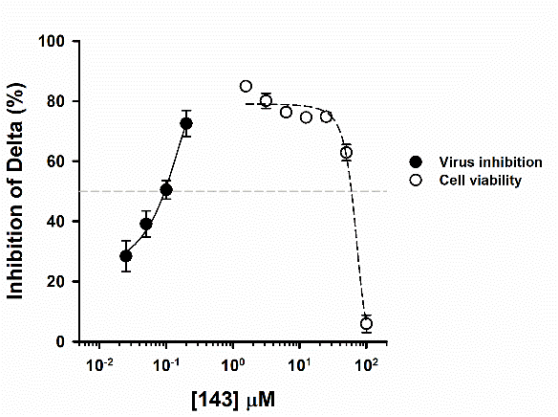

C

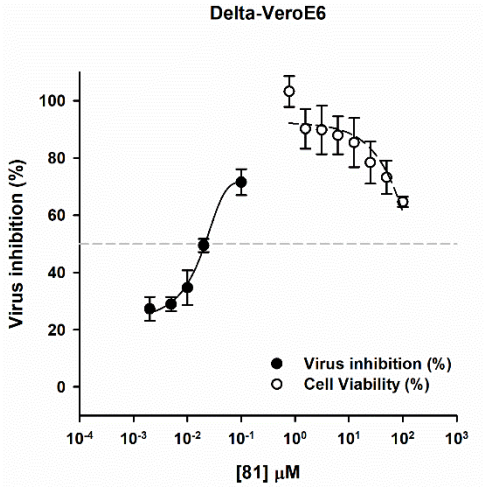

D

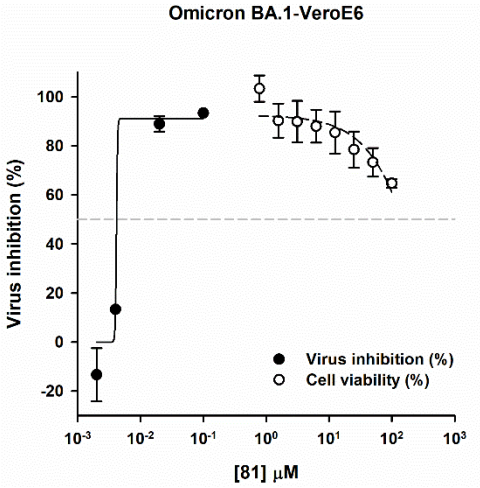

E

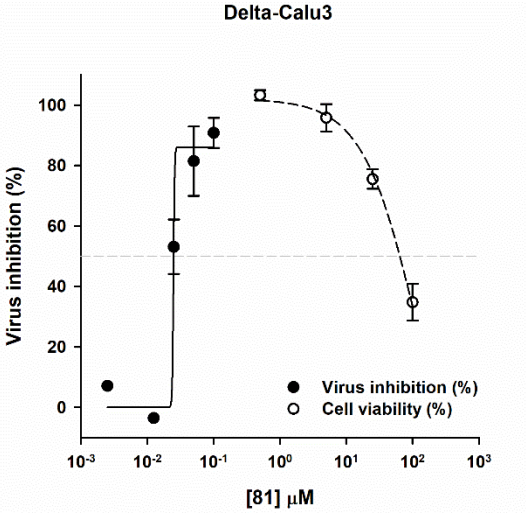

F

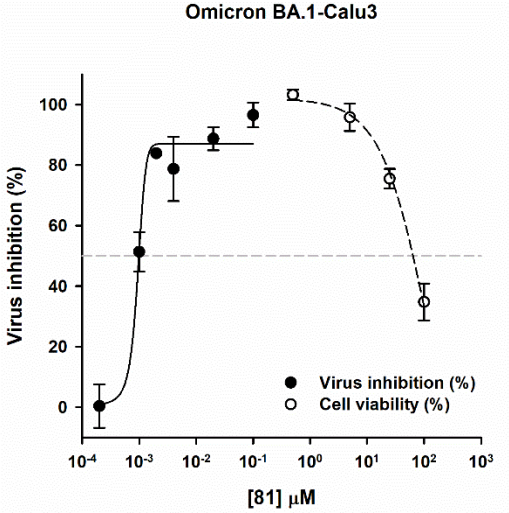

doi:10.6342/NTU202400256

Fig. 2. Dose-dependent inhibition curves of the representative inhibitors **2b** (**22**), **2e** (**143**), and **2f** (**81**) against SARS-CoV-2. In (A−C), the plaque reduction assay was performed to determine the EC_{50} of **2b**, **2e**, and **2f** to be 0.15 ± 0.10, 0.087 ± 0.010, and 0.023 ± 0.005 μM, respectively, against the delta strain of SARS-CoV-2 (NTU92) infecting VeroE6 cells at 50−100 pfu for 1 h at 37 °C. The X-axis concentrations adopt the log base 10 scale. (D) The EC_{50} of **81** was determined to be 0.002 ± 0.002 μM against the omicron BA.1 strain (NTU128) infecting VeroE6 cells at 50−100 pfu for 1 h at 37 °C based on **81**-caused virus plaque reduction. (E, F) The dose-dependent inhibition on the virus yield by pretreating **81** with delta or omicron strain was used to determine the EC_{50} of **81** to be 0.026 ± 0.012 and 0.001 ± 0.0007 μM, respectively, against the delta and omicron BA.1 SARS-CoV-2 infecting Calu-3 cells at 50−100 pfu for 1 h at 37 °C based on **81**-caused virus plaque reduction. The drop of Calu-3 cell viability was due to higher concentrations of DMSO at higher concentrations of **81**. All the measurements were performed in triplicate to yield the averaged EC_{50} values and the standard deviations.

doi:10.6342/NTU202400256

Fig. 3

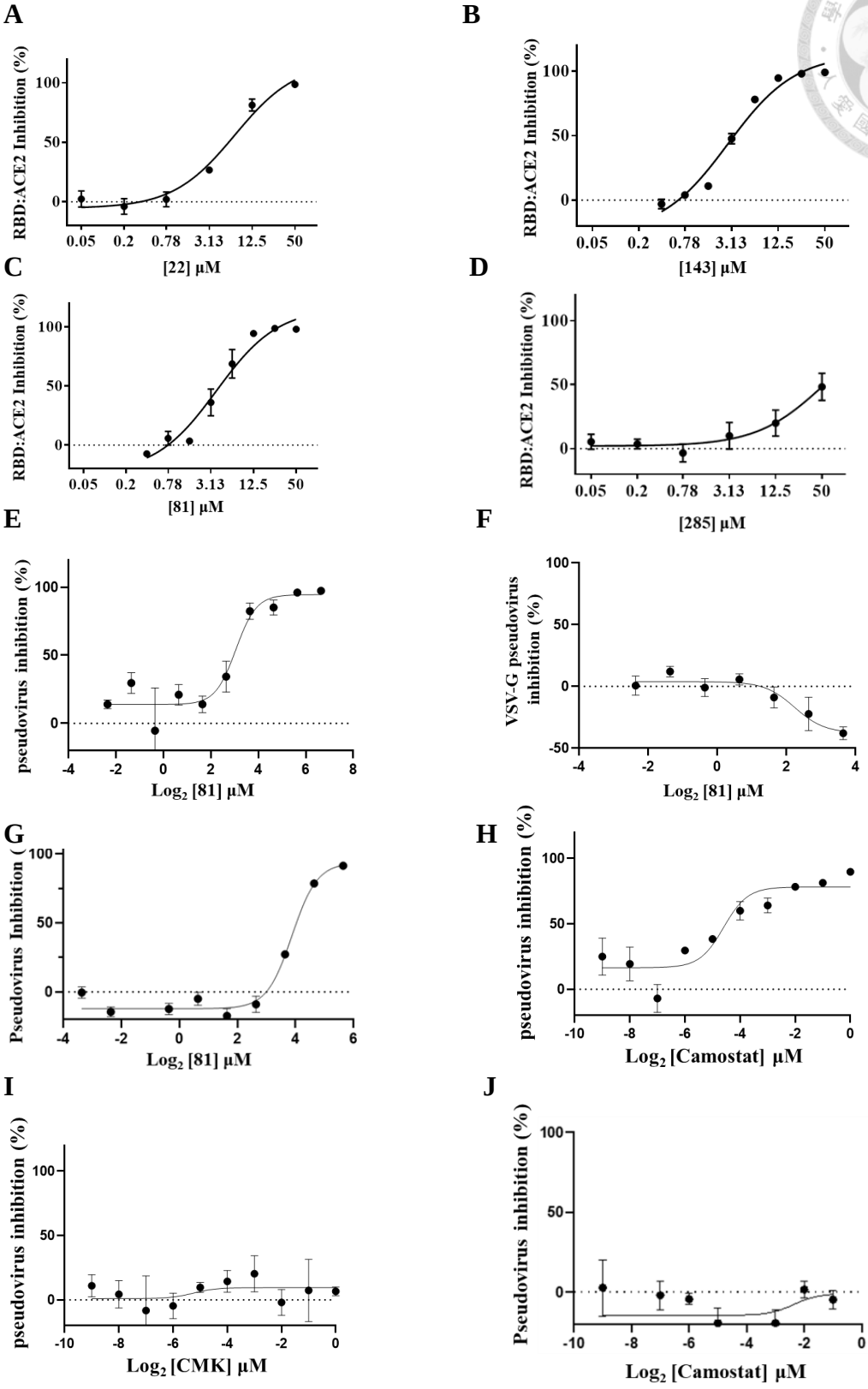

doi:10.6342/NTU202400256

Fig. 3. The dose-dependent inhibition curves of the compounds on delta strain Spike's RBD:ACE2 interaction and pseudovirus. (A−C) The increasing inhibition percentages of RBD:ACE2 interaction in the presence of increasing concentrations of **2b** (**22**), **2e** (**143**), and **2f** (**81**) were fitted with the equation to yield the IC_{50} of 7.15 ± 1.52, 2.81 ± 0.49, and 3.76 ± 0.84 μM, respectively. The X-axis concentrations adopt the log base 2 scale. (D) The inhibition percentages on RBD:ACE2 binding were increased with increased concentrations of **4b** (**285**). The plot gave EC_{50} of 51.72 ± 51.84 μM. In the above measurements, Hela cells expressing SmBiT-tagged human ACE2 and the recombinant RBD-LgBiT protein were mixed to form decreasing levels of an active NanoLuc complex, a luciferase, to be assayed using the provided substrate in the presence of increasing concentrations of synthesized inhibitors to yield IC_{50}. (E) The does-dependent curve for inhibiting delta Spike pseudovirus entry into Calu-3 cells by **2f** (**81**) to yield EC_{50} of 8.3 ± 1.2 μM. (F) Infection of Calu-3 cells by VSV-G Pseudovirus was not inhibited by **81**. (G) Infection of Hela-ACE2 cells by pseudovirus was inhibited by compounds **81** with EC_{50} of 14.7 ± 1.1 μM. (H) Specific TMPRSS2 covalent inhibitor Camostat inhibited pseudovirus infection on Calu-3 cells with EC_{50} of 0.04 ± 0.001 μM. (I) Specific Furin covalent inhibitor decanoyl-RVKR-chloromethylketone (CMK) showed no effect on pseudovirus infection on Calu-3 cells. (J) Camostat showed no effect on pseudovirus infection on HeLa-ACE2 cells. All the measurements were performed in triplicate to yield the averaged IC_{50} or EC_{50} values and the standard deviations.

doi:10.6342/NTU202400256

Fig. 4

A

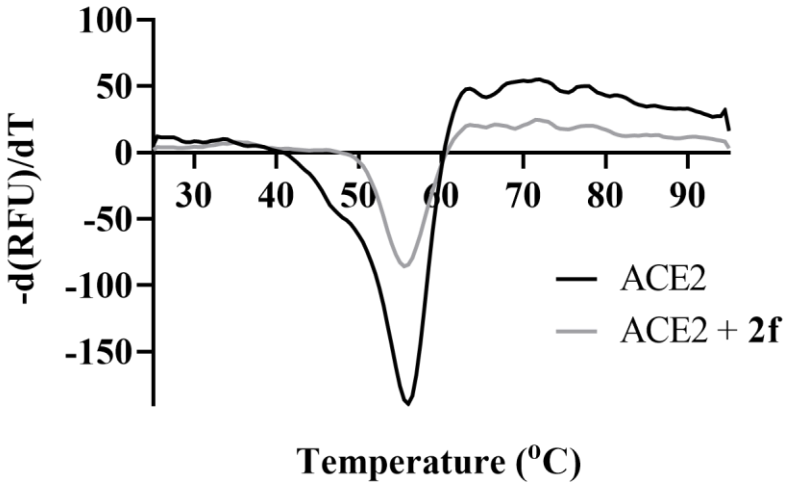

B

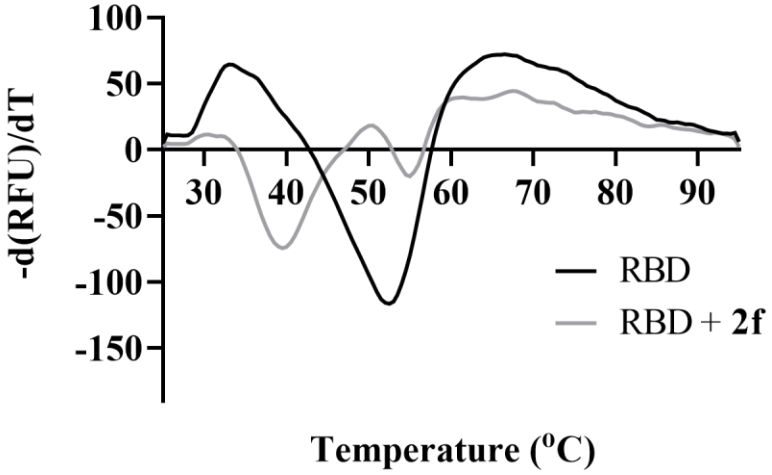

doi:10.6342/NTU202400256

Fig. 4. Thermal shift experiments to measure the binding partner of **2f** (**81**). (A) Melting temperature change was not observed for adding **2f** to ACE2 (A), but obvious to RBD (B), based on the differential scanning fluorimetry assay, indicating RBD as the binding partner of **2f**. In this assay, a fluorescent dye was bound to the exposed surface on the heat-induced unfolded protein RBD or ACE2. The temperatures causing the maximal unfolding of the proteins (the peaks) were defined as melting temperatures. The curves were obtained from a single run of experiments with repeatable results.

doi:10.6342/NTU202400256

Fig. 5

A

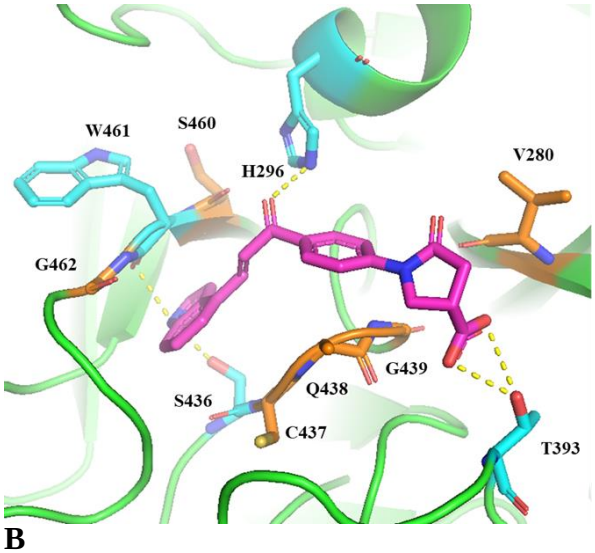

B

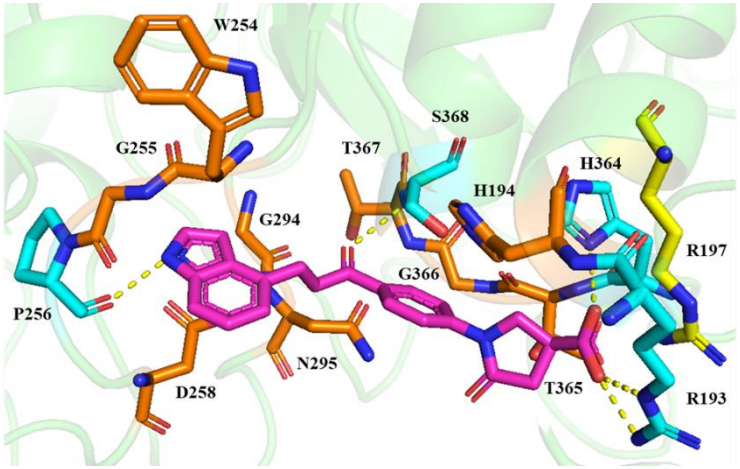

C

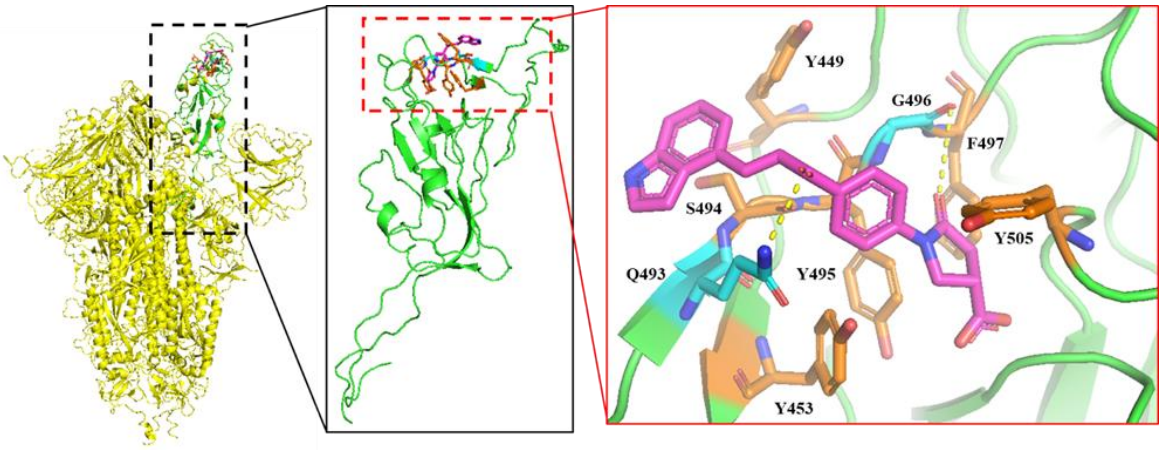

doi:10.6342/NTU202400256

Fig. 5. Compound **2f** (**81**) was docked into (A) the TMPRSS2 ectodomain (PDB: 7meq), (B) Furin (PDB: 5jxg), and (C) RBD of the delta-strain Spike protein (PDB: 7w92). The estimated binding energies of **2f** with TMPRSS2, Furin, and RBD are -115.8, -118.9, and -115.1 kcal/mol, respectively. Compound **2f** is colored in magenta, and the residues colored in cyan, orange, and yellow are involved in hydrogen-bonding, van der Waals, and electrostatic interactions, respectively. In (C), colored in yellow is trimeric Spike protein and in green is RBD. **2f** binds with the residues of RBD in the interface to interfere with the RBD binding with ACE2.

doi:10.6342/NTU202400256

Fig. 6

A

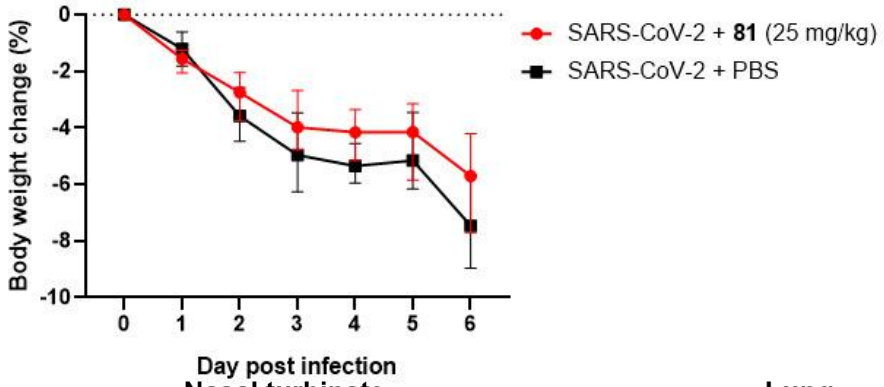

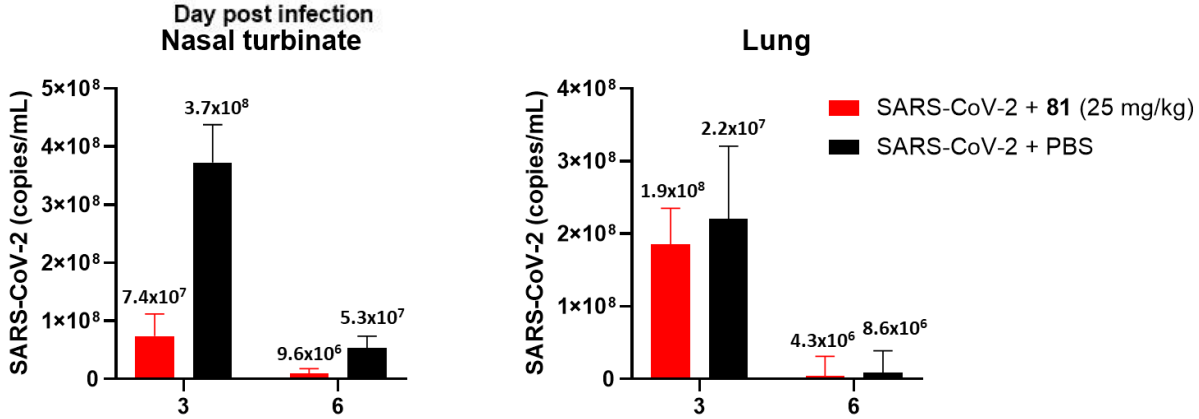

C

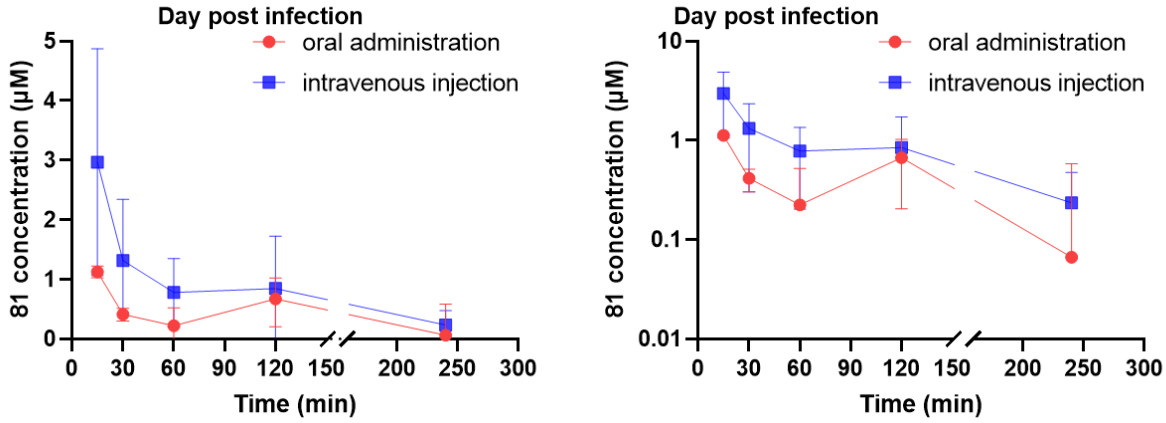

doi:10.6342/NTU202400256

Fig. 6. Body weight changes and viral loads of Syrian hamsters infected intranasally with SARS-CoV-2 with or without **2f** (**81**) oral treatment. (A) Time courses of body weight percent changes from the averages of three hamsters with treatment of 25 mg/kg shown in red and the averages of three without treatment (only PBS) shown in black. (B) Corresponding virus genome copy numbers as determined by qRT-PCR in nasal turbinate (left) and lung (right) from the averages of three hamsters with treatment of 25 mg/kg shown in red and the averages of three without treatment (only PBS) shown in black. (C) Linear (left) and semi-logarithmic (right) plots of the serum concentration-time profile of compound **81** following oral administration or intravenous injection (25 mg/kg). The serum samples obtained from the mice before treatment and 15, 30, 60, 120, and 240 min after oral administration or IV injection of 25 mg/kg compound **81** were subjected to LC-MS to determine the concentrations shown in red and blue dots for oral and injection treatment, respectively. Data represented are mean ± SD. Apparently, IV injection yielded higher serum concentrations of **81** than oral treatment, but both gave the concentrations above the antiviral EC_{50}.

doi:10.6342/NTU202400256

Fig. 7

A

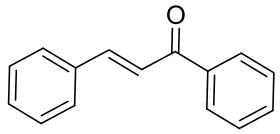

Chalcone

B

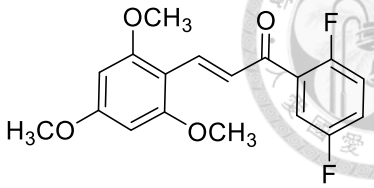

(effective at 1.6 μg/mL)

C

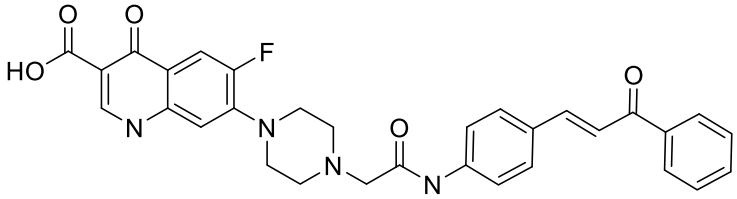

ciprofloxacin-chalcone (EC_{50} = 3.93 nM, 10 μM<CC_{50} <100 μM)

D

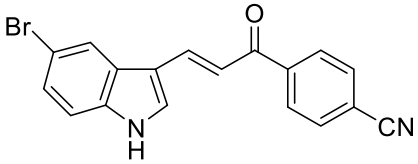

(IC_{50} = 8.1 and 9.5 μM against COX-1 and -2)

E

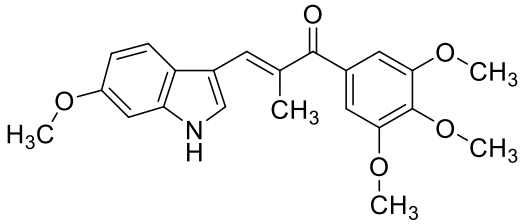

(EC_{50} = 3 nM against A549)

F

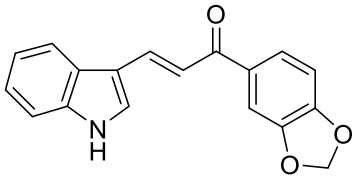

(MIC = 171 μM against *Mtb*)

doi:10.6342/NTU202400256

Fig. 7. Chemical structures of some biologically active chalcones. These include the chemical structures of (A) chalcone, (B) a chalcone derivative shown to inhibit SARS-CoV-2 viral growth in Vero E6 cell (effective at 1.6 μg/mL) by targeting RdRp, $3CL^{pro}$, and Spike's RBD as predicted by computer docking, (C) 7-(4-(N-substituted-carbamoyl-methyl)piperazin-1yl) ciprofloxacin-chalcone shown to inhibit $3CL^{pro}$ and SARS-CoV-2, and (D-F) indole chalcones possessing anti-inflammatory, anti-tumor, and anti-*Mycobacterium tuberculosis* activities, respectively.

doi:10.6342/NTU202400256

Fig. S2

A

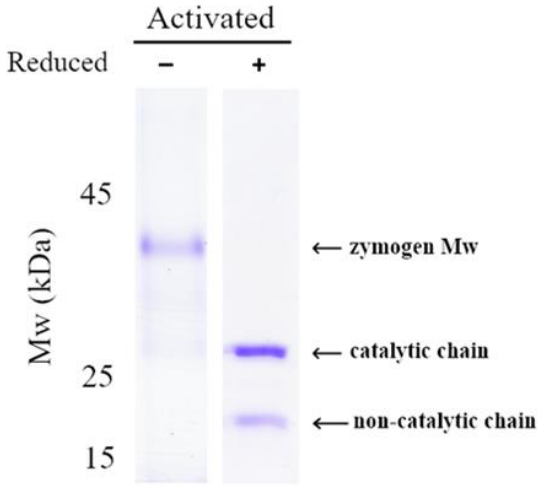

B

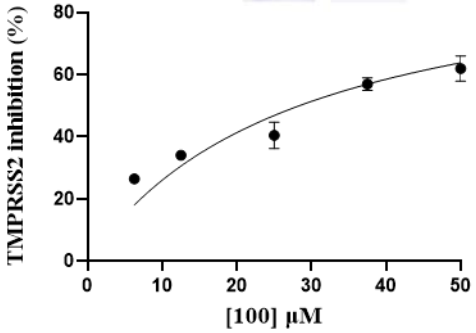

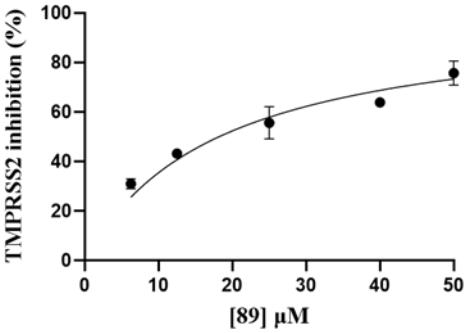

doi:10.6342/NTU202400256

Fig. S2. (A) SDS-PAGE analysis of the purified and activated TMPRSS2 ectodomain. The TMPRSS2 ectodomain was expressed and purified as described in Materials and Methods. (B) Dose-response curves (inhibition percentages vs. inhibitor concentrations) of the TMPRSS2 inhibitors **2a** (**100**) and **2c** (**89**). All the measurements were performed in triplicate to yield the averaged IC_{50} values and the standard deviations.

doi:10.6342/NTU202400256

Fig. S3.

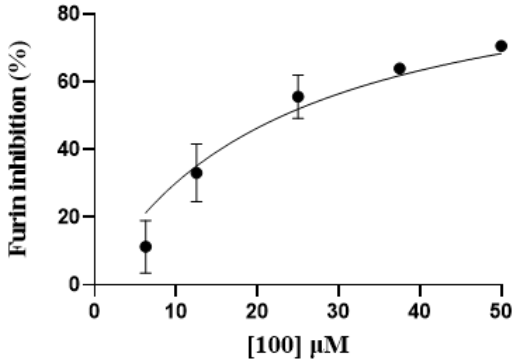

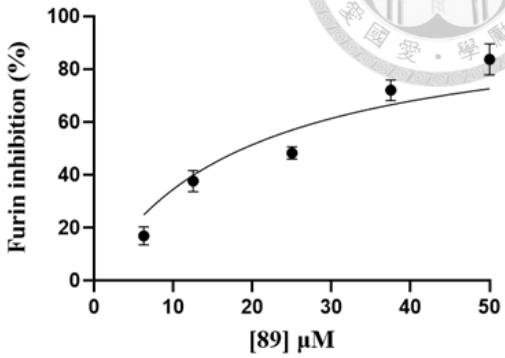

doi:10.6342/NTU202400256

Fig. S3. Dose-response curves (inhibition percentages vs. inhibitor concentrations) of the Furin inhibitors **2a** (**100**) and **2c** (**89**). Furin and the assay reagents were included in a commercial kit. All the measurements were performed in triplicate to yield the averaged IC_{50} values and the standard deviations.

doi:10.6342/NTU202400256

Fig. S4.

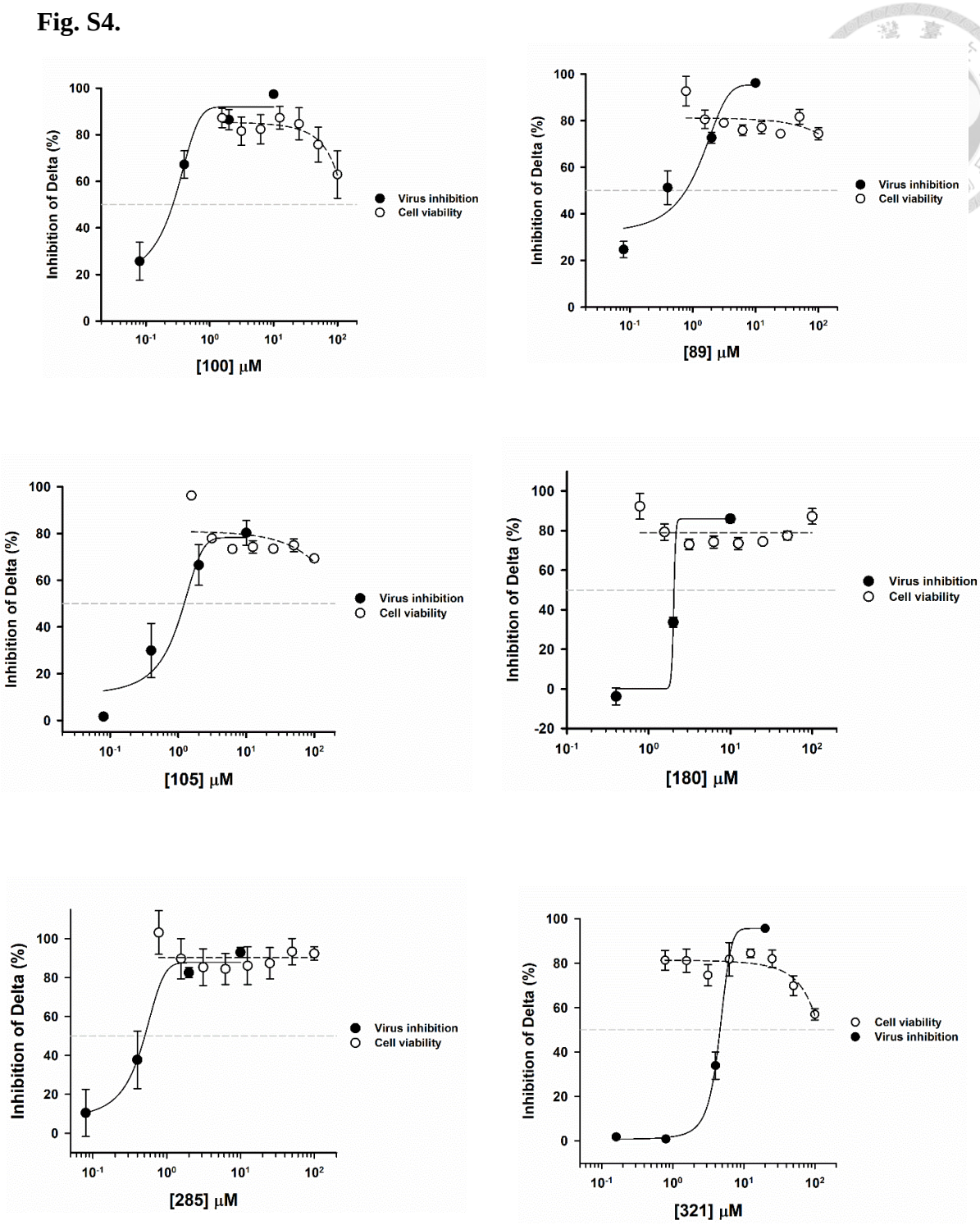

doi:10.6342/NTU202400256

Fig. S4. Antiviral activities against delta SARS-CoV-2 and cytotoxicity of test compounds. Dose-dependent inhibition by the other inhibitors **2a** (**100**), **2c** (**89**), **2d** (**105**), **2g** (**321**), **4a** (**180**), and **4b** (**285**) against delta variant of SARS-CoV-2 infecting VeroE5 cells at 50−100 pfu for 1 h at 37 °C shown in filled circles for EC_{50} measurements and changes of VeroE6 cell viability with different concentrations of inhibitors shown in open circles for CC_{50} determination. As shown in Table 1, the determined EC_{50} and CC_{50} were averages of three measurements to yield the standard deviations. The X-axis concentrations adopt the log base 10 scale.

doi:10.6342/NTU202400256

Fig. S5.

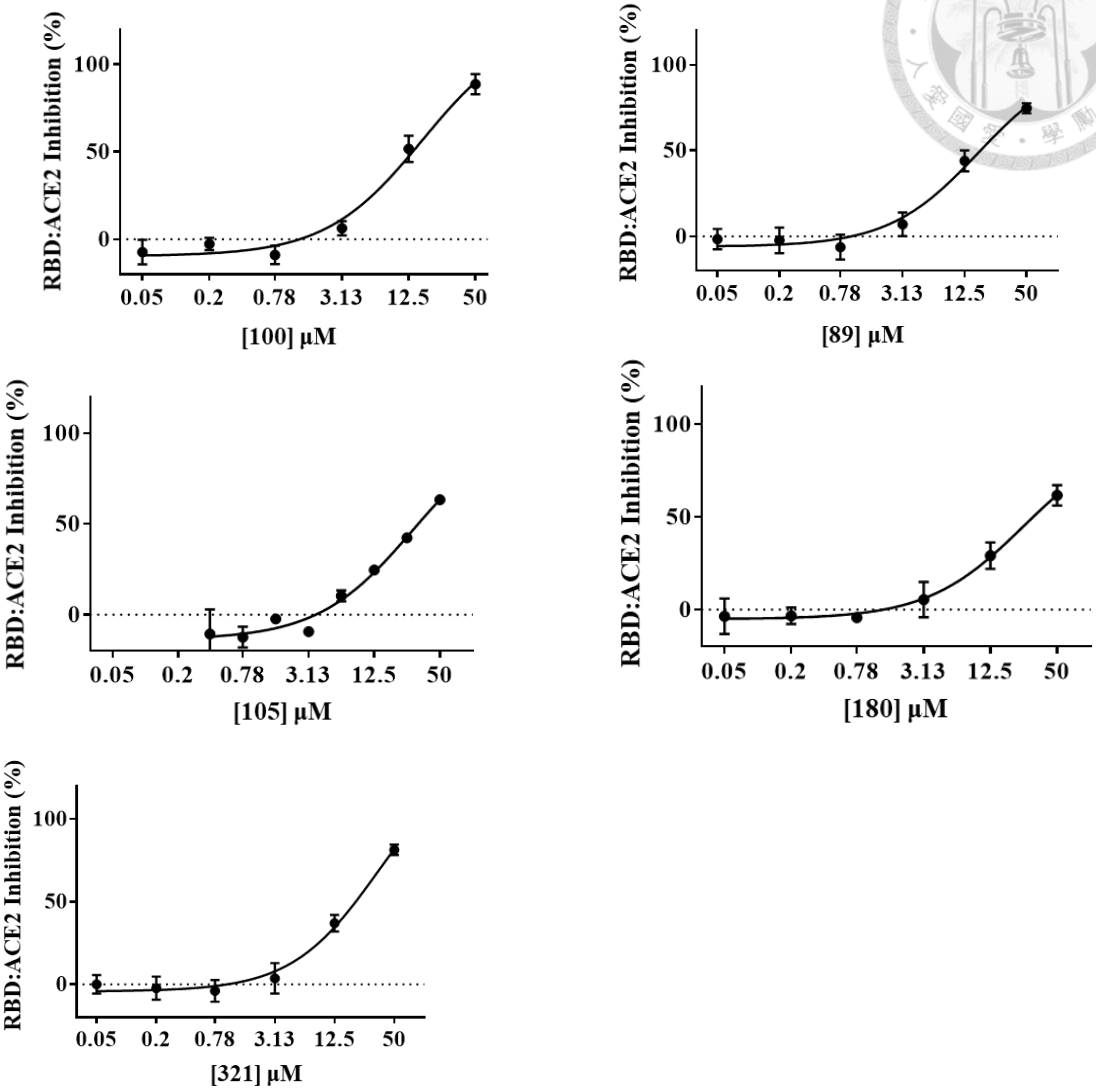

doi:10.6342/NTU202400256

Fig. S5. Dose-dependent curves for inhibiting RBD:ACE2 interaction probed by using the cell-based assay. Hela cells expressing SmBiT-tagged human ACE2 and the recombinant RBD-LgBiT protein were mixed to form decreasing levels of an active Bit complex, a luciferase, to be assayed using the provided substrate in the presence of increasing concentrations of synthesized inhibitors. The increasing inhibition percentages of RBD:ACE2 interaction in the presence of increasing concentrations of **2a** (**100**), **2c** (**89**), **2d** (**105**), **2g** (**321**), and **4a** (**180**) were fitted with the equation to yield the IC_{50} of 7.15 ± 1.52, 2.81 ± 0.49, and 3.76 ± 0.84 μM, respectively. The determined IC_{50} were averages of three measurements to yield standard deviations. The X-axis inhibitor concentrations adopt the log base 2 scale.

doi:10.6342/NTU202400256

Fig. S6.

A

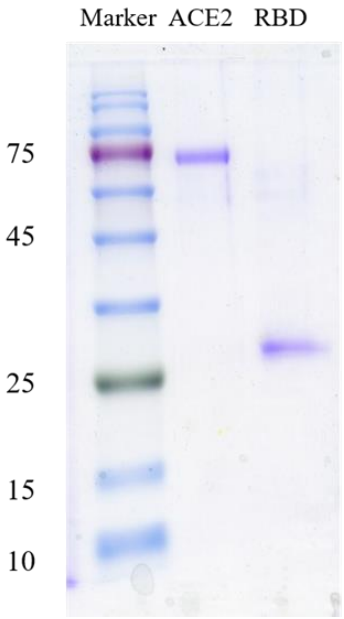

B

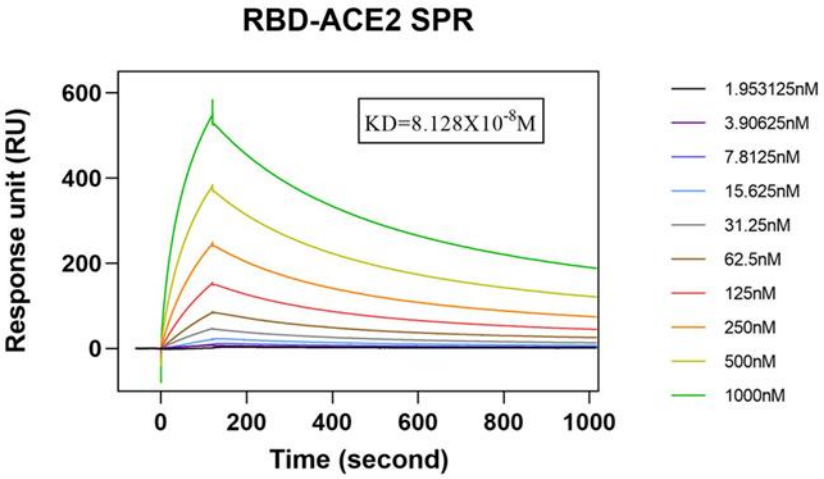

doi:10.6342/NTU202400256

Fig. S6. Preparation and characterization of recombinant RBD and ACE2. (A) SDS-PAGE analysis of the purified recombinant RBD and ACE2. (B) Their interaction probed by Biacore to yield a K_d of 8.128 x10^{-8} M (81.28 nM). For the Biacore experiments using a Biacore T200 surface plasmon resonance instrument (cytiva, MA, USA), RBD was immobilized on a CM5 sensor chip with an amine coupling kit and the two-fold serially diluted ACE2, starting at a concentration of 1000 nM, was injected into the flow channels in running buffer (PBS, pH 7.4, and 0.05% Tween 20) at a flow rate of 30 μL/min for 120 s at 25 °C. The obtained signals were subtracted from the reference channel not coated with RBD. The binding curves (sensorgrams) were fitted with 1:1 binding model using the Biacore T200 evaluation software (GE Healthcare, USA) to yield the K_d.

doi:10.6342/NTU202400256

6. Spectral data

1-(4-Acetylphenyl)-4-carboxy-2-pyrrolidinone (1)

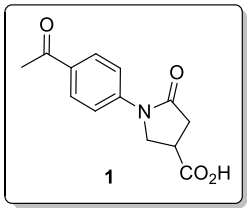

A mixture of 4-aminoacetophenone (1 g, 7.40 mmol) and itaconic acid (1.2 g, 8.89 mmol) was stirred at 110–130 ºC for 18 h. After cooling to room temperature, 10 mL of methanol was added to the reaction mixture. The reaction mixture was sonicated under mild heating to dissolve the contents in methanol, and then cooled to room temperature for recrystallization. The crystallized product was filtered and washed with ethyl acetate to afford the pure product. The pyrrolidinone **1** was obtained as white crystals (49.8% yield), mp 180–181 ºC, ^{1}H NMR (400 MHz, DMSO-d_6): δ 12.81 (s, 1H), 7.99 (d, *J* = 8.8 Hz, 2H), 7.83 (d, *J* = 8.88 Hz, 2H), 4.14–4.01 (m, 2H), 3.41–3.32 (m, 1H), 2.88–2.72 (m, 2H), 2.56 (s, 3H) ppm. ^{13}C NMR (100 MHz, DMSO-d_6): δ 196.64, 174.02, 172.57, 143.10, 132.09, 129.15, 118.41, 49.78, 35.32, 35.01, 26.49 ppm. HRMS (ESI): *m/z* calcd. for $C_{13}H_{14}NO_4^+$ $[M+H]^+$: 248.0917, found 248.0929.

1-(4-Styrylcarbonylphenyl)-4-carboxy-2-pyrrolidinone (2a)

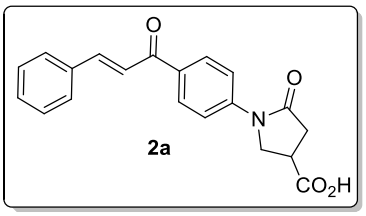

A mixture of 1-(4-acetylphenyl)-4-carboxy-2-pyrrolidinone **1** (2.47 g, 10 mmol), benzaldehyde (15 mmol) and 15 mL of 10% NaOH in 10 mL of ethanol was refluxed for

doi:10.6342/NTU202400256

4 h and cooled to room temperature. Then, 15 mL of water was added and the mixture was acidified to pH 1–2 with aq. HCl. The precipitate was filtered and washed with water. The product **2a** was obtained as light-yellow solid (yield 70.0%), mp 209–210 °C, ^{1}H NMR (400 MHz, DMSO-d_6): δ 12.87 (s, 1H), 8.20 (d, *J* = 8.68 Hz, 2H), 7.10–7.90 (m, 5H), 7.77 (d, *J* = 15.48 Hz, 1H), 7.48 (t, *J* = 5.28 Hz, 3H), 4.18–4.05 (m, 2H), 3.43–3.31 (m, 1H), 2.89–2.74 (m, 2H) ppm. ^{13}C NMR (100 MHz, DMSO-d_6): δ 188.18, 174.51, 173.11, 144.08, 143.69, 135.22, 133.21, 131.02, 130.08, 129.38, 129.33, 122.44, 199.04, 50.30, 35.85, 35.52 ppm. HRMS (ESI): *m/z* calcd. for $C_{20}H_{18}NO_4^+$ $[M+H]^+$: 336.1230, found 336.1246.

6.3. 1-(4-(4-Nitrostyrylcarbonyl)phenyl)-4-carboxy-2-pyrrolidinone (2b)

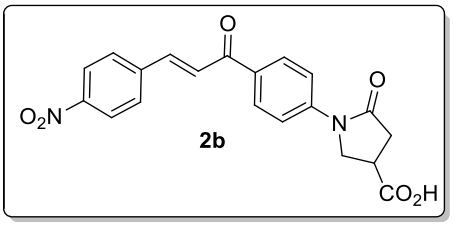

The compound **2b** was prepared by following the procedure described for the synthesis of 2**a**, by using 4-nitrobenzaldehyde. Light yellow solid (yield 30.2%), mp 224–225 °C, ^{1}H NMR (400 MHz, DMSO-d_6): δ 12.90 (s, 1H), 8.30 (q, *J* = 8.8 Hz, 4H), 8.12 (q, *J* = 1.9 Hz, 3H), 7.90 (q, *J* = 8.9 Hz, 3H), 4.18–4.04 (m, 2H), 3.44–3.36 (m, 1H), 2.90–2.74 (m, 2H) ppm. ^{13}C NMR (100 MHz, DMSO-d_6): δ 187.95, 174.50, 173.20, 148.51, 143.98, 141.74, 141.20, 132.79, 130.32, 126.47, 124.39, 119.03, 50.31, 35.87, 35.53 ppm. HRMS (ESI): *m/z* calcd. for $C_{20}H_{17}N_2O_6^+$ $[M+H]^+$: 381.1081, found 381.1075.

doi:10.6342/NTU202400256

6.4. 1-(4-(3-Nitrostyrylcarbonyl)phenyl)-4-carboxy-2-pyrrolidinone (2c)

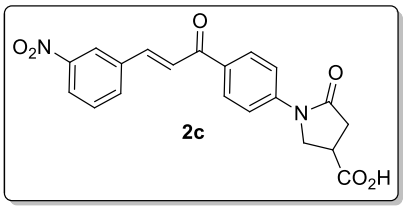

The compound **2c** was prepared by using the procedure described for the synthesis of **2a**, with 3-nitrobenzaldehyde. Light yellow solid (yield 63.9%), mp 234–235 °C, ^{1}H NMR (400 MHz, DMSO-d_6): δ 8.77 (s, 1H), 8.34 (d, *J* = 7.64 Hz, 1H), 8.27–2.23 (m, 3H), 8.10 (d, *J* = 15.64 Hz, 1H), 7.89 (t, *J* = 12.32 Hz, 2H), 7.82 (s, 1H), 7.76 (t, *J* = 15.8 Hz, 1H). 4.15–4.03 (m, 2H), 3.38–3.210 (m, 1H), 2.90–2.80 (m, 2H) ppm. ^{13}C NMR (100 MHz, DMSO-d_6): δ 187.48, 174.15, 172.93, 148.39, 143.49, 140.99, 136.64, 135.04, 132.30, 130.30, 129.80, 124.68, 124.55, 122.98, 118.45, 50.07, 35.60, 35.35 ppm. HRMS (ESI): *m/z* calcd. for $C_{20}H_{15}N_2O_6^-$ $[M+H]^-$: 379.0936, found 379.0902.

6.5. 1-(4-(3-(Furan-2-yl)acryloyl)phenyl)-4-carboxy-2-pyrrolidinone (2d)

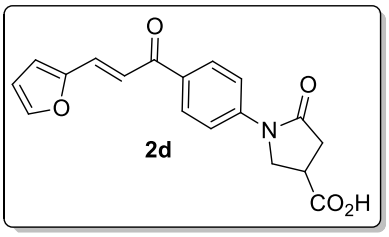

The compound **2d** was prepared by following the procedure described for the synthesis of **2a**, by using furan-2-carboxaldehyde. Brown solid (yield 49.7%), mp 205–206 °C, ^{1}H NMR (400 MHz, DMSO-d_6): δ 12.82 (s, 1H), 8.13 (d, *J*= 8.7 Hz, 2H), 7.10 (t, *J* = 8.6, Hz, 3H), 7.60 (s, 2H), 7.12 (d, *J* = 3.3 Hz, 1H), 6.71–6.10 (m, 1H), 4.17–4.03 (m, 2H), 3.43–3.35 (m, 1H), 2.80–2.73 (m, 2H) ppm. ^{13}C NMR (100 MHz, DMSO-d_6): δ 187.10, 174.02, 172.61, 151.17, 146.12, 143.12, 132.64, 130.12, 129.34, 118.58, 116.90, 113.10, 49.79,

doi:10.6342/NTU202400256

35.34, 35.02 ppm. HRMS (ESI): *m/z* calcd. for $C_{18}H_{16}N_2O_5^+$ $[M+H]^+$: 326.1028, found 326.0970.

6.6. 1-(4-(3-(5-Nitrothiophene-2-yl)acryloyl)phenyl)-4-carboxy-2-pyrrolidinone (2e)

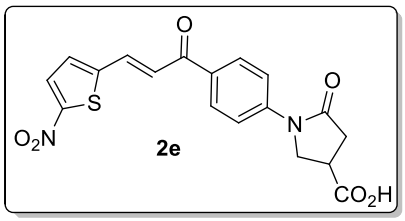

The compound **2e** was prepared by following the procedure described for the synthesis of **2a**, by using 5-nitrothiophene-2-carboxaldehyde. Light yellow solid (yield 34.6%), mp 270–271 °C, ^{1}H NMR (400 MHz, DMSO-d_6): δ 12.84 (s, 1H), 9.94 (s, 1H), 8.29 (d, *J* = 3.16, 1H), 7.99 (d, *J* = 8.84, 2H), 7.83 (d, *J* = 8.84, 2H), 7.52–50 (m, 1H), 7.29–7.20 (m, 1H), 4.13–4.00 (m, 2H), 3.41–3.37 (m, 1H), 2.88–2.73 (m, 2H) ppm. ^{13}C NMR (100 MHz, DMSO-d_6): δ 197.10, 185.40, 174.49, 173.04, 143.58, 138.87, 137.51, 129.63, 124.59, 123.91, 122.57, 121.28, 118.89, 112.87, 50.26, 35.81, 35.50, 26.95 ppm. HRMS (ESI): *m/z* calcd. for $C_{18}H_{14}N_2O_6S^+$ $[M+H]^+$: 386.0567, found 386.0581.

6.7. 1-(4-(3-(1*H*-Indol-4-yl)acryloyl)phenyl)-4-carboxy-2-pyrrolidinone (2f)

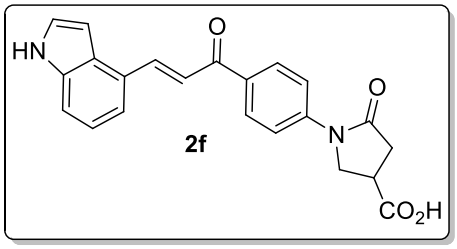

The compound **2f** was prepared by following the procedure described for the synthesis of **2a**, by using indole-4-carboxaldehyde. Dark brown solid (yield 47.0%), mp 232–233 °C, ^{1}H NMR (400 MHz, DMSO-d_6): δ 12.904 (s, 1H), 11.49 (s, 1H), 8.22 (d, *J* = 8.8 Hz, 2H), 8.14 (d, *J* = 15.6 Hz, 1H), 7.98 (d, *J* = 15.5 Hz, 1H), 7.90 (d, *J*= 8.8 Hz, 2H), 7.67 (d, *J* =

doi:10.6342/NTU202400256

7.4 Hz, 1H), 7.56 (t, J = 4.2 Hz, 2H), 7.22 (t, J = 7.7 Hz, 1H), 6.89 (s, 1H), 4.18–4.05 (m, 2H), 3.44–3.39 (m, 1H), 2.90–2.75 (m, 2H) ppm. ^{13}C NMR (100 MHz, DMSO-d_6): δ 188.21, 174.56, 173.11, 143.52, 143.25, 136.93, 133.56, 129.92, 127.71, 127.60, 127.36, 121.54, 121.51, 121.12, 119.10, 114.77, 100.39, 50.34, 35.88, 35.58. HRMS (ESI): *m/z* calcd. for $C_{22}H_{19}N_2O_4^+$ $[M+H]^+$: 375.1339, found 375.1326.

6.8. 1-(4-(3-(1*H*-Indol-3-yl)acryloyl)phenyl)-4-carboxy-2-pyrrolidinone (2g)

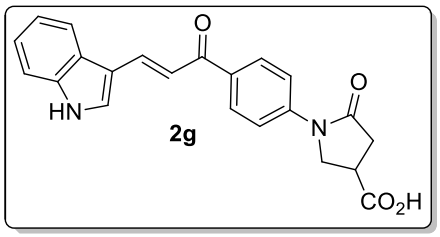

The compound **2g** was prepared by following the procedure described for the synthesis of **2a**, by using indole-3-carboxaldehyde. Dark yellow solid (yield 52.2%), mp 230–231 °C, ^{1}H NMR (400 MHz, DMSO-d_6): δ 12.849 (s, 1H), 11.45 (s, 1H), 8.22–8.09 (m, 2H), 7.99–7.97 (m, 2H), 7.90 (d, J = 8.88 Hz, 1H), 7.83 (d, J = 8.84 Hz, 1H), 7.67 (d, J = 7.74 Hz, 1H) 7.56–7.54 (m, 1H), 7.22 (t, J = 15.44 Hz, 1H) 6.89 (s, 1H), 6.64 (d, J = 8.8 Hz, 1H), 4.18–4.10 (m, 2H), 3.44–3.37 m, 1H), 2.89–2.72 (m, 2H) ppm. ^{13}C NMR (100 MHz, DMSO-d_6): δ 174.55, 173.12, 167.32, 143.62, 143.33, 130.61, 129.93, 121.57, 121.48, 121.01, 119.91, 114.80, 100.40, 100.10, 50.31, 35.80, 35.52. HRMS (ESI): *m/z* calcd. for $C_{22}H_{18}N_2O_4^-$ $[M+H]^-$: 374.1261, found 374.1238.

6.9. 1-(4-Acetylphenyl)-2-pyrrolidinone (3)

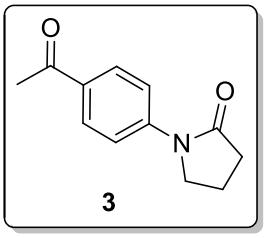

doi:10.6342/NTU202400256

The compound **3** was synthesized following a procedure reported for copper/*N*,*N*-dimethylglycine catalyzed Goldberg reaction (Jiang, 2014). A Schlenk tube was charged with amide (1.2 mmol), aryl halide (1 mmol), CuI (0.05 or 0.1 mmol), *N*,*N*-dimethylglycine (0.1 or 0.2 mmol), and potassium carbonate (2 mmol). The tube was evacuated and backfilled with argon at room temperature. DMF (0.5 mL) was added under argon *via* syringe. The Schlenk tube was immersed in a preheated oil bath and the reaction mixture was stirred for the specified time at the indicated temperature. The cooled mixture was partitioned between water and ethyl acetate (3×10 mL). The organic layer was separated and the aqueous layer was extracted with ethyl acetate. The combined organic layer was washed with brine, dried over anhydrous Na_2SO_4, and concentrated *in vacuo*. The residue was purified by column chromatography on silica gel (eluting with 1:8 to 1:2 ethyl acetate/petroleum ether) to give the product **3**, a non-carboxylate analogue of **1**. Brown solid (yield 52.3%), mp 172−173 ºC, ^{1}H NMR (400 MHz, DMSO-d_6): δ 7.99 (d, *J* = 8.8 Hz, 2H), 7.83 (d, *J* = 8.8 Hz, 2H), 3.90 (t, *J* = 7.0 Hz, 2H), 3.34 (d, *J* = 1.5 Hz, 2H), 2.55 (s, 3H), 2.12–2.05 (m, 2H) ppm, ^{13}C NMR (100 MHz, DMSO-d_6) δ 197.1, 175.1, 144.1, 132.4, 129.6, 118.8, 48.4, 32.9, 27.0, 17.8 ppm. HRMS (ESI): *m/z* calcd. for $C_{12}H_{14}NO_2^+$ $[M+H]^+$: 204.1025, found 204.1021.

6.10. 1-(4-Styrylcarbonylphenyl)-2-pyrrolidinone (4a)

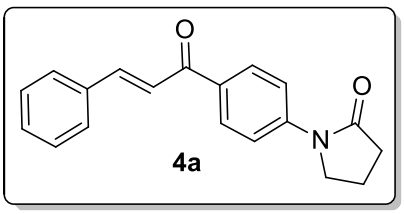

A mixture of 1-(4-acetylphenyl)-2-pyrrolidinone **3** (2.47 g, 10 mmol), benzaldehyde (1.6 g, 15 mmol), and 15 mL of 10% NaOH in 10 mL of ethanol was refluxed for 4 h and then

doi:10.6342/NTU202400256

cooled to room temperature. Then, 15 mL of water was added and the mixture was acidified to pH 1–2 with aq. HCl. The precipitate was filtered and then washed with water. The residue was purified by column chromatography on silica gel (eluting with 2:8 hexane/ethyl acetate) to give the desired product. Yellow solid (yield 63.7%), mp 280–281 °C, ^{1}H NMR (400 MHz, DMSO-d_6): δ 7.98 (d, *J* = 8.84 Hz, 2H), 7.90–7.83 (m, 3H), 7.64 (d, *J* = 15.56 Hz, 1H), 7.47–7.42 (m, 2H), 6.78 (t, *J* = 10.76 Hz, 1H), 6.66 (d, *J* = 8.92 Hz, 2H), 3.17−3.12 (m, 2H), 2.36 (t, *J* = 14.48 Hz, 2H), 1.83–1.75 (m, 2H) ppm. ^{13}C NMR (100 MHz, DMSO-d_6): δ 186.31, 174.75, 153.60, 141.84, 135.66, 131.51, 129.31, 128.97, 125.70, 122.93, 111.40, 42.03, 31.57, 24.42 ppm. HRMS (ESI): *m/z* calcd. for $C_{19}H_{18}NO_2^+$ $[M+H]^+$: 292.1332, found 292.1346.

6.11. 1-(4-(3-(1*H*-Indol-4-yl)acryloyl)phenyl)-2-pyrrolidinone (4b)

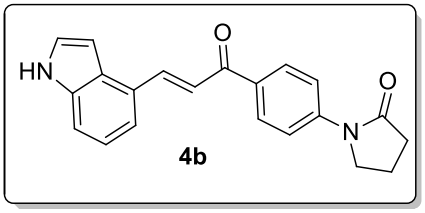

The compound **4b** was prepared by following the procedure described for the synthesis of **4a**, by using indole-4-carboxaldehyde. Dark yellow solid (yield 62.8%), mp 228–231 °C, ^{1}H NMR (400 MHz, DMSO-d_6): δ 11.460 (s, 1H), 8.22–8.09 (m, 3H), 7.98–7.88 (m, 3H), 7.67 (d, *J* = 7.6 Hz 1H), 7.556 (t, *J* = 7.5 Hz 2H), 7.22 (t, *J* = 7.2 Hz 1H), 6.88 (s, 1H), 4.17−4.04 (m, 2H), 3.44–3.39 (m, 2H), 2.89–2. 74 (m, 2H) ppm.^{13}C NMR (100 MHz, DMSO-d_6): δ 193.84, 188.44, 174.64, 173. 23, 143.40, 136.90, 133.57, 129.93, 127.75, 127.57, 126.26, 121.64, 121.42, 121.17, 199.22, 144.87, 122.66, 100.39, 50.37, 35.84, 35.53 ppm. HRMS (ESI): *m/z* calcd. for $C_{19}H_{18}NO_2^+$ $[M+H]^+$: 330.1368, found 330.1394.

doi:10.6342/NTU202400256

7. References

1. Alaaeldin, R., Mustafa, M., Abuo-Rahma, G.E.-D.A., Fathy, M., 2022. In vitro inhibition and molecular docking of a new ciprofloxacin-chalcone against SARS-CoV-2 main protease. Fundam Clin. Pharmacol. 36, 160–170. doi: 10.1111/fcp.12708.
2. Bestle, D., Heindl, M.R., Limburg, H., Van Lam van, T., Pilgram, O., Moulton, H., Stein, D.A., Hardes, K., Eickmann, M., Dolnik, O., Rohde, C., Klenk, H.D., Garten, W., Steinmetzer, T., Böttcher-Friebertshäuser, E., 2020. TMPRSS2 and furin are both essential for proteolytic activation of SARS-CoV-2 in human airway cells. Life Sci. Alliance 3, e202000786. doi: 10.26508/lsa.202000786.
3. Bojadzic, D., Alcazar, O., Chen, J., Chuang, S.T., Condor Capcha, J.M., Shehadeh, L.A., Buchwald, P., 2021. Small-molecule inhibitors of the coronavirus Spike: ACE2 protein-protein interaction as blockers of viral attachment and entry for SARS-CoV-2. ACS Infect. Dis. 7, 1519–1534. doi: 10.1021/acsinfecdis.1c00070.
4. Cao, Y., Yisimayi, A., Jian, F., Song, W., Xiao, T., Wang, L., Du, S., Wang, J., Li, Q., Chen, X., Yu, Y., Wang, P., Zhang, Z., Liu, P., An, R., Hao, X., Wang, Y., Wang, J., Feng, R., Sun, H., Zhao, L., Zhang, W., Zhao, D., Zheng, J., Yu, L,, Li, C., Zhang, N., Wang, R., Niu, X., Yang, S., Song, X., Chai, Y., Hu, Y., Shi, Y., Zheng, L., Li, Z., Gu, Q., Shao, F., Huang, W., Jin, R., Shen, Z., Wang, Y., Wang, X., Xiao, J., Xie, X.S., 2022. BA.2.12.1, BA.4 and BA.5 escape antibodies elicited by Omicron infection. Nature. 608, 593–602. doi: 10.1038/s41586-022-04980-y.
5. Cheng, Y.W., Chao, T.L., Li, C.L., Chiu, M.F., Kao, H.C., Wang, S.H., Pang, Y.H., Lin, C.H., Tsai, Y.M., Lee, W.H., Tao, M.H., Ho, T.C., Wu, P.Y., Jang, L.T., Chen,

doi:10.6342/NTU202400256

P.J., Chang, S.Y., Yeh, S.H. 2020. Furin inhibitors block SARS-CoV-2 Spike protein cleavage to suppress virus production and cytopathic effects. Cell Rep. 33, 108254. doi: 10.1016/j.celrep.2020.108254.

6. Dai, W., Zhang, B., Jiang, X.M., Su, H., Li, J., Zhao, Y., Xie, X., Jin, Z., Peng, J., Liu, F., Li, C., Li, Y., Bai, F., Wang, H., Cheng, X., Cen, X., Hu, S., Yang, X., Wang, J., Liu, X., Xiao, G., Jiang, H., Rao, Z., Zhang, L.K., Xu, Y., Yang, H., Liu, H., 2020. Structure-based design of antiviral drug candidates targeting SARS-CoV-2 main protease. Science 368, 1331–1335. doi: 10.1126/science.abb4489.
7. de Wit, E., van Doremalen, N., Falzarano, D., Munster, V.J., 2016. SARS and MERS: recent insights into emerging coronaviruses. Nat. Rev. Microbiol. 14, 523–34. doi: 10.1038/nrmicro.2016.81.
8. Duran, N., Polat, M.F., Aktas, D.A., Alagoz, M.A., Ay, E., Cimen, F., Tek, E., Anil, B., Burmaoglu, S., Algul, O., 2021. New chalcone derivatives as effective against SARS-CoV-2 Agent. Int. J. Clin. Pract. 75, e14846. doi: 10.1111/ijcp.14846.
9. Essalmani, R., Jain, J., Susan-Resiga, D., Andréo, U., Evagelidis, A., Derbali, R.M., Huynh, D.N., Dallaire, F., Laporte, M., Delpal, A., Sutto-Ortiz, P., Coutard, B., Mapa, C., Wilcoxen, K., Decroly, E., Nq Pham, T., Cohen, É.A., Seidah, N.G. 2022. Distinctive roles of Furin and TMPRSS2 in SARS-CoV-2 infectivity. J. Virol. 96, e0012822. doi: 10.1128/jvi.00128-22.
10. Fraser, B.J., Beldar, S., Seitova, A., Hutchinson, A., Mannar, D., Li, Y., Kwon, D., Tan, R., Wilson, R.P., Leopold, K., Subramaniam, S., Halabelian, L., Arrowsmith, C.H., Bénard, F., 2022. Structure and activity of human TMPRSS2 protease implicated in SARS-CoV-2 activation. Nat. Chem. Biol. 18, 963–971. doi:

doi:10.6342/NTU202400256

10.1038/s41589-022-01059-7.

11. Ghosh, A.K., Raghavaiah, J., Shahabi, D., Yadav, M., Anson, B.J., Lendy, E.K., Hattori, S.I., Higashi-Kuwata, N., Mitsuya, H., Mesecar, A.D., 2021. Indole chloropyridinyl ester-derived SARS-CoV-2 3CLpro Inhibitors: Enzyme inhibition, antiviral Efficacy, structure-activity relationship, and X-ray structural studies. J. Med. Chem. 64, 14702–14714. doi: 10.1021/acs.jmedchem.1c01214.
12. Gobinath, P., Packialakshmi, P., Ali, D., Alarifi, S., Alotaibi, A., Idhayadhulla, A., Surendrakumar, R., 2021. Synthesis and cytotoxic activity of novel indole derivatives and their in Silico screening on Spike glycoprotein of SARS-CoV-2. Front. Mol. Biosci. 8, 637989. doi: 10.3389/fmolb.2021.637989.
13. Gordon, C.J., Tchesnokov, E.P., Woolner, E., Perry, J.K., Feng, J.Y., Porter, D.P., Götte, M., 2020. Remdesivir is a direct-acting antiviral that inhibits RNA-dependent RNA polymerase from Severe Acute Respiratory Syndrome Coronavirus 2 with high potency. J. Biol. Chem. 295, 6785–6797. doi: 10.1074/jbc.RA120.013679.
14. Grein, J., Ohmagari, N., Shin, D., Diaz, G., Asperges, E., Castagna, A., Feldt, T., Green, G., Green, M.L., Lescure, F.X., Nicastri, E., Oda, R., Yo, K., Quiros-Roldan, E., Studemeister, A., Redinski, J., Ahmed, S., Bernett, J., Chelliah, D., Chen, D., Chihara, S., Cohen, S.H., Cunningham, J., D'Arminio Monforte, A., Ismail, S., Kato, H., Lapadula, G., L'Her, E., Maeno, T., Majumder, S., Massari, M., Mora-Rillo, M., Mutoh, Y., Nguyen, D., Verweij, E., Zoufaly, A., Osinusi, A.O., DeZure, A., Zhao, Y., Zhong, L., Chokkalingam, A., Elboudwarej, E., Telep, L., Timbs, L., Henne, I., Sellers, S., Cao, H., Tan, S.K., Winterbourne, L., Desai, P., Mera, R., Gaggar, A., Myers, R.P., Brainard, D.M., Childs, R., Flanigan, T., 2020. Compassionate use of

doi:10.6342/NTU202400256

Remdesivir for patients with severe Covid-19. N. Engl. J. Med. 382, 2327–2336. doi: 10.1056/NEJMoa2007016.

15. Hattori, S.I., Higashi-Kuwata, N., Hayashi, H., Allu, S.R., Raghavaiah, J., Bulut, H., Das, D., Anson, B.J., Lendy, E.K., Takamatsu, Y., Takamune, N., Kishimoto, N., Murayama, K., Hasegawa, K., Li, M., Davis, D.A., Kodama, E.N., Yarchoan, R., Wlodawer, A., Misumi, S., Mesecar, A.D., Ghosh, A.K., Mitsuya, H., 2021. A small molecule compound with an indole moiety inhibits the main protease of SARS-CoV-2 and blocks virus replication. Nat. Commun. 12, 668. doi: 10.1038/s41467-021-20900-6
16. Hoffman, R.L., Kania, R.S., Brothers, M.A., Davies, J.F., Ferre, R.A., Gajiwala, K.S., He, M., Hogan, R.J., Kozminski, K., Li, L.Y., Lockner, J.W., Lou, J., Marra, M.T., Mitchell, L.J. Jr, Murray, B.W., Nieman, J.A., Noell, S., Planken, S.P., Rowe, T., Ryan, K., Smith, G.J. 3rd, Solowiej, J.E., Steppan, C.M., Taggart, B., 2020. Discovery of ketone-based covalent inhibitors of Coronavirus 3CL proteases for the potential therapeutic treatment of COVID-19. J. Med. Chem. 63, 12725–12747. doi: 10.1021/acs.jmedchem.0c01063.
17. Hoffmann, M., Kleine-Weber, H., Schroeder, S., Krüger, N., Herrler, T., Erichsen, S., Schiergens, T.S., Herrler, G., Wu, N.H., Nitsche, A., Müller, M.A., Drosten, C., Pöhlmann, S., 2020a. SARS-CoV-2 cell entry depends on ACE2 and TMPRSS2 and is blocked by a clinically proven protease inhibitor. Cell 181, 271–280.e8. doi: 10.1016/j.cell.2020.02.052.
18. Hoffmann, M., Schroeder, S., Kleine-Weber, H., Müller, M.A., Drosten, C., Pöhlmann, S., 2020b. Nafamostat mesylate blocks activation of SARS-CoV-2: New

doi:10.6342/NTU202400256

treatment option for COVID-19. Antimicrob. Agents Chemother. 64, e00754–20. doi: 10.1128/AAC.00754-20.

19. Hoffmann, M., Sidarovich, A., Arora, P., Krüger, N., Nehlmeier, I., Kempf, A., Graichen, L., Winkler, M.S., Niemeyer, D., Goffinet, C., Drosten, C., Schulz, S., Jäck, H.M., Pöhlmann, S. 2022. Evidence for an ACE2-independent entry pathway that can protect from neutralization by an antibody used for COVID-19 therapy. mBio. 13, e0036422. doi: 10.1128/mbio.00364-22.
20. Hsu, M.F., Kuo, C.J., Chang, K.T., Chang, H.C., Chou, C.C., Ko, T.P., Shr, H.L., Chang, G.G., Wang, A.H., Liang, P.H., 2005. Mechanism of the maturation process of SARS-CoV 3CL protease. J. Biol. Chem. 280, 31257–31266. doi: 10.1074/jbc.M502577200.
21. Huang, C., Wang, Y., Li, X., Ren, L., Zhao, J., Hu, Y., Zhang, L., Fan, G., Xu, J., Gu, X., Cheng, Z., Yu, T., Xia, J., Wei, Y., Wu, W., Xie, X., Yin, W., Li, H., Liu, M., Xiao, Y., Gao, H., Guo, L., Xie, J., Wang, G., Jiang, R., Gao, Z., Jin, Q., Wang, J., Cao, B., 2020. Clinical features of patients infected with 2019 novel coronavirus in Wuhan, China. Lancet 395, 497–506. doi: 10.1016/S0140-6736(20)30183-5.
22. Imai, M., Iwatsuki-Horimoto, K., Hatta, M., Loeber, S., Halfmann, P.J., Nakajima, N., Watanabe, T., Ujie, M., Takahashi, K., Ito, M., Yamada, S., Fan, S., Chiba, S., Kuroda, M., Guan, L., Takada, K., Armbrust, T., Balogh, A., Furusawa, Y., Okuda, M., Ueki, H., Yasuhara, A., Sakai-Tagawa, Y., Lopes, T.J.S., Kiso, M., Yamayoshi, S., Kinoshita, N., Ohmagari, N., Hattori, S.I., Takeda, M., Mitsuya, H., Krammer, F., Suzuki, T., Kawaoka, Y., 2020. Syrian hamsters as a small animal model for SARS-CoV-2 infection and countermeasure development. Proc. Natl. Acad. Sci. USA. 117,

doi:10.6342/NTU202400256

16587–16595. doi: 10.1073/pnas.2009799117.

23. Jackson, C.B., Farzan, M., Chen, B., Choe, H., 2022. Mechanisms of SARS-CoV-2 entry into cells. Nat. Rev. Mol. Cell Biol. 23, 3−20. doi: 10.1038/s41580-021-00418-x.

24. Jayaram, B., Singh, T., Mukherjee, G., Mathur, A., Shekhar, S., Shekhar, V., 2012. A freely accessible web-server for target directed lead molecule discovery. BMC bioinformatics 13, 1−13. doi: 10.1186/1471-2105-13-S17-S7.

25. Jiang, L. 2014. Copper/N,N-dimethylglycine catalyzed Goldberg reactions between aryl bromides and amides, aryl iodides and secondary acyclic amides. Molecules 19, 13448−13460. doi: 10.3390/molecules190913448.

26. Jin, Z., Du, X., Xu, Y.. Deng, Y., Liu, M., Zhao, Y., Zhang, B., Li, X., Zhang, L., Peng, C., Duan, Y., Yu, J., Wang, L., Yang, K., Liu, F., Jiang, R., Yang, X., You, T., Liu, X., Yang, X., Bai, F., Liu, H., Liu, X., Guddat, L.W., Xu, W., Xiao, G., Qin, C., Shi, Z., Jiang, H., Rao, Z., Yang, H., 2020. Structure of Mpro from COVID-19 virus and discovery of its inhibitors. Nature 582, 289−293. doi: 10.1038/s41586-020-2223-y.

27. Kim, Y., Liu, H., Galasiti Kankanamalage, A.C., Weerasekara, S., Hua, D.H., Groutas, W.C., Chang, K.O., Pedersen, N.C., 2016. Reversal of the progression of fatal coronavirus infection in cats by a broad-spectrum coronavirus protease inhibitor. PLoS Pathog. 12, e1005531. doi: 10.1371/journal.ppat.1005531.

28. Kuo, C.J., Chao, T.L., Kao, H.C., Tsai, Y.M., Liu, Y.K., Wang, L.H., Hsieh, M.C., Chang, S.Y., Liang, P.H., 2021. Kinetic characterization and inhibitor screening for the proteases leading to identification of drugs against SARS-CoV-2. Antimicrob.

doi:10.6342/NTU202400256

Agents Chemother. 65, e02577-20. doi: 10.1128/AAC.02577-20.

29. Kuo, C.J., Liang, P.H., 2015. Characterization, inhibition, and engineering of the main protease of Severe Acute Respiratory Syndrome Coronavirus. ChemBioEng Rev. 2, 118–132. doi:10.1002/cben.201400031.

30. Kuo CJ, Liang PH., 2022. SARS-CoV-2 3CLpro displays faster self-maturation in vitro than SARS-CoV 3CLpro due to faster C-terminal cleavage. FEBS Lett. 596, 1214–1224. doi: 10.1002/1873-3468.14337.

31. Lan, J., Ge, J., Yu, J., Shan, S., Zhou, H., Fan, S., Zhang, Q., Shi, X., Wang, Q., Zhang, L., Wang, X. 2020. Structure of the SARS-CoV-2 spike receptor-binding domain bound to the ACE2 receptor. Nature 581, 215–220. doi: 10.1038/s41586-020-2180-5.

32. Lee, J.Y., Kuo, C.J., Shin, J.S., Jung, E., Liang, P.H., Jung, Y.S., 2021. Identification of non-covalent 3C-like protease inhibitors against severe acute respiratory syndrome coronavirus-2 via virtual screening of a Korean compound library. Bioorg. Med. Chem. Lett. 42, 128067. doi: 10.1016/j.bmcl.2021.128067.

33. Lee, R.K., Li, T.N., Chang, S.Y., Chao, T.L., Kuo, C.H., Pan, M.Y., Chiou, Y.T., Liao, K.J., Yang, Y., Wu, Y.H., Huang, C.H., Juan, H.F., Hsieh, H.P., Wang, L.H. 2022. Identification of Entry Inhibitors against Delta and Omicron Variants of SARS-CoV-2. Int. J. Mol. Sci. 23, 4050. doi: 10.3390/ijms23074050.

34. Lipinski, C.A., 2004. Lead-and drug-like compounds: the rule-of-five revolution. Drug Discov. Today Technol. 1, 337–341. doi: 10.1016/j.ddtec.2004.11.007.

35. Lu, R., Zhao, X., Li, J., Niu, P., Yang, B., Wu, H., Wang, W., Song, H., Huang, B., Zhu, N., Bi, Y., Ma, X., Zhan, F., Wang, L., Hu, T., Zhou, H., Hu, Z., Zhou, W.,

doi:10.6342/NTU202400256

Zhao, L., Chen, J., Meng, Y., Wang, J., Lin, Y., Yuan, J., Xie, Z., Ma, J., Liu, W.J., Wang, D., Xu, W., Holmes, E.C., Gao, G.F., Wu, G., Chen, W., Shi, W., Tan, W., 2020. Genomic characterisation and epidemiology of 2019 novel coronavirus: implication for virus origins and receptor binding. Lancet 395, 565–574. doi: 10.1016/S0140-6736(20)30251-8.

36. Mahoney, M., Damalanka, V.C., Tartellm, M.A., Chung, D.H., Lourenço, A.L., Pwee, D., Bridwell, A.E.M., Hoffmann, M., Voss, J., Karmakar, P., Azouz, N.P., Klingler, A.M., Rothlauf, P.W., Thompson, C.E., Lee, M., Klampfer, L., Stallings, C.L., Rothenberg, M.E., Pöhlmann, S., Whelan, S.P..J, O'Donoghue, A.J., Craik, C.S., Janetka, J.W., 2021. A novel class of TMPRSS2 inhibitors potently block SARS-CoV-2 and MERS-CoV viral entry and protect human epithelial lung cells. Proc. Natl. Acad. Sci. USA. 118, e2108728118. doi: 10.1073/pnas.2108728118.
37. Mondal, S., Chen, Y., Lockbaum, G.J., Sen, S., Chaudhuri, S., Reyes, A.C., Lee, J.M., Kaur, A.N., Sultana, N., Cameron, M.D., Shaffer, S.A., Schiffer, C.A., Fitzgerald, K.A., Thompson, P.R., 2022. Dual inhibitors of main protease (MPro) and cathepsin L as potent antivirals against SARS-CoV2. J. Am. Chem. Soc. 144, 21035–21045. doi: 10.1021/jacs.2c04626.
38. O'Boyle, N.M., Banck, M., James, C.A., Morley, C., Vandermeersch, T., Hutchison, G.R., 2011. Open Babel: An open chemical toolbox 2011. J. Cheminform. 3, 33. doi: 10.1186/1758-2946-3-33.
39. Ouyang, Y., Li, J., Chen, X., Fu, X., Sun, S., Wu, Q., 2021. Chalcone derivatives: Role in anticancer therapy. Biomolecules 11, 894. doi: 10.3390/biom11060894.
40. Özdemir, A., Altintop, M.D., Turan-Zitouni, G., Çiftçi, G.A., Ertorun, İ., Alataş, Ö.,

doi:10.6342/NTU202400256

Kaplancikli, Z.A., 2015. Synthesis and evaluation of new indole-based chalcones as potential antiinflammatory agents. Eur. J. Med. Chem. 89, 304–309. doi: 10.1016/j.ejmech.2014.10.056.

41. Pires, D.E.V., Blundell, T.L., Ascher, D.B., 2015. pkCSM: predicting small-molecule pharmacokinetic and toxicity properties using graph-based signatures. J. Med. Chem. 58, 4066–4072. doi: 10.1021/acs.jmedchem.5b00104.
42. Ramesh, D., Joji, A., Vijayakumar, B.G., Sethumadhavan, A., Mani, M., Kannan, T., 2020. Indole chalcones: design, synthesis, in vitro and in silico evaluation against Mycobacterium tuberculosis. Eur. J. Med. Chem. 198, 112358. doi: 10.1016/j.ejmech.2020.112358.
43. Sheahan, T.P., Sims, A.C., Zhou, S., Graham, R.L., Pruijssers, A.J., Agostini, M.L., Leist, S.R., Schäfer, A., Dinnon, K.H. 3rd, Stevens, L.J., Chappell, J.D., Lu, X., Hughes, T.M,, George, A.S., Hill, C.S., Montgomery, S.A., Brown, A.J., Bluemling, G.R., Natchus, M.G., Saindane, M., Kolykhalov, A.A., Painter, G., Harcourt, J., Tamin, A., Thornburg, N.J., Swanstrom, R., Denison, M.R., Baric, R.S. , 2020. An orally bioavailable broad-spectrum antiviral inhibits SARS-CoV-2 in human airway epithelial cell cultures and multiple coronaviruses in mice. Sci Transl Med. 12, eabb5883. doi: 10.1126/scitranslmed.abb5883.
44. Shapira, T., Monreal, I.A., Dion, S.P., Buchholz, D.W., Imbiakha, B., Olmstead, A.D., Jager, M., Désilets, A., Gao, G., Martins, M., Vandal, T., Thompson, C.A.H., Chin, A., Rees, W.D., Steiner, T., Nabi, I.R., Marsault, E., Sahler, J., Diel, D.G., Van de Walle, G.R, August, A., Whittaker, G.R., Boudreault, P.L., Leduc, R., Aguilar, H.C., Jean, F., 2022. A TMPRSS2 inhibitor acts as a pan-SARS-CoV-2 prophylactic

doi:10.6342/NTU202400256

and therapeutic. Nature 605, 340–348. doi: 10.1038/s41586-022-04661-w.

45. Sia, S.F., Yan, L.M., Chin, A.W.H., Fung, K., Choy, K.T., Wong, A.Y.L., Kaewpreedee, P., Perera, R.A.P.M., Poon, L.L.M., Nicholls, J.M., Peiris, M., Yen, H.L., 2020. Pathogenesis and transmission of SARS-CoV-2 in golden hamsters. Nature 583, 834–838. doi: 10.1038/s41586-020-2342-5.

46. Tang, W.F., Tsai, H.P., Chang, Y.H., Chang, T.Y., Hsieh, C.F., Lin, C.Y., Lin, G.H., Chen, Y.L., Jheng, J.R., Liu, P.C., Yang, C.M., Chin, Y.F., Chen, C.C., Kau, J.H., Hung, Y.J., Hsieh, P.S., Horng, J.T., 2021. Perilla (Perillafrutescens) leaf extract inhibits SARS CoV-2 via direct virus inactivation. Biomed. J. 44, 293–303. doi: 10.1016/j.bj.2021.01.005.

47. Vijayakumar, B.G., Ramesh, D., Joji, A., Prakasan, J.J., Kannan, T., 2020. In Silico pharmacokinetic and molecular docking studies of natural flavonoids and synthetic indole chalcones against essential proteins of SARS-CoV-2. Eur. J. Pharmacol. 886, 173448. doi: 10.1016/j.ejphar.2020.173448.

48. Voskiene, A., Mickevicius, V., Mikulskiene, G., 2007. Synthesis and structural characterization of products condensation 4-carboxy-1-(4-styrylcarbonylphenyl)-2-pyrrolidinones with hydrazines. Arkivoc 2007, 303–314. doi.org/10.3998/ark.5550190.0008.f29.

49. Vuong, W., Khan, M.B., Fischer, C., Arutyunova, E., Lamer, T., Shields, J., Saffran, H.A., McKay, R.T., van Belkum, M.J., Joyce, M.A., Young, H.S., Tyrrell, D.L., Vederas, J.C., Lemieux, M.J., 2020. Feline coronavirus drug inhibits the main protease of SARS-CoV-2 and blocks virus replication. Nat. Commun. 11, 4282. doi: 10.1038/s41467-020-18096-2.

doi:10.6342/NTU202400256

50. Wang, M., Cao, R., Zhang, L., Yang, X., Liu, J., Xu, M., Shi, Z., Hu, Z., Zhong, W., Xiao, G. 2020. Remdesivir and chloroquine effectively inhibit the recently emerged novel coronavirus (2019-nCoV) in vitro. Cell Res. 30, 269–271. doi: 10.1038/s41422-020-0282-0.

51. Wu, F., Zhao, S., Yu, B., Chen, Y.M., Wang, W., Song, Z.G., Hu, Y., Tao, Z.W., Tian, J.H., Pei, Y.Y., Yuan, M.L., Zhang, Y.L., Dai, F.H., Liu, Y., Wang, Q.M., Zheng, J.J., Xu, L., Holmes, E.C., Zhang, Y.Z., 2020. A new coronavirus associated with human respiratory disease in China. Nature 579, 265−269. doi: 10.1038/s41586-020-2008-3.

52. Xu, M., Wu, P., Shen, F., Ji, J., Rakesh, .KP., 2019. Chalcone derivatives and their antibacterial activities: Current development. Bioorg. Chem. 91, 103133. doi: 10.1016/j.bioorg.2019.103133.

53. Yamamoto, M., Kiso, M., Sakai-Tagawa, Y., Iwatsuki-Horimoto, K., Imai, M., Takeda, M., Kinoshita, N., Ohmagari, N., Gohda, J., Semba, K., Matsuda, Z., Kawaguchi, Y., Kawaoka, Y., Inoue, J.I., 2020. The anticoagulant nafamostat potently inhibits SARS-CoV-2 S protein-mediated fusion in a cell fusion assay system and viral infection in vitro in a cell-type-dependent manner. Viruses 12, 629. doi: 10.3390/v12060629.

54. Yan, J. Chen, S. Zhang, J. Hu, L. Huang, X. Li, X., 2016. Synthesis, evaluation, and mechanism study of novel Indole-Chalcone derivatives exerting effective antitumor activity through microtubule destabilization in vitro and in vivo. J. Med. Chem. 59, 5264−5283. doi: 10.1021/acs.jmedchem.6b00021.

55. Zhang, L., Lin, D., Sun, X., Curth, U., Drosten, C., Sauerhering, L., Becker, S., Rox,

doi:10.6342/NTU202400256

K., Hilgenfeld, R., 2020. X-ray structure of main protease of the novel coronavirus SARS-CoV-2 enables design of α-ketoamide inhibitors. Science 368, 409–412. doi: 10.1126/science.abb3405.

56. Zhou, P., Yang, X.L., Wang, X.G., Hu, B., Zhang, L., Zhang, W., Si, H.R., Zhu, Y., Li, B., Huang, C.L., Chen, H.D., Chen, J., Luo, Y., Guo, H., Jiang, R.D., Liu, M.Q., Chen, Y., Shen, X.R., Wang, X., Zheng, X.S., Zhao, K., Chen, Q.J., Deng, F., Liu, L.L., Yan, B., Zhan, F.X., Wang, Y.Y., Xiao, G.F., Shi, Z.L., 2020. A pneumonia outbreak associated with a new coronavirus of probable bat origin. Nature 579, 270–273. doi: 10.1038/s41586-020-2012-7.

57. Zhu, N., Zhang, D., Wang, W., Li, X., Yang, B., Song, J., Zhao, X., Huang, B., Shi, W., Lu, R., Niu, P., Zhan, F., Ma, X., Wang, D., Xu, W., Wu, G., Gao, G.F., Tan, W., China Novel Coronavirus Investigating and Research Team., 2020. A novel coronavirus from patients with pneumonia in China, 2019. N. Eng. J. Med. 382, 727–733. doi: 10.1056/NEJMoa2001017.

doi:10.6342/NTU202400256

Part II

Design, Synthesis, and Evaluation of 1-(4-(arylethylenylcarbonyl)phenyl)-4-carboxy-2-pyrrolidinones as Potent Inhibitors against Methicillin-Resistant *Staphylococcus aureus*

摘要

十一異戊烯基二磷酸合成酶 **(UPPS)** 是一種細菌順式異戊二烯基轉移酶，對於製造脂質載體介導肽聚醣生物合成至關重要。 我們設計了一類**1-(4-(**苯乙烯基羰基**)**苯基**)-4-**羧基**-2-**吡咯烷酮作為潛在的含有查耳酮的**UPPS**抑制劑，並透過邁克爾加成、環化、羥醛縮合和去質子化合成它們。 這些化合物針對兩種革蘭氏陽性菌－甲氧西林敏感金黃色葡萄球菌（**MSSA**）和抗甲氧西林金黃色葡萄球菌**MRSA**，以及兩種革蘭氏陰性菌－大腸桿菌和綠膿桿菌胞菌進行了評估。 苯環上帶有 **4-**氯取代基的最有效的抗菌化合物表現出廣譜抗菌活性，對 **MRSA** 的 **MIC** 為 **4.3 μg/mL**。 該化合物也抑制金黃色葡萄球菌 **UPPS**，IC_{50} 為 **5.30 μM**。 因此，我們為針對 **MRSA** 的進一步臨床前研究提供了一種有前景的先導化合物。

doi:10.6342/NTU202400256

Abstract

Undecaprenyl diphosphate synthase (UPPS) is a bacterial cis-prenyltransferase essential for making lipid carrier to mediate peptidoglycan biosynthesis. We designed a class of 1-(4-(styrylcarbonyl)phenyl)-4-carboxy-2-pyrrolidinones as potential UPPS inhibitors containing chalcone moiety and synthesized them via Michael addition, cyclization, aldol condensation, and deprotonation. The compounds were evaluated against two Gram-positive bacteria, methicillin-sensitive *Staphylococcus aureus* (MSSA) and methicillin-resistant *Staphylococcus aureus* MRSA, as well as two Gram-negative bacteria, *E. coli* and *P. aeruginosa*. The most potent antibacterial compound with 4-chloro substituent on the benzene ring displayed broad spectrum antibacterial activities with a MIC of 4.3 μg/mL against MRSA. This compound also inhibited *S. aureus* UPPS with an IC_{50} of 5.30 μM. We thus provide a promising lead compound for further preclinical study against MRSA.

doi:10.6342/NTU202400256

1. Introduction

Increased mortality and morbidity from the failure of treatment for infectious diseases caused by drug-resistant bacterial strains have been occurring. (1,2) The lack of new effective antibiotics resulted in many deaths by these drug-resistant bacteria every year, causing public health concerns. (3). The leading multidrug-resistant bacteria include methicillin-resistant *Staphylococcus aureus* (MRSA), penicillin-resistant *Streptococcus pneumoniae* (PRSP), vancomycin-resistant *Enterococci* (VRE), etc. Although tremendous efforts have been made, no new major class of antibiotics were invented between 1962 and 2000. (4) Since 2017, 12 new antibacterial drugs have been approved globally, but only vaborbactam belongs to a new antibacterial class. (5) Therefore, the development of effective antibiotics against drug-resistant bacteria is an urgent need. Particular attention has focused on MRSA because many strains of this organism are now resistant against clinically useful antibiotics like methicillin and vancomycin. (6) MRSA is an opportunistic pathogen frequently found in nosocomial infections that may lead to severe infections, including septicemias. In 2017, WHO listed MRSA as one of the high priority pathogens among the most important bacterial infectious threats to human health. (7)

Chalcones are open-chain flavonoids with α,β-unsaturated carbonyl group (see the basic structure shown in Figure 1A) abundant in plants. The synthetic derivatives have attracted great interest for possible therapeutic uses. (8) Thousands of chalcone derivatives have been synthesized in chemical laboratories with a variety of different activities. (9) Chalcones containing several functional groups showed a wide spectrum of biological activities such as antimicrobial, (10–13) anti-malarial, (14,15) anticancer, (16,17) anti-inflammatory, (18,19) antiprotozoal, (20) anti-HIV, (21) antioxidant, (22) and antiulcer

doi:10.6342/NTU202400256

(23) activities. Chalcones and their derivatives have also been found to display antioxidant, (24) antimicrobial, (25) anticancer, (26) anti-malarial, (27) anti-inflammatory, (28) antiulcer, (29) anti-leishmanial, (30) and anti-HIV (31) properties. For some examples of antibacterial chalcones (only those inhibiting MRSA are shown in Figure 1 as examples), the compound in Figure 1B displayed good bactericidal inhibitory activities against both Gram-positive and Gram-negative bacteria, including the drug-resistant species MRSA (MIC = 0.25 μg/mL), *Klebsiella pneumoniae Carbapenemase* (KPC) and New Delhi metallo-lactamase-1 (NDM-1). (32) The potential compounds can depolarize and permeabilize bacterial membranes, leading to the rapid death of bacteria. Triazolyl chalcones were synthesized and evaluated against a panel of bacterial strain and the most active compound (Figure 1C) displayed inhibitory activities against MRSA (MIC: 4 μg/mL), *M. luteus* (MIC: 4 μg/mL) and *C. mycoderma* (MIC: 8 μg/mL) comparable or better than the control drugs (Chloromycin and Norfloxacin). (33) The possible antimicrobial action mechanism of the synthesized compounds could be binding with DNA. Compound shown in Figure 1D, a chalcone derivative bearing 2,4-thiazolidinedione and benzoic acid moieties with a MIC of 1 and 0.5 μg/mL against MRSA CCARM 3167 and 3506, respectively, showed eight-fold more potency than Norfloxacin (MIC: 8 and 4 μg/mL) and 64-fold more activity than Oxacillin (MIC > 64 μg/mL) without knowing the antimicrobial mechanism. (34) A class of chalcones having “cationic” aliphatic amino substituents were investigated and the compound shown in Figure 1E displayed MIC values of 2 μM against MRSA and also active against *E. faecium* and *E. coli* with MIC of 5 μM. (35) The compounds acted by unselective disruption of bacterial cell membranes.

doi:10.6342/NTU202400256

Undecaprenyl diphosphate synthase (UPPS) is essential for bacterial survival by synthesizing C55 product via 8 condensation reactions of homoallylic C5 isopentenyl diphosphate (IPP) with an allylic C15 farnesyl diphosphate (FPP), as a lipid carrier to mediate biosynthesis of peptidoglycan. (36) Therefore, it is regarded as a validated target for developing new antibiotics and several UPPS inhibitors have been reported to inhibit bacterial growth. (e.g. 37–42) None of them contain chalcone moiety. As reported herein, we designed and synthesized a series of 1-(4-(arylethylenylcarbonyl)phenyl)-4-carboxy-2-pyrrolidinones containing the chalcone moiety as UPPS inhibitors. They were evaluated against two Gram-positive bacteria, methicillin-sensitive *Staphylococcus aureus* (MSSA) and MRSA, as well as two Gram-negative bacteria, *E. coli* and *P. aeruginosa*. We found the electron-withdrawing groups at the para and meta positions of the benzene ring increased the antibacterial activities. The best inhibitor displayed a MIC of 4.3 μg/mL against MRSA and an IC_{50} of 5.30 μM SaUPPS. We thus provide a new promising antibacterial lead with a chalcone against MRSA by inhibiting UPPS or other targets.

doi:10.6342/NTU202400256

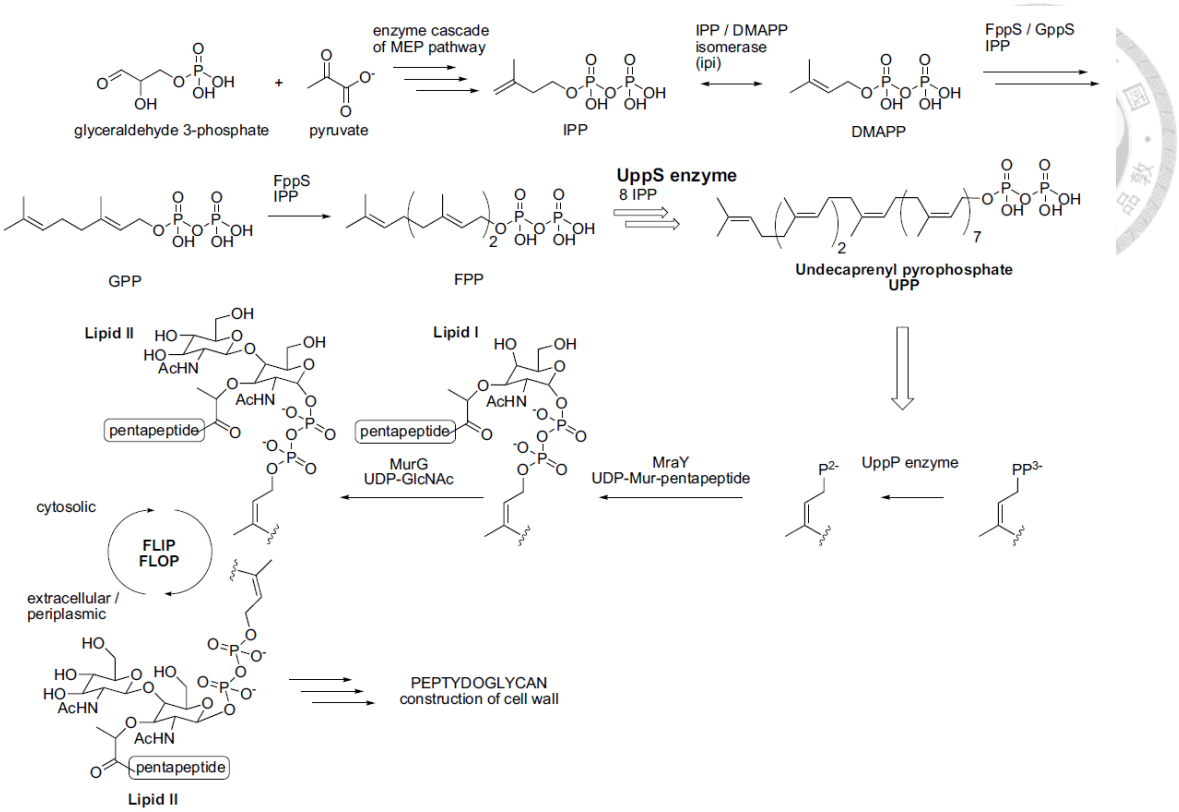

The pathway of peptidoglycan synthesis

2. Materials and methods

Reactions for synthesizing compounds were monitored by using thin-layer chromatography (TLC) on silica gel. Flash chromatography was performed on silica gel of 60–200 μm particle size for compound purification. Yields are reported for spectroscopically pure compounds. Melting points were recorded on the Fargo MP-1D Melting Point Apparatus. NMR spectra were recorded on Bruker AVIIIHD 400MHz FT-NMR in the Department of Chemistry, National Taiwan University. Chemical shifts are given in δ values relative to tetramethylsilane (TMS); coupling constants *J* are given in Hz. Internal standards were $CDCl_3$ (δ_H = 7.24) or DMSO-d_6 (δ_H = 2.49) for ^{1}H-NMR spectra, and $CDCl_3$ (δ_C = 77.0) or DMSO-d_6 (δ_C = 39.5) for ^{13}C-NMR spectra. The splitting patterns

doi:10.6342/NTU202400256

are reported as s (singlet), d (doublet), t (triplet), q (quartet), m (multiplet), br (broad) and dd (double of doublets). High-resolution mass spectra were measured by Bruker UPLC-MS in the TechComm core facility, Department of Chemistry, National Taiwan University.

2.1. Chemicals

All the reagents were the highest commercially available grade and were used without further purification. 4-aminoacetophenone, itaconic acid, 4-fluorobenzaldehyde, 4-chlorobenzaldehyde, 4-bromobenzaldehyde, 4-hydroxybenzaldehyde, 4-carboxybenzaldehyde, 4-cyanobenzaldehyde, 4-hydroxy-2-fluorobenzaldehyde, 2,4-difluorobenzaldehyde, and 4-chloro-2-fluorobenzaldehyde, were purchased from AK Scientific (Union City, USA). Benzaldehyde was purchased from Acros Organics (New Jersey, USA). Compound **2a** and its analogue without the carboxylate on the pyrrolidinone ring had been synthesized in our previous studies. (48) Compounds **2b**–**2j** are new compounds synthesized in this study.

2.2. Test of the Synthesized Compounds on Inhibiting Bacteria

For testing antibacterial activities of the synthesized compounds, the strain of Methicillin-sensitive *Staphylococcus aureus* (MSSA) ATCC 29213, the strain of MRSA ATCC 33592, the strain of *E. coli* K12/BW25113, and the strain of *P. aeruginosa* PAO1 were used. The diameters of bacterial inhibition zones in mm were represented with numbers of positive sign +, + 5.1–7 mm, ++ 7.1–9 mm, +++ 9.1–11 mm (including the 5 mm of the paper disk). The absence of inhibition was denoted by a negative sign –, indicating no clear zone of inhibition. Those marked +/-, signifying a vague inhibition zone, were categorized as minor positive (< 5.1 mm). DMSO was used as a negative control

doi:10.6342/NTU202400256

and the following conditions were used as positive controls, vancomycin 2 μg/disc for MSSA and MRSA, carbenicillin 3 μg/disc for *E. coli*, and 40 μg/disc for *P. aeruginosa*.

2.3. MIC Measurements

The most promising inhibitors including **2b** (**219**), **2c** (**101**), **2d** (**91**), **2h (118), 2i (452),** and **2j** (**456**), which inhibited MRSA, were further measured for MIC values. The MIC values were determined by the modified broth microdilution-colorimetric method. (49) Briefly, the test compounds were dissolved in DMSO, which was less than 8% in all the final test mixtures, and the compound concentration range of 256–0.5 mg/ml were added. The single colony of each strain was inoculated into Mueller-Hinton broth (BD/BBL, USA) to reach an inoculum level of 5 x 10^5 CFU/ml. After the plates were incubated at 37 ºC and vortexed 180 rpm for 24 h, 10% 3-(4,5-dimethylthiazol-2-yl)-2,5-diphenyltetrazolium bromide (MTT), 5 mg/mL in 0.2 mol/L, pH 7.2 phosphate-buffered saline, was added into each well, and the plates were incubated for another 15 min. The bacterium that could convert MTT from yellow to purple color was quantitated by measuring the absorbance of each culture at 550 nm using an enzyme-linked immunosorbent assay (ELISA) reader (BMG LABTECH CLARIOstar). The concentration-dependent bacterial inhibition curves were fitted with the equation A(I) = A(0) x {1-[I/(I + MIC)]} using GraphPad Prism software (v. 8.0.2). In this equation, A(I) is the bacterial quantity with inhibitor concentration I, A(0) is the bacterial quantity without inhibitor, and I is the inhibitor concentration. For each inhibitor, the measurements were repeated three times to yield an averaged MIC and a standard deviation.

doi:10.6342/NTU202400256

2.4. CC_{50} measurements.

Cytotoxicity of the compounds was determined by using the CellCount™ Cell counting Kit-8 purchased from Topcells (Energenesis Biomedical Co., Ltd., Taiwan) based on the manufacturer's instructions. Briefly, HEK293T cells were seeded onto a 96-well culture plate at a concentration of 4×10^4 cells in 200 µl medium per well. The next day, the medium was removed and wells were added with different concentrations (0, 100, 125, 250, 500, and 1000 µM) of compounds, respectively, and incubated for 24 h. Subsequently, 10 µl of CCK-8 solution was added and incubate at 37°C for 1 h. The highly water-soluble tetrazolium salt WST-8 [2-(2-methoxy-4-nitrophenyl)-3-(4-nitrophenyl)-5-(2,4-disulfophenyl)-2Htetrazolium,monosodium salt] in the solution was reduced by dehydrogenases of live cells to give a yellow colored product (formazan), absorbing light at 450 nm. The absorbance was determined by ELISA reader (VERSAmax, Molecular Devices, Sunnyvale, CA). The cell survival percentages % =(At/As)×100%, where At and As refer to the absorbance of a tested substance and solvent control, respectively. The 50% cytotoxicity concentration (CC_{50}) was defined as the concentration reducing 50% of cell viability. For each data point, the measurements were repeated three times to yield the averaged number and the standard deviation.

2.5. Cloning, Expression, and Purification of SaUPPS

The gene encoding the full-length of SaUPPS was synthesized by Bio Basic Inc. (Canada). The forward primer 5'-GGTATTGAGGGTCGCGAATTCGAGAACCTGTACTTCCAGGG-3' (froward) and the backward primer 5'-

doi:10.6342/NTU202400256

AGAGGAGAGTTAGAGCCCTCGAGTTATTCCTCGCTCAGGCC-3' for PCR reactions to amplify the gene, and the gene was subcloned into pET32Xa/LIC vector for expressing the recombinant protein with N-terminal Thioredoxin (TRX), hexa-His tag, and TEV protease cutting site. The *E. coli* BL21 competent cells transformed with the TRX-His_6-TEVp-SaUPPS construct were plated on LB-agar under 100 mg/L ampicillin selection. A single colony was selected and inoculated into 20 mL of Luria-Bertani (LB) medium with constant shaking at 200–250 rpm overnight. The culture was used to inoculate 1 liter of LB medium containing 100 mg/L ampicillin with constant shaking at 200–250 rpm at 37°C until the cell density reached OD_{600} of 0.6–0.8, followed by adding 0.5 mM isopropyl β-d-1-thiogalactopyranoside (IPTG) with constant shaking at 180 rpm at 16°C for 16–20 h to induce the protein expression. The cells were harvested by centrifugation (6500 rpm for 20 min), resuspended in buffer A (10 mM Tris-HCl, pH 7.5, 500 mM NaCl, and 2 mM 2-mercaptoethanol), and disrupted by a French-press instrument (Constant Cell Disruption System) at 20,000 psi. Cell lysate was centrifuged at 16000 rpm for 30 min at 4°C to remove debris, and the supernatant was loaded onto an open column with 5 mL nickel nitrilotriacetic acid (Ni-NTA) resin (Merck, Darmstadt, Germany). After washing with 100 mL of buffer A with 25 mM imidazole, the target protein was eluted with 25 mL of buffer A containg 250 mM imidazole, followed by dialysis against 5 L buffer A to remove imidazole, and the TRX-His_6-tag was cleaved by TEV protease at 4°C overnight. The overnight mixture was subsequently applied into another open column containing 5 mL Ni-NTA resin, and the untagged SaUPPS was eluted in the buffer A without imidazole.

doi:10.6342/NTU202400256

2.6. Inhibition Assay against SaUPPS

The dose-dependent inhibition against SaUPPS was assayed using EnzChek Pyrophosphate assay kit (Thermofisher, MA, USA). The SaUPPS enzymatic activities were assayed in buffer containing 100 mM Hepes, pH 7.5, 50 mM KCl, 1 mM $MgCl_2$, 0.1% Triton X-100, 0.2 mM 2-amino-6-mercapto-7-methylpurine ribonucleoside, 1 U/mL purine ribonucleoside phosphorylase, 0.03 U/mL inorganic pyrophosphatase, 0.037 μM of purified SaUPPS, 0.5 μM FPP, 10 μM IPP, and various concentrations of inhibitors at 25 °C. IC_{50} value was determined by fitting the concentration-dependent SaUPPS inhibition curves with the equation $A(I) = A(0) \times \{1-[I/(I + IC_{50})]\}$ using GraphPad Prism software (v.9.4.0). In this equation, A(I) represents the enzyme activity with inhibitor concentration I, I is the concentration of the inhibitor, and A(0) is the enzyme activity in the absence of the inhibitor. All measurements were performed in triplicate to generate an averaged IC_{50} and a standard deviation for each inhibitor.

2.7. Molecular docking

To predict the binding interaction between compound **2c (101)** and SaUPPS, molecular docking was carried out using iGEMDOCK software. The three-dimensional (3D) structure of SaUPPS (4H8E) was obtained from the RCSB Protein Data Bank (PDB, https://www.rcsb.org/). Prior to docking, water molecules and bound ligands were removed from the structure. The binding cavity of SaUPPS was defined by selecting residues within an 8 Å radius around the FPP binding site. This binding site was prepared by specifying residue atom types and assigning charges using the iGEMDOCK method. The 3D structure of compound 2c was generated using the Molview website (https://molview.org/), and its

doi:10.6342/NTU202400256

structural information was converted into mol2 format using the Open Babel GUI software.

For the molecular docking process, specific docking accuracy settings were selected, with GA parameters including a population size of 800, 80 generations, and 10 solutions. iGEMDOCK software was utilized to generate protein-ligand interaction profiles, encompassing Electrostatic (E), Hydrogen-Bonding (H), and Van der Waals interaction (V). After completing the docking, iGEMDOCK was employed to analyze and rank all docked poses based on the estimated binding energy. The scores of the docked poses were determined as the total energy of Electrostatic (E) + Hydrogen-Bonding (H) + Van der Waals (V) interactions within the docking site. The docked pose with the lowest energy was considered the best binding pose for compound 2c against SaUPPS.

2.8. Drug Likeness Analysis

The 3D structure of the most selective inhibitor **2c (101)** was converted into a SMILES format by Open Babel GUI software. (44) To assess the drug likeness of compound **2c (101)**, the online tool (http://www.scfbio-iitd.res.in/software/drugdesign/lipinski.jsp) was used for Lipinski rule of five estimation. (45,46) The ADMET profile of **2c (101)** was estimated by pkcsm website (http://biosig.unimelb.edu.au/pkcsm/). (47)

3. Results and discussion

3.1. Synthesis of 1-(4-(arylethylenylcarbonyl)phenyl)-4-carboxy-2-pyrrolidinones 2a-j

The preliminary product 1-(4-acetylphenyl)-4-carboxy-2-pyrrolidinone **1** was synthesized by heating of 4-aminoacetophenone with itaconic acid without any solvent

doi:10.6342/NTU202400256

(Scheme 1). Then by following a similar procedure, (43) the compounds **2a-j** were obtained in good yields by base (NaOH)-catalyzed aldol condensation of **1** and the unsubstituted or substituted benzaldehydes in ethanol. The chemical structures of synthesized compounds were confirmed by NMR and MS spectral data. The NMR assignment was made on the substituents additivity rules, spectral characteristics of structurally related compounds, signal intensities, and multiplicities. ^{13}C NMR spectra were used to prove the interpretation of the carbon resonances in some cases.

3.2. Evaluation of the Synthesized Compounds against Bacteria Bacteria (by YC Lien in Dr. SH Wu's laboratory)

We tested the inhibition of bacterial zones to evaluate the antibacterial effectiveness of the synthesized compounds as shown in Figure 2. The data are summarized in Table 1. The diameters (mm) of inhibition zones are represented as follows: – for 0 mm, + for 6–8 mm, and ++ for 8.1–10 mm. As compared to **2a (100)** without any substituent on the benzene ring, **2b (219)** and **2c (101)** with electron-withdrawing F and Cl showed better MRSA inhibition (++ at 50 and + at 25 μM), respectively. Although F has a stronger electronegativity, Cl has a larger size for binding. The even bigger Br did not display inhibition on MRSA, but a weak inhibition on MSSA (+ at 40 μM). The para-substituents such as OH **2e** (**400**), COOH **2f (221),** and CN **2g (182)** gave no inhibition on MRSA and other bacteria tested. However, when a F was added to ortho-position of **2e (400)**, compound **2h (118)** gained anti-MRSA (+ at both 50 and 25 μM) and anti-MSSA (+ at 40 μM) activities. Therefore, we added 2-F to compounds **2b (219)** and **2c (101)**, hoping to increase their anti-MRSA activity. However, 2,4-difluoro containing compound (**2i**) showed a slightly weaker anti-MRSA activity as compared to that of the 4-fluoro

doi:10.6342/NTU202400256

containing compound (**2b**). On the other hand, adding 2-fluoro into **2c** with 4-chloro group maintained the anti-MRSA activity, but slightly weaker anti-MSSA activity. Moreover, **2c (101)** at 40 μM also inhibited *E. coli* (++) and *P. aeruginosa* (+). **2j (456)** at 40 μM only inhibited *E. coli* (+) but not *P. aeruginosa*. Overall, **2b (219)** with 2-fluoro on the benzene ring was the only selective inhibitor of MRSA, whereas **2c (101)** with 2-fluoro on the benzene ring was a broad-spectrum inhibitor against all the tested bacteria.

3.3. MIC Measurements of the Active Compounds (by YC Lien in Dr. SH Wu's laboratory)

Since compounds **2b (219)**, **2c (101)**, **2d (91)**, **2h (118)**, **2i (452)**, and **2j (456)** showed better antibacterial activities as mentioned above, their MIC were accurately measured and summarized in Table 2. **2b (219)** with 4-F substituent showed relatively poor MIC of 68.1 (Figure 3A). The most potent inhibitor **2c (101)** as shown in the above screening indeed inhibited MRSA with the smallest MIC of 4.3 μg/mL as calculated from the dose-dependent curve shown in Figure 3B, approaching that of the positive control, vancomycin. The 4-Br-subsituted compound **2d (91)** showed MIC of 10.5 μg/mL against MRSA as the second best (Figure 3C). The three 2-F substituted compounds with OH, F, and Cl at the para-position displayed MIC values of 52.1, 19.6, and 12.4 μg/mL as calculated from the plots shown in Figures 3D, E, and F, respectively, for compounds **2h (118)**, **2i (452)**, and **2j (456)**. Their MIC values against MSSA were comparable to those against MRSA as summarized in Table 2, based on the dose-dependent inhibition curves shown in Figures 3G–K. Only **2d (91)** showed better anti-MRSA activity (MIC = 10.5 μg/mL) than anti-MSSA activity (MIC = 35.4 μg/mL). In general, the compounds with stronger electron-withdrawing groups on the benzene ring showed higher anti-MRSA

doi:10.6342/NTU202400256

activities.

3.4. CC_{50} Measurements of the Active Compounds (by IC Liu in Dr. PH Liang's laboratory)

Compound **2b (219)**, **2c (101)**, **2d (91)**, **2H (118)**, **2i (452)**, and **2j (456)** showed CC_{50} values of 466.4 ± 42.4, 601.4 ± 120, 433.4 ± 40.9, >1000, 591.2 ±53.3, and 576.8 ± 47.8 uM, respectively, as judged from the profiles of cell viability percentages vs. compound concentrations (Figure 4A–F). These compounds were without toxicity at the effective concentrations used for anti-bacteria.

3.5. SaUPPS IC_{50} Measurements of the Active Compounds (by JJ Liu and SH Chen in Dr. PH Liang's laboratory)

Because we designed the compounds as SaUPPS inhibitors and found they could inhibit bacterial growth, we then measured the IC_{50} of the synthesized compounds, including the inactive and active antibacterial compounds, against SaUPPS. As shown in Figure 5A–F the dose-dependent curves of the active antibacterial compounds **2b (219)**, **2c (101)**, **2h (118)**, **2i (452)**, and **2j (456)** were fitted with the equation to yield the IC_{50} of 4.41 ± 0.39, 5.30 ± 0.46, 9.24 ± 0.98, 2.74 ± 0.23, and 4.59 ± 0.67 μM, respectively, consistent with their antibacterial activities. The IC_{50} values of the selected compounds are shown in Table 3. However, **2a (100)** which could not inhibit bacterial growth still inhibited SaUPPS with an IC_{50} of 3.55 ± 0.49 μM. It is not surprising that the in-vitro antibacterial enzyme targets' inhibitors could not inhibit bacterial growth in vivo due to the compounds' properties, such as failure to entry into bacterial cells, quick degradation etc. However, **2d (91)** that failed to inhibit SaUPPS still inhibited the bacterial growth. This

doi:10.6342/NTU202400256

suggests that other target(s) might exist to count for its antibacterial effect. Other targets likely are octaprenyl diphosphate synthase for making the side-chain of bacterial ubiquinone and other bacterial prenyltransferases, as these enzymes use the same substrates FPP and IPP. (40)

3.6. Computer Modeling of 2c (101) in SaUPPS to rationalize Structure-Activity Relationship (by JJ Liu in Dr. PH Liang's laboratory)

The binding mode of the best antibacterial compound **2c (101)** in SaUPPS active site was simulated by computer modeling. As shown in Figure 6 for the binding mode on the FPP site, the binding energy was -138.9 kcal/mol. Because the analogue of **2a (100)** without the carboxylate on the pyrrolidinone ring did not inhibit SaUPPS (data not shown), the carboxylate is important for the binding. It was simulated that the carboxylate on the pyrrolidinone ring forms electrostatic interactions with Mg ion and the side-chain N atoms of R84, which is one of the key catalytic residues of SaUPPS. Moreover, the carboxylate group forms two hydrogen bonds with the hydroxyl group of Asp33 and the main-chain N atom of Gly34. Another hydrogen bond is formed between the carbonyl group of **2c (101)** and the main-chain N atom of Met54. Besides, the pyrrolidinone ring forms hydrophobic interactions with Met32, Asn35, His50, and the 2-chlorobenzene ring forms hydrophobic interactions with Ile92, Leu95, Pro96, Phe99, and Phe148.

3.7. Drug-Likeness of 2c (101) as Judged from Lipinski Rule of Five (by JJ Liu in Dr. PH Liang's laboratory)

Lipinski rule of five was established to evaluate a compound's potential as an orally bioavailable drug candidate. The Molview website (https://molview.org/) was used to

doi:10.6342/NTU202400256

prepare the 3D structure of compound **2c (101)**, the best anti-MRSA compound, and Open Babel was used to transform the structure data into a SMILES format. (44) Using the online application (http://www.scfbio-iitd.res.in/software/drugdesign/lipinski.jsp), compound **2c**'s drug likeness was evaluated based on the Lipinski rule of five. (45,46) Compound **2c (101)** fits the criteria for the Lipinski rule of five in terms of its molecular weight (less than 500 Da), logP (less than 5), hydrogen bond acceptors (less than 10) and donors (less 5), and molar refractivity (between 40 and 130) as summarized in Table S1, suggesting that it is suitable to become a candidate for drug development.

3.8. Drug-Likeness of 2c (101) as Judged from ADMET Properties (by JJ Liu in Dr. PH Liang's laboratory)

The potential for chemicals to be exploited as therapeutic agents is evaluated by the five parameters: absorption, distribution, metabolism, excretion, and toxicity (ADMET) qualities predicted in silico. The pkcsm website (http://biosig.unimelb.edu.au/pkcsm/) (47) was used to estimate the ADMET profile of compound **2c (101)** as summarized in Table S2. Human colorectal adenocarcinoma cell line (Caco2) permeability, human intestinal absorption (HIA), skin permeability, and the likelihood of being a substrate or inhibitor of P-glycoprotein were used to represent its absorption. The skin permeability value is low, showing that compound **2c (101)** is skin permeable, whereas the Caco2 permeability and HIA scores are relatively high, indicating compound **2c (101)** might be absorbed into the human intestine. Besides, P-glycoprotein is an ATP-binding cassette transporter, which can recognize a wide range of xenobiotics and extrude them out of cells. The prediction shows that compound **2c (101)** is neither P-glycoprotein's substrate nor inhibitor, suggesting that it would not be pumped out of cells through P-glycoprotein. According to the analysis of

doi:10.6342/NTU202400256

distribution progress, compound **2c (101)** would be possible to penetrate both the blood brain barrier (BBB) and the central nervous system (CNS), and the volume of distribution at steady-state (VDss) shows that compound **2c (101)** is more likely to distribute in plasma than in tissue. In the human body, pharmaceuticals are processed by Cytochrome P450 (CYP) enzymes, and inhibitors of these CYP enzymes can drastically alter the effect of pharmaceuticals. The predicted results show that compound **2c (101)** might be a substrate of CYP3A4 (an inhibitor of CYP3A4 might be co-administrated with **2c (101)** to increase its life-time), but not be processed by other CYP enzymes. For excretion prediction, compound **2c (101)** is not expected be a renal organic cation transporter-2 (OCT2) substrate, demonstrating that there is no probable contraindication. In the toxicity estimation, compound **2c (101)** is neither a mutagenic drug nor a hERG I/II inhibitor, and it does not exhibit acute toxicity, hepatotoxicity, and skin sensitization. In the toxicity estimation, the maximum tolerated dose of compound **2c (101)** is high, and compound **2c (101)** is neither a mutagenic drug nor a hERG I/II inhibitor. Moreover, it does not exhibit skin sensitization, but it might be potential to possess liver toxicity.

4. Conclusions

We designed a series of *S. aureus* UPPS inhibitors and synthesized them as new antibiotics. Generally, the compounds with stronger electro-withdrawing groups at the para-position of the phenyl ring display better antibacterial activities. The lead compound with chloro atom shows IC_{50} of 5.3 μM against *S. aureus* UPPS and MIC of 4.3 M towards MRSA. Although this compound is slightly weaker for antibacterial activity as compared to vancomycin, this series of compounds has the advantages of easy synthesis and much cheaper prices as compared to vancomycin. Therefore, we have successfully identified a

doi:10.6342/NTU202400256

promising anti-MRSA agent to be further investigated through pre-clinical trial.

Table. 1. The Inhibition Zones of the Compounds Tested for Antibacterial Activity

		Gram-positive bacteria				Gram-negative bacteria			
		MSSA		MRSA		*E.coli*		*P. aeruginosa*	
		content of compounds (μg/disc)							
Compd	**Ar**	**40**	**20**	**50**	**25**	**40**	**20**	**40**	**20**
2a (100)[a]		–	–	–	–	–	–	–	–
2b (219)	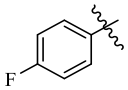	–	–	+/-	-	–	–	–	–
2c (101)	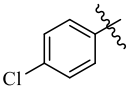	+	–	++	+	+	–	+/-	–
2d (91)	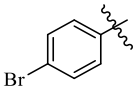	+/-	–	–	–	–	–	–	–
2e (400)	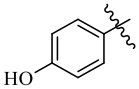	–	–	–	–	–	–	–	–
2f (221)	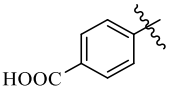	–	–	–	–	–	–	–	–
2g (182)	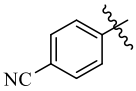	–	–	–	–	–	–	–	–
2h (118)	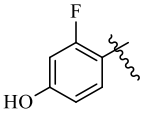	+/-	–	+/-	-	–	–	–	–
2i (452)	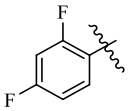	+/-	–	+/-	–	–	–	–	–
2j (456)	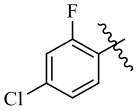	+	+/-	+	+/-	+/-	–	–	–
DMSO[b]		–	–	–	–	–	–	–	–
Vancomycin[c]		++	++	++	++	nt	nt	nt	nt
Carbenicilli[c]		nt	nt	nt	nt	+++	+++	++	++

[a]Compound synthesized previously. Others are new compounds.
[b]Negative control: DSMO
[c]Positive controls: vancomycin 2 μg/disc for MSSA and MRSA, carbenicillin 3 μg/disc for *E.coli* and 40 μg/disc for *P. aeruginosa*
nt: not tested.

doi:10.6342/NTU202400256

Table. 2. MIC Values (μg/ml) of the Effective Antibacterial Compounds

Compd	Ar	MSSA	MRSA	*E. coli*	*P. aeruginosa*
2b (219)	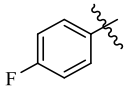	52.7	68.1	>256	>256
2c (101)	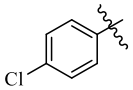	2.2	4.3	>256	>256
2d (91)	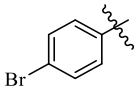	35.4	10.5	>256	>256
2h (118)	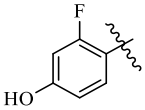	45.2	52.1	>256	>256
2i (452)	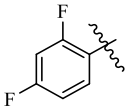	15.6	19.6	>256	>256
2j (456)	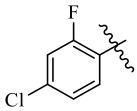	8.5	12.4	>256	>256
Vancomycin[a]		<0.5	1	nt	nt
Carbenicillin[a]		nt	nt	8	128

[a]Positive Control
nt: not tested

doi:10.6342/NTU202400256

Table. 3. IC_{50} and CC_{50} values of Some Compounds against *Sa*UPPS

Compd	Ar	*Sa*UPPS IC_{50} (μM)	CC_{50} (μM)
2a (100)		3.55 ± 0.49	nt
2b (219)	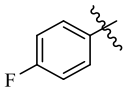	4.41 ± 0.39	466.4 ± 42.4
2c (101)	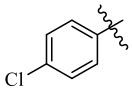	5.30 ± 0.46	601.4 ± 120
2d (91)	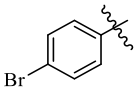	>50	433.4 ± 40.9
2h (118)	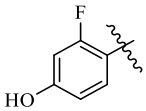	9.24 ± 0.98	>1000
2i (452)	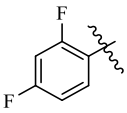	2.74 ± 0.23	591.2 ± 53.3
2j (456)	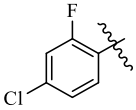	4.59 ± 0.67	576.8 ± 47.8

nt: not tested

doi:10.6342/NTU202400256

Table. 4. The Properties of 2c Analyzed Using Lipinski's Rule of Five

Properties	Predicted value
Molecular weight	368.5 Da
Hydrogen bond donors	1
Hydrogen bond acceptors	5
LogP	4.341599
Molar refractivity	99.766273

Table. 5. The ADMET Profile of Compound 2c

Properties	Predicted value
Absorption	
Water solubility (log mol/L)	-4.836
Caco2 permeability (log Papp in 10^{-6} cm/s)	1.244
Intestinal absorption (human) (% Absorbed)	98.974
Skin Permeability (log Kp)	-2.677
P-glycoprotein substrate	No
P-glycoprotein I inhibitor	No
P-glycoprotein II inhibitor	No
Distribution	
VDss (human) (log L/kg)	-0.878
Fraction unbound (human) (Fu)	0
BBB permeability (log BB)	-0.536

doi:10.6342/NTU202400256

CNS permeability (log PS)	-2.192
Metabolism	
CYP2D6 substrate	No
CYP3A4 substrate	Yes
CYP1A2 inhibitor	No
CYP2C19 inhibitor	No
CYP2C9 inhibitor	No
CYP2D6 inhibitor	No
CYP3A4 inhibitor	No
Excretion	
Total Clearance (log ml/min/kg)	-0.29
Renal OCT2 substrate	No
Toxicity	
AMES toxicity	No
Max. tolerated dose (human) (log mg/kg/day)	0.542
hERG I inhibitor	No
hERG II inhibitor	No
Oral Rat Acute Toxicity (LD_{50}) (mol/kg)	2.959
Oral Rat Chronic Toxicity (LOAEL) (log mg/kg_bw/day)	1.779
Hepatotoxicity	Yes
Skin Sensitization	No
T.Pyriformis toxicity (log ug/L)	0.354
Minnow toxicity (log mM)	-1.288

doi:10.6342/NTU202400256

Scheme 1. Synthesis of a series of compounds 2a–j and the reaction conditions in this study.

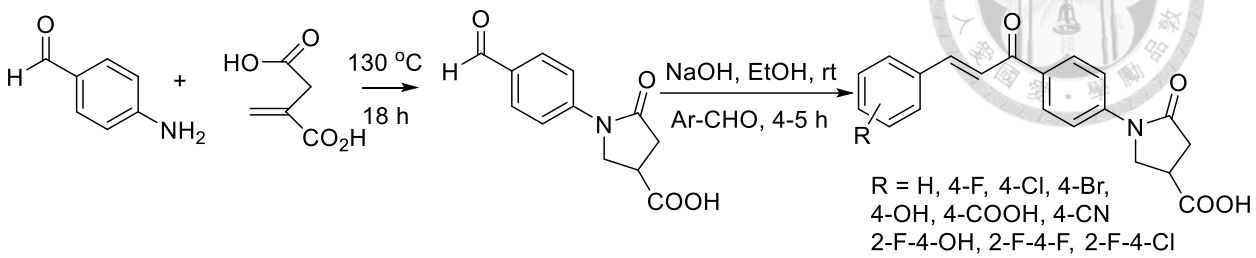

doi:10.6342/NTU202400256

5. Figure Legends

Figure. 1

A

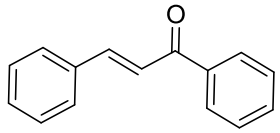

Chalcone

B

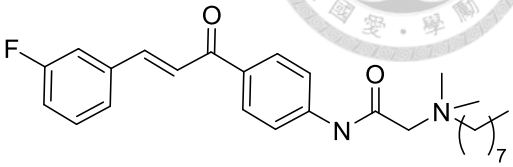

(MIC = 0.25 µg/mL against MRSA)

C

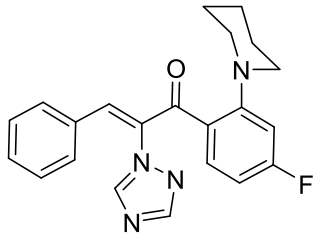

MIC: 0.25 µg/mL against MRSA)

D

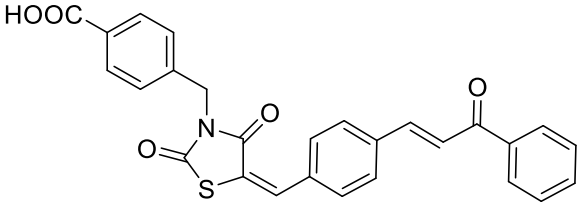

(MIC: 1 and 0.5 µg/mL against MRSA CCARM 3167 and 3506, respectively)

E

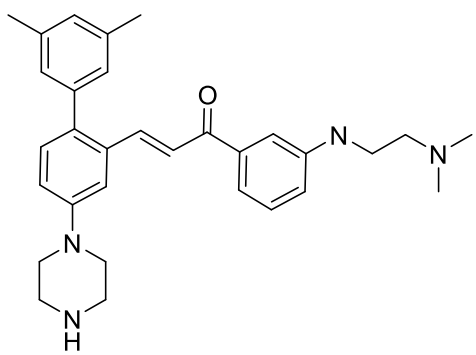

(MIC: 2 µM against MRSA)

doi:10.6342/NTU202400256

Figure. 1. (A–E) Chemical structures of some antibacterial chalcones with effective MIC against MRSA. The MIC values against MRSA are shown below the structures.

doi:10.6342/NTU202400256

Figure. 2

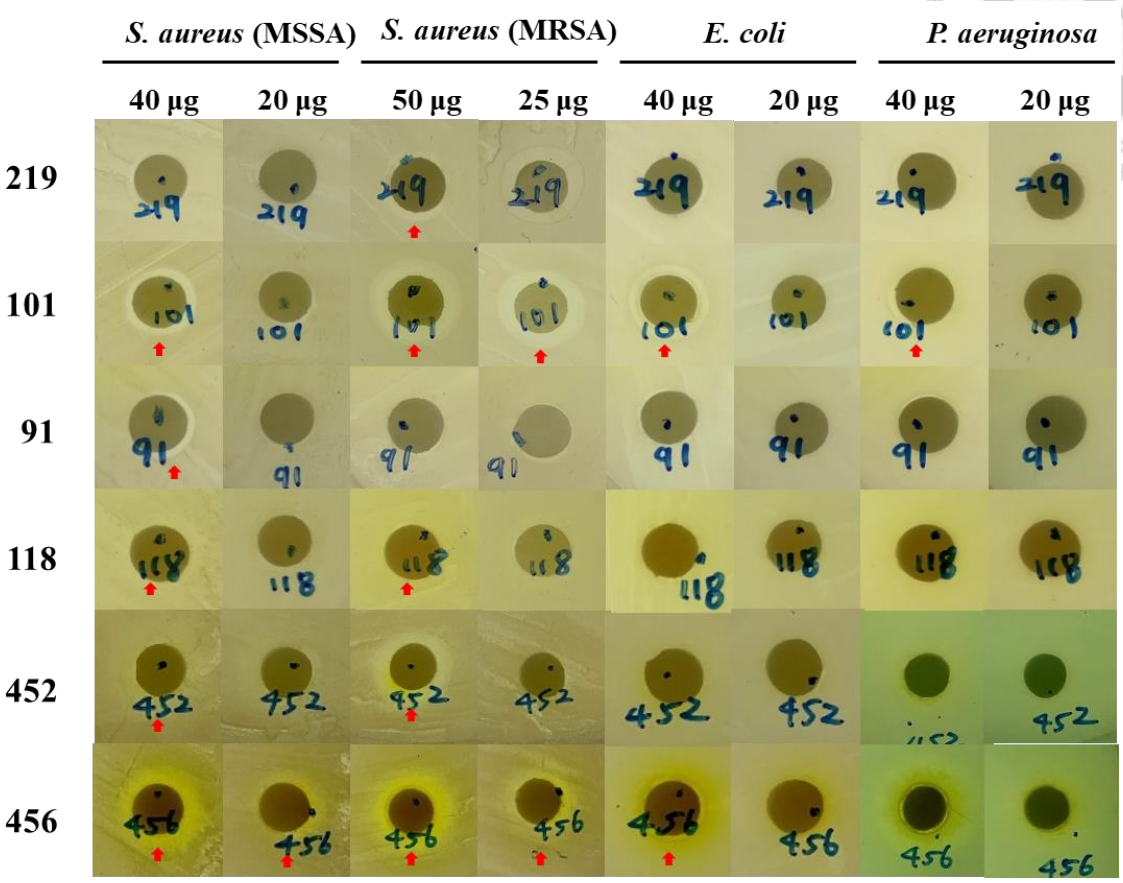

doi:10.6342/NTU202400256

Figure. 2. Inhibition zones of bacteria by the compounds **2b**, **2c**, **2d**, **2h**, **2i**, and **2j**. The red arrows indicated the edges of their bacterial inhibition zones.

doi:10.6342/NTU202400256

Figure. 3

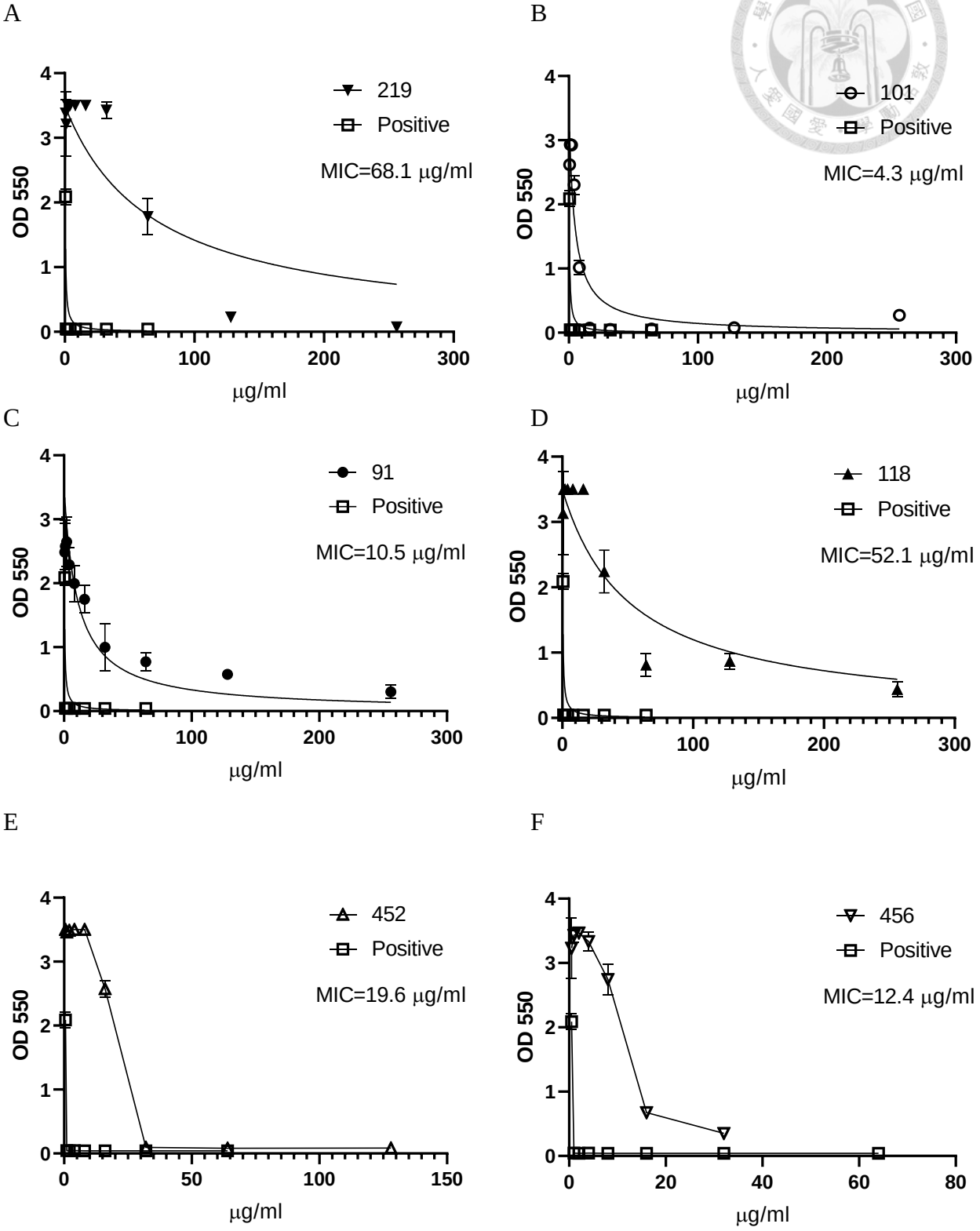

doi:10.6342/NTU202400256

G

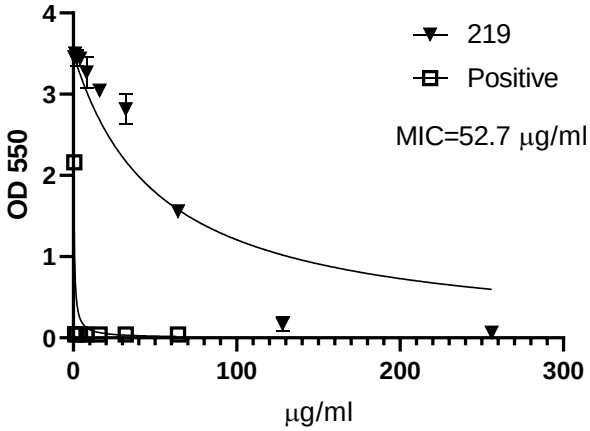

H

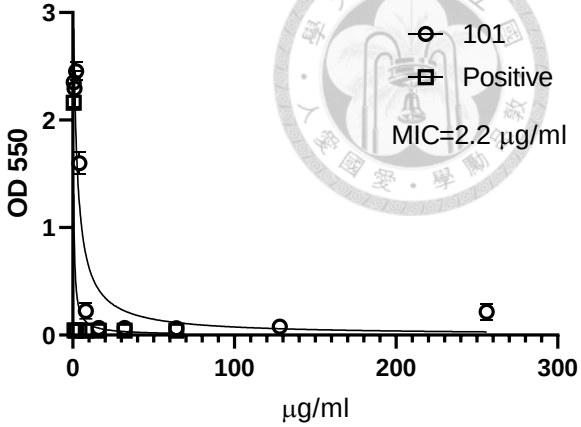

I

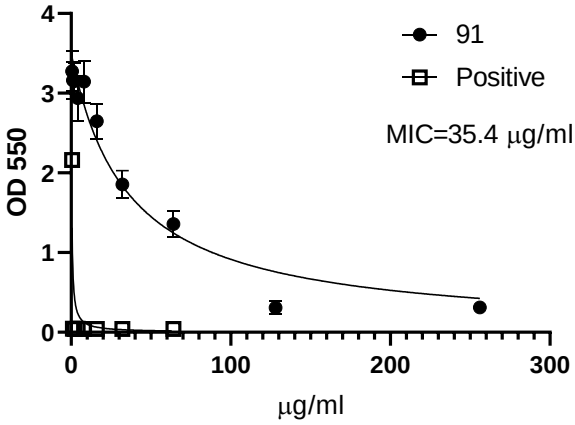

J

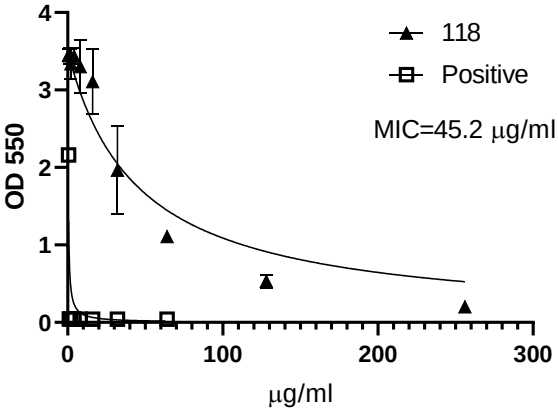

K

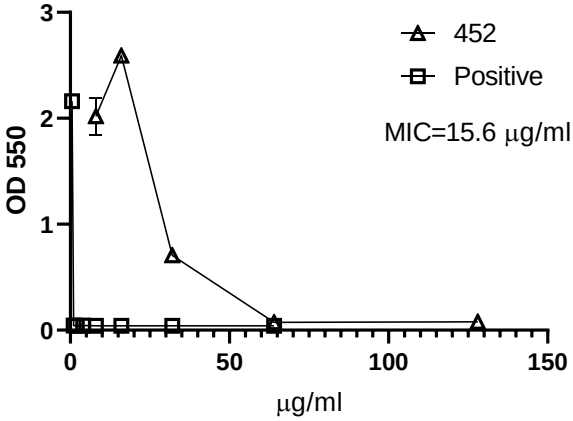

L

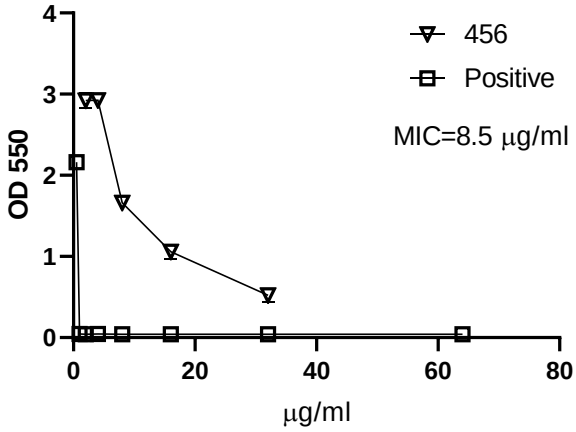

doi:10.6342/NTU202400256

Figure. 3. Inhibitors concentrations dependent bacterial inhibition curves for MIC measurements of the active compounds. (A–F) The MIC measurements of compounds **2b**, **2c**, **2d**, **2h**, **2i**, and **2j** against MRSA. The MIC values derived from the measurements were 68.1, 4.3, 10.5, 52.1, 19.6, and 12.4 μg/ml, respectively. (G–L) The MIC measurements of compounds **2b**, **2c**, **2d**, **2h**, **2i**, and **2j** against MSSA. The MIC values obtained from the measurements were 52.7, 2.2, 35.4, 45.2, 15.6, and 8.5 μM, respectively.

doi:10.6342/NTU202400256

Figure. 4

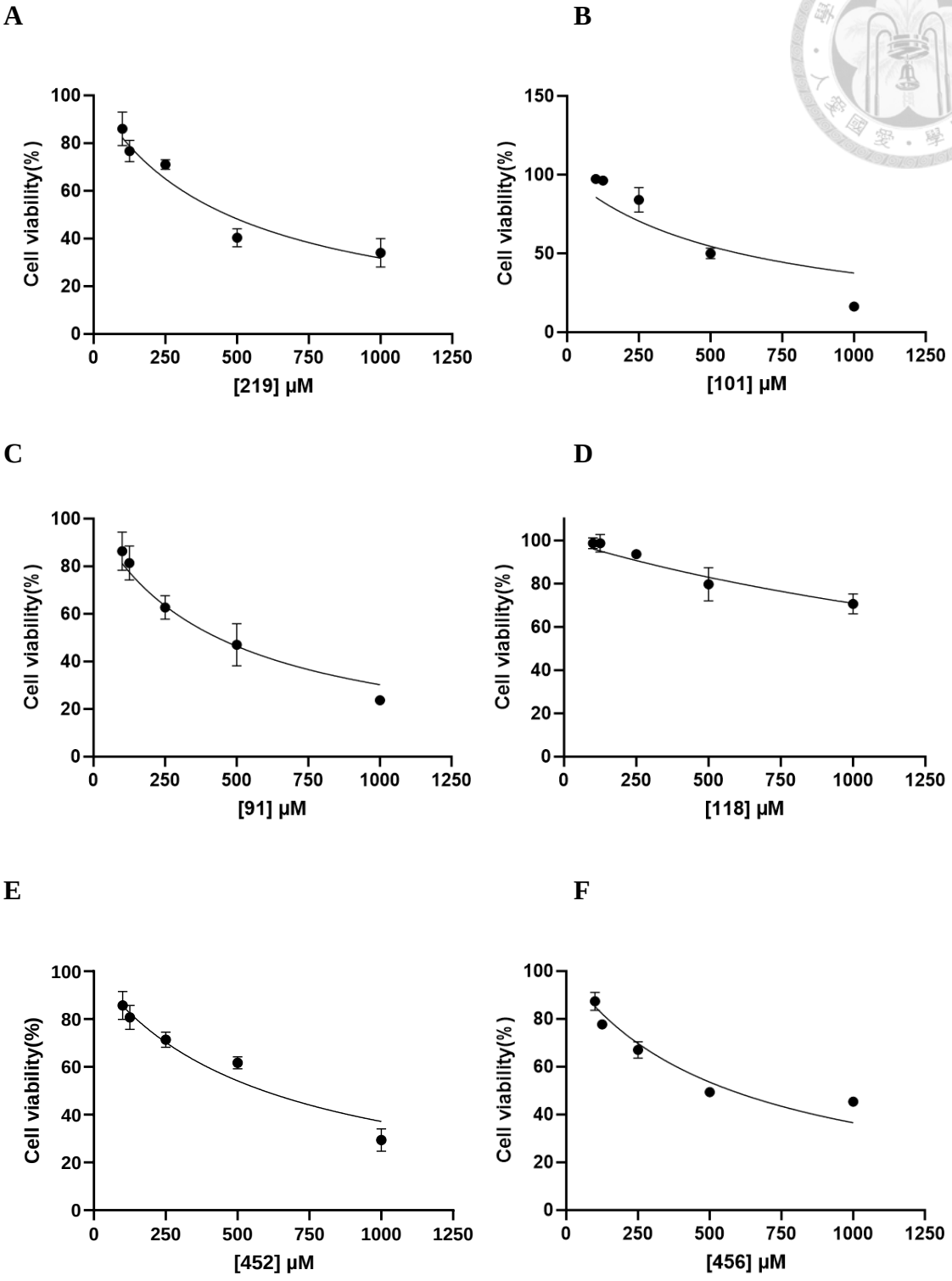

doi:10.6342/NTU202400256

Figure. 4. Inhibitors concentrations dependent cytotoxicity curves for CC_{50} measurements of the active compounds. (A–F) The measurements for compounds **2b**, **2c**, **2d**, **2h**, **2i**, and **2j** yield CC_{50} of 466.4 ± 42.4, 601.4 ± 120, 433.4 ± 40.9, >1000, 591.2 ± 53.3, and 576.8 ± 47.8 μM, respectively.

doi:10.6342/NTU202400256

Figure. 5

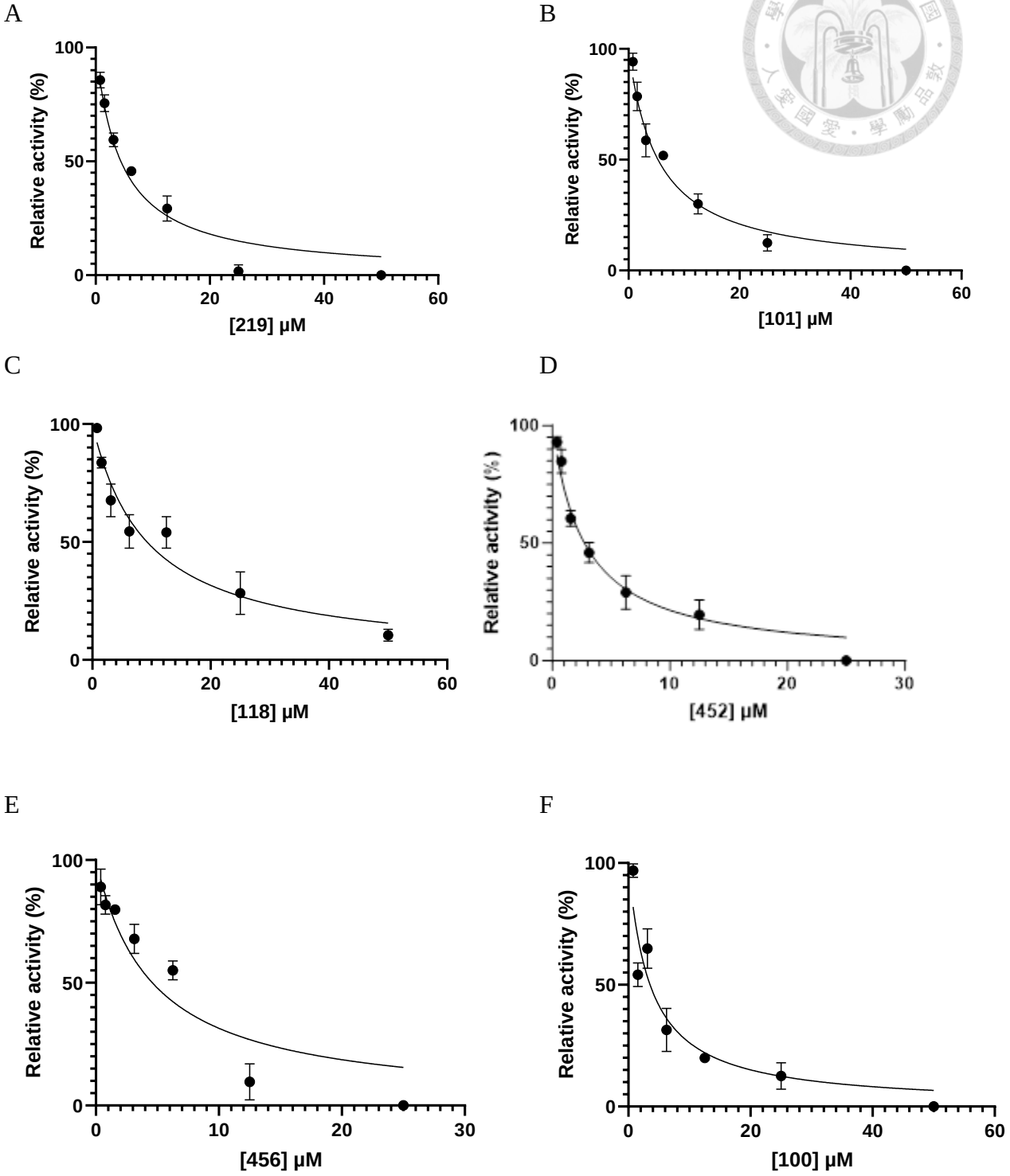

doi:10.6342/NTU202400256

Figure. 5. Dose-dependent inhibition curves of the active compound against SaUPPS. (A–F) The plots of decreasing SaUPPS reaction initial rates in the presence of increasing concentrations of **2b**, **2c**, **2h**, **2i**, **2j**, and **2a** were fitted with an equation to yield the IC_{50} of 4.41 ± 0.39, 5.30 ± 0.46, 9.24 ± 0.98, 2.74 ± 0.23, 4.59 ± 0.67, and 3.55 ± 0.49 μM, respectively.

doi:10.6342/NTU202400256

Figure. 6

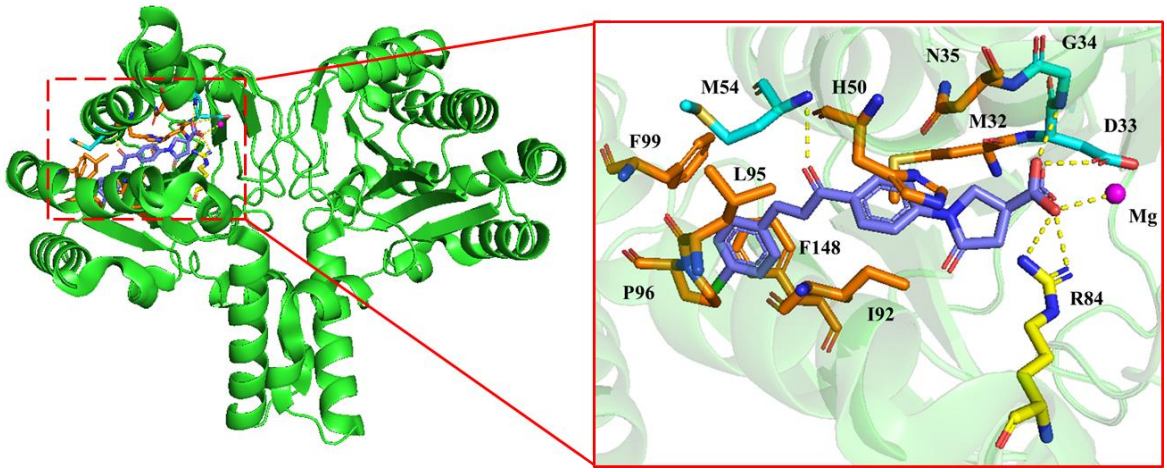

doi:10.6342/NTU202400256

Figure. 6. Simulated molecular interactions between compound **2c (101)** and SaUPPS. Compound **2c** (**101**) was docked against the active site of SaUPPS (PDB: 4H8E). The estimated binding energies of **2c** with SaUPPS was -138.9 kcal/mol. Compound **2c** is colored in purple, Mg ion in magenta, and the amino acid residues in cyan, orange, and yellow are involved in hydrogen-bonding, van der Waals, and electrostatic interactions, respectively. Left panel: the overall structure of SaUPPS enzyme in complex with **2c**. Right panel: The close-up views of simulated **2c**-SaUPPS interactions in the binding pocket are highlighted in red boxes with oxygen atoms shown in red stick and nitrogen atoms shown in blue stick.

doi:10.6342/NTU202400256

Figure Abstract

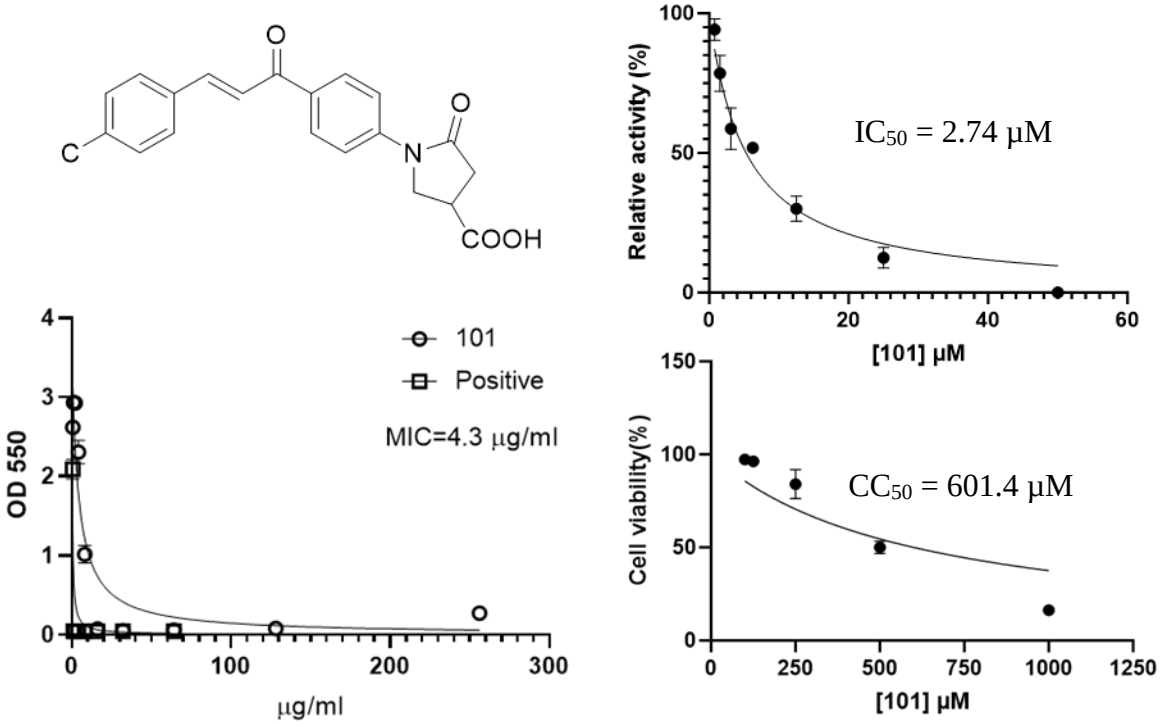

doi:10.6342/NTU202400256

6. Spectral data

6.1. Synthesis of 1-(4-(4-fluorostyrylcarbonyl)phenyl)-4-carboxy-2-pyrrolidinone 2b (219)

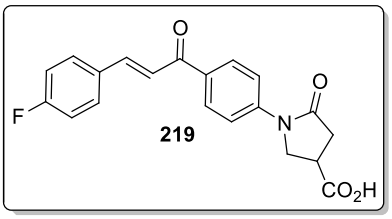

A mixture of 1-(4-acetylphenyl)-4-carboxy-2-pyrrolidinone **1**, (2.47 g, 10 mmol), 15 mmol of 4-fluorobenzaldehyde, and 15 mL of 10% NaOH in 10 mL of ethanol was refluxed for 4 h and cooled to room temperature. Then, 15 mL water was added and the mixture was acidified to pH 1–2 with aq HCl. The precipitate was filtered and washed with water. The product **219** was obtained as yellow solid (yield 42.4 %), mp 256–257 °C, ^{1}H NMR (400 MHz, DMSO-d6): δ 12.97 (s, 1H), 8.237 (d, *J* = 5.32 Hz, 2H), 8.09 (d, *J* = 15.68 Hz, 1H), 8.03–7.97 (m, 4H), 7.89 (d, *J* = 5.36 Hz, 2H), 7.79 (d, *J* = 12.64 Hz, 1H), 4.17–4.04 (m, 2H), 3.44–3.38 (m, 1H), 2.90–2.75 (m, 2H) ppm. ^{13}C NMR (100 MHz, d6-DMSO) δ: 187.10, 174.01, 172.60, 151.17, 146.11, 143.12, 132.64, 130.11, 129.34, 118.59, 116.88, 113.09, 49.79, 35.34, 35.02 ppm. HRMS (ESI): *m/z* calcd. for $C_{20}H_{17}FNO_4^+$ $[M+H]^+$: 354.1136, found 354.1148.

6.2. Synthesis of 1-(4-(4-Chlorostyrylcarbonyl)phenyl)-4-carboxy-2-pyrrolidinone 2c (101)

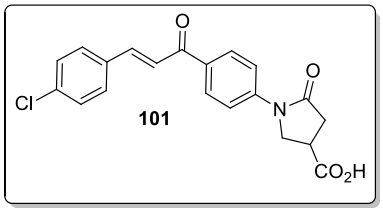

The compound **2c** was prepared by following the procedure described for the synthesis of **2b**, by using 4-chlorobenzaldehyde. dark yellow solid (yield 30.2 %), mp 224–225 °C, ^{1}H

doi:10.6342/NTU202400256

NMR (400 MHz, DMSO-d_6): δ 12.90 (s, 1H), 8.22 (d, *J* = 9.52 Hz, 2H), 8.01–7.93 (m, 3H), 7.89 (d, *J* = 8.92 Hz, 2H), 7.74 (d, *J* = 15.64 Hz, 1H), 7.55 (d, *J* = 8.52 Hz, 2H), 4.17–4.04 (m, 2H), 3.42–3.34 (m, 1H), 2.88 – 2.73 (m, 2H) ppm. ^{13}C NMR (100 MHz, DMSO-d_6): δ 192.98, 188.03, 174.61, 173.21, 143.78, 142.60, 137.38, 135.49, 134.21, 131.37, 131.05, 130.14, 129.42, 128.80, 128.37, 123.15, 119.00, 50.37, 35.92, 35.60 ppm. HRMS (ESI): *m/z* calcd. for $C_{20}H_{15}ClNO_4^-$ $[M+H]^-$: 368.0690, found 368.0653.

6.3. Synthesis of 1-(4-(4-bromostyrylcarbonyl)phenyl)-4-carboxy-2-pyrrolidinone 2d (91)

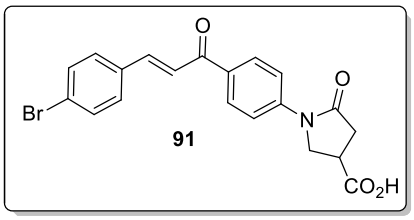

The compound **2d** was prepared by following the procedure described for the synthesis of **2b**, by using 4-bromobenzaldehyde. Dark yellow solid (yield 72.0 %), mp 232–233 ℃, ^{1}H NMR (400 MHz, DMSO-d6): δ 12.76 (s, 1H), 8.19 (d, *J* = 8.9 Hz, 2H), 7.99 (d, *J* = 15.6 Hz, 1H), 7.83–7.86 (m, 4H), 7.64–7.71 (m, 3H), 4.02–4.15 (m, 2H), 3.34–3.41 (m, 1H), 2.72–2.87 (m, 2H) ppm, ^{13}C NMR (100 MHz, d6-DMSO): δ 187.54, 174.05, 172.68, 143.28, 142.19, 134.04, 132.57, 131.84, 130.75, 129.64, 123.87, 122.70, 118.51, 49.84, 35.40, 35.08 ppm. HRMS (ESI): *m/z* calcd. for $C_{20}H_{17}BrNO_4^+$ $[M+H]^+$: 414.0335, found 414.0319.

doi:10.6342/NTU202400256

6.4. Synthesis of 1-(4-(4-hydroxystyrylcarbonyl)phenyl)-4-carboxy-2-pyrrolidinone 2e (400)

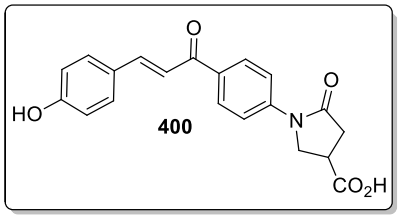

The compound **2e** was prepared by following the procedure described for the synthesis of **2b**, by using 4-hydroxybenzaldehyde. Light yellow solid (yield 63.2 %), mp 234–235 °C, ^{1}H NMR (400 MHz, DMSO-d_6): δ 12.83 (s, 1H), 10.07 (s, 1H), 8.18 (d, *J* = 8.92 Hz, 2H), 7.87–7.84 (m, 2H) 7.77–7.73 (m, 3H). 7.69 (d, *J* = 15.48 Hz, 1H), 6.85 (d, *J* = 8.68 Hz, 2H), 4.16–4.03 (m, 2H), 3.43–3.36 (m, 1H), 2.88–2.73 (m, 2H) ppm. ^{13}C NMR (100 MHz, DMSO-d_6): δ 188.00, 174.52, 173.05, 160.55, 144.56, 143.41, 133.63, 131.44, 129.84, 126.33, 119.01, 116.28, 50.30, 35.85, 35.53 ppm. HRMS (ESI): *m/z* calcd. for $C_{20}H_{18}NO_5^+$ $[M+H]^+$: 352.1179, found 352.1178.

6.5. Synthesis of 1-(4-(4-carboxystyrylcarbonyl)phenyl)-4-carboxy-2-pyrrolidinone 2f (221)

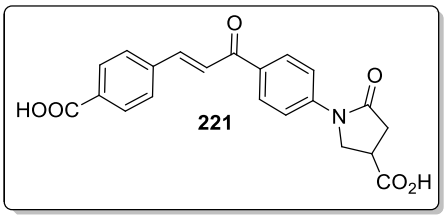

The compound **2f** was prepared by following the procedure described for the synthesis of **2b**, by using 4-carboxybenzaldehyde. Yellow solid (yield 48.0 %), mp 308–309 °C, ^{1}H NMR (400 MHz, MeOD): δ 7.96 (d, *J* = 8.8 Hz, 2H), 7.63–7.78 (m, 4H), 7.42 (d, *J* = 8.5 Hz, 2H), 6.72 (d, *J* = 8.8 Hz, 2H), 3.37–3.58 (m, 2H), 3.04–3.07 (m, 1H), 2.52–2.72 (m, 2H) ppm. ^{13}C NMR (100 MHz, MeOD): δ 189.62, 178.34, 176.81, 154.89, 142.37, 136.89, 135.52, 132.58, 130.88, 130.15, 127.18, 123.96, 112.62, 45.37, 43.38, 35.94 ppm. HRMS

doi:10.6342/NTU202400256

(ESI): *m/z* calcd. for $C_{21}H_{18}NO_6^+$ $[M+H]^+$: 380.1129, found 380.1129.

6.6. Synthesis of 1-[4-(4-Cyanostyrylcarbonyl)phenyl]-4-carboxy-2-pyrrolidinone 2g (182)

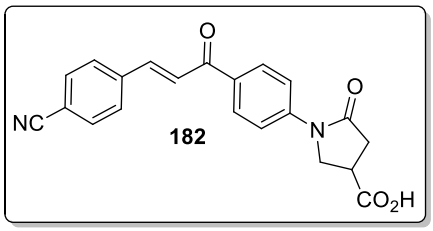

The compound **2g** was prepared by following the procedure described for the synthesis of **2b**, by using 4-cyanobenzaldehyde. Light yellow solid (yield 57.9 %), mp 250–251 ℃, ^{1}H NMR (400 MHz, DMSO-d6): δ 12.78 (s, 1H), 8.20 (d, *J* = 9.2 Hz, 2H), 7.97 (d, *J* = 15.6 Hz, 1H), 7.89–7.85 (m, 4H), 7.74 (d, *J* = 15.6 Hz, 1H), 7.46–7.44 (m, 2H), 4.15–4.02 (m, 2H), 3.42–3.36 (m, 1H), 2.87–2.72 (m, 2H) ppm. ^{13}C NMR (100 MHz, DMSO-d6): δ 187.46, 175.16, 173.99, 143.84, 141.23, 139.33, 132.68, 132.04, 129.78, 129.41, 125.25, 118.64, 118.64, 118.31, 112.16, 151.20, 36.60 ppm. HRMS (ESI): *m/z* calcd. for $C_{21}H_{17}N_2O_4^+$ $[M+H]^+$: 361.1183, found 361.1183.

6.7. Synthesis of 1-(4-(2-fluoro4-hydroxystyrylcarbonyl)phenyl)-4-carboxy-2-pyrrolidinone 2h (118)

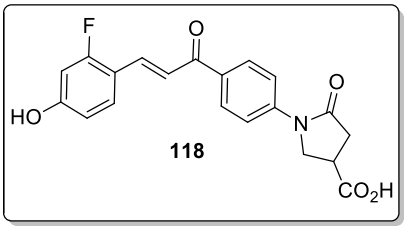

The compound **2h** was prepared by following the procedure described for the synthesis of **2b**, by using 4-hydroxy-2-fluorobenzaldehyde. Bright yellow solid, (yield 63.6 %), mp 260–261 ℃, ^{1}H NMR (400 MHz, DMSO-d6): δ 12.80 (s, 1H), 10.60 (s, 1H), 8.16 (d, *J* =

doi:10.6342/NTU202400256

8.92 Hz, 2H), 7.98 (t, *J* = 8.84, Hz, 1H), 7.88 (d, *J* = 8.96 Hz, 2H), 7.78 (d, *J* = 2.48, 2H), 6.74 (d, d, *J* = 10.96, Hz, 1H). 6.69 (d, d, *J* = 14.92, 1H), 4.16–4.03 (m, 2H), 3.43 – 3.36 (m, 1H), 2.89–2.73 (m, 2H) ppm. ^{13}C NMR (100 MHz, DMSO-d6): δ 187.91, 174.51, 173.09, 163.95, 162.20, 162.07, 161.46, 143.58, 135.96, 133.34, 129.90, 119.05, 113.92, 113.81, 113.13, 103.44, 103.21, 50.31, 35.85, 35.53 ppm. HRMS (ESI): *m/z* calcd. for $C_{20}H_{17}FNO_5^+$ $[M+H]^+$: 370.1085, found 370.1068.

6.8. Synthesis of 1-(4-(2,4-difluorostyrylcarbonyl)phenyl)-4-carboxy-2-pyrrolidinone 2i (452)

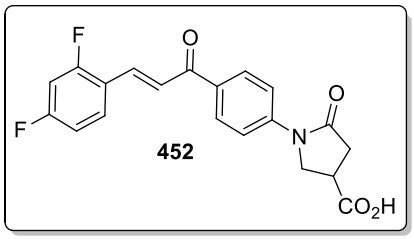

The compound **2i** was prepared by following the procedure described for the synthesis of **2b**, by using 2,4-difluorobenzaldehyde. Pale yellow solid (yield 67.4 %), mp 232–233 ℃, ^{1}H NMR (400 MHz, DMSO-d6): δ 12.82 (s, 1H), 8.12 (d, *J* = 8.72 Hz, 2H), 7.92 (t, *J* = 8.64 Hz, 3H), 7.57 (s, 2H), 7.11 (d, *J* = 3.32 Hz, 1H), 6.70–6.67 (m, 1H), 4.16–4.03 (m, 2H), 3.41–3.35 (m, 1H), 2.89–2.73 (m, 2H) ppm. ^{13}C NMR (100 MHz, d6-DMSO): δ 186.16, 175.74, 174.23, 153.34, 140.52, 132.21, 131.39, 131.17, 131.09, 125.68, 122.74, 166.27, 116.05, 111.41, 44.38, 41.64, 36.12 ppm.

HRMS (ESI): *m/z* calcd. for $C_{20}H_{15}F_2NO_2^+$ $[M+H]^+$: 371.0969, found 371.1025.

doi:10.6342/NTU202400256

6.9. Synthesis of 1-(4-(2-fluoro-4-chloro-styrylcarbonyl)phenyl)-4-carboxy-2-pyrrolidinone 2j (456)

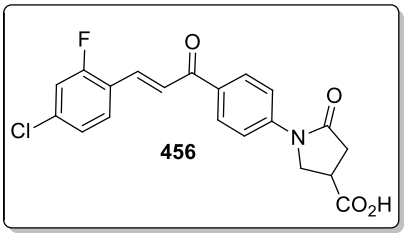

The compound **2j** was prepared by following the procedure described for the synthesis of **2b**, by using 2-fluoro-4-chlorobenzaldehyde. Yellow solid (yield 56.7 %), mp 256–257 °C, ^{1}H NMR (400 MHz, DMSO-d6): δ 13.02 (s, 1H), 8.48 (d, *J* = 13.36 Hz, 1H), 8.17–8.06 (m, 2H), 7.99 (d, *J* = 8.32 Hz, 2H), 7.83 (d, *J* = 8.48 Hz, 2H), 7.66–7.57 (m, 1H), 7.47–7.39 (m, 1H), 4.13–4.00 (m, 2H), 3.42–3.37 (m, 1H), 2.87–2.72 (m, 2H). 3.17–3.49 (m, 2H), 7.85 (d, *J* = 15.6 Hz, 2H) 7.25–7.30 (m, 2H), 7.63 (d, *J* = 15.6 Hz, 1H), 7.85 (d, *J* = 15.6 Hz, 1H), 7.91–7.99 (m, 4H) ppm, ^{13}C NMR (100 MHz, d6-DMSO): δ 187.46, 175.16, 173.99, 143.85, 141.23, 139.33, 132.68, 132.05, 129.78, 129.41, 129.10, 125.26, 118.64, 118.32, 174.2112.17, 51.20, 36.61 ppm.

HRMS (ESI): *m/z* calcd. for $C_{20}H_{16}ClFNO_4^+$ $[M+H]^+$: 388.0746, found 388.0755.

doi:10.6342/NTU202400256

7. References

1. Levy, S. B.; Marshall, B. Antibacterial Resistance Worldwide: Causes, Challenges and Responses. *Nat. Med.* **2004**, *10* (12 Suppl), S122–S129, DOI: 10.1038/nm1145
2. Ghosh, C.; Haldar, J. Membrane-Active Small Molecules: Designs Inspired by Antimicrobial Peptides. *ChemMedChem.* **2015**, *10* (10), 1606–1624, DOI: 10.1002/cmdc.201500299
3. Lim, S. M.; Webb, S. A. R. Nosocomial Bacterial Infections in Intensive Care Units. I: Organisms and Mechanisms of Antibiotic Resistance. *Anaesthesia* **2005**, *60* (9), 887–902, DOI: 10.1111/j.1365-2044.2005.04220.x
4. Fischbach, M. A.; Walsh. C. T. Antibiotics for Emerging Pathogen. *Science* **2009**, *325* (5944), 1089–1093, DOI: 10.1126/science.1176667
5. Bulter, M. S.; Gigante V.; Sati, H.; Paulin, S.; Al-Sulaiman, L.; Rex, J. H.; Fernandes, P.; Arias, C. A.; Paul, M.; Thwaites, G. E.; Czaplewski, L.; Alm, R. A.; Lienhardt, C.; Spigelman, M.; Silver, L. L.; Ohmagari, N.; Kozlov, R.; Harbarth, S.; Beyer, P. Analysis of the Clinical Pipeline of Treatments for Drug-Resistant Bacterial Infections: Despite Progress, More Action Is Needed. *Antimicrob. Agents Chemother.* **2022**, *66* (3), e0199121, DOI: 10.1128/AAC.01991-21.
6. Grundmann, H.; Aires-de-Sousa, M.; Boyce, J.; Tiemersma, E. Emergence and Resurgence of Meticillin-Resistant Staphylococcus aureus as a Public-Health Threat. *Lancet* **2006**, *368 (9538)*, 874–885, doi: 10.1016/S0140-6736(06)68853-3
7. Tacconelli, E.; Carrara, E.; Savoldi, A.; Harbarth, S.; Mendelson, M.; Monnet, D. L.; Pulcini, C.; Kahlmeter, G.; Kluytmans, J.; Carmeli, Y.; Ouellette, M.; Outterson, K.; Patel, J.; Cavaleri, M.; Cox, E. M.; Houchens, C. R.; Grayson, M. L.; Hansen, P.; Singh,

doi:10.6342/NTU202400256

N.; Theuretzbacher, U.; Magrini, N.; WHO Pathogens Priority List Working Group. Discovery, Research, and Development of New Antibiotics: the WHO Priority List of Antibiotic-Resistant Bacteria and Tuberculosis. *Lancet Infect. Dis.* **2018**, *18* (3), 318–327, DOI: 10.1016/S1473-3099(17)30753-3

8. Zhuang, C.; Zhang, W.; Sheng, C.; Zhang, W.; Xing, C.; Miao, Z. Chalcone: A Privileged Structure in Medicinal Chemistry. Chem. Rev. **2017**, *117* (12), 7762–7810, DOI: 10.1021/acs.chemrev.7b00020
9. Xu, M.; Wu, P.; Shen, F.; Ji, J.; Rakesh, K. P. Chalcone Derivatives and Their Antibacterial Activities: Current Development. *Bioorg. Chem.* **2019**, *91*, 103133, DOI: 10.1016/j.bioorg.2019.103133
10. Bhale, P. S.; Dongare, S. B.; Chanshetti, U. B. Synthesis and antimicrobial screening of chalcones containing imidazo[1,2-a] pyridine nucleus. *Res. J. Chem. Sci.* **2013**, *3*, 38–42.
11. Mohammad, F.; Rahaman, S. A.; Moinuddin, M. D. Synthesis and Antimicrobial Activity of 1-(2’,4’-Dichlorophenyl)-3-(Substituted aryl)-2-Propene-1-Ones. *Int. J. Life Sci. Pharm. Res.* **2009**, *2*, 82-87.
12. Asiri, A. M.; Khan, S. A. Synthesis, Characterization, and In Vitro Antibacterial Activities of Macromolecules Derived from Bis-Chalcone. *J. Heter. Chem.*, **2012**, *49* (6), 1434–1438, https://doi.org/10.1002/jhet.942
13. Asiri, A. M.; Khan, S. A. Green Synthesis, Characterization and Biological Evaluation of Novel Chalcones as Anti Bacterial Agents. *Ara. J. Chem.* **2017**, *10* (2), S2890–S2895, DOI: 10.1016/j.arabjc.2013.11.018

doi:10.6342/NTU202400256

14. Yadav, N.; Dixit, S. K..; Bhattacharya, A.; Mishra, L. C.; Sharma, M.; Awasthi, S. K.; Bhasin, V. K. Antimalarial Activity of Newly Synthesized Chalcone Derivatives in Vitro. *Chem. Biol. Drug Des.* **2012**, *80* (2), 340–347, DOI: 10.1111/j.1747-0285.2012.01383.x

15. Insuasty, B.; Ramírez, J.; Becerra, D.; Echeverry, C.; Quiroga, J.; Abonia, R.; Robledo, S. M.; Velez, I. D.; Upegui, Y.; Munoz, J. A.; Ospina, V.; Nogueras, M.; Cobo, J. An Efficient Synthesis of New Caffeine-Based Chalcones, Pyrazolines and Pyrazolo[3,4-b][1,4]diazepines as Potential Antimalarial, Antitrypanosomal and Antileishmanial Agents. *Eur. J. Med. Chem.* **2015**, *93*, 401–413, DOI: 10.1016/j.ejmech.2015.02.040

16. Salum, L. B.; Altei, W. F.; Chiaradia, L. D.; Cordeiro, M. N. S.; Canevarolo, R. R.; Melo, C. P. S.; Winter, E.; Mattei, B.; Daghestani, H. N.; Santos-Silva, M. C.; Creczynski-Pasa, T. B.; Yunes, R. A.; Yunes, J. A.; Andricopulo, A. D.; Day, B. W.; Nunes, R. J.; Vogt, A. Cytotoxic 3,4,5-Trimethoxychalcones as Mitotic Arresters and Cell Migration Inhibitors. *Eur. J. Med. Chem.* **2013**, *63*, 501–510, DOI: 10.1016/j.ejmech.2013.02.037

17. Murthy, Y. L. N.; Suhasini, K. P.; Pathania, A. S.; Bhushan, S.; Sastry. Y. N. Synthesis, Structure Activity Relationship and Mode of Action of 3-Substitutedphenyl-1-(2,2,8,8-Tetramethyl-3,4,9,10-Tetrahydro-2*H*, 8*H*-Pyrano[2,3-*f*]chromen-6-yl)-Propenones as Novel Anticancer Agents in Human Leukaemia HL-60 Cells. *Eur. J. Med. Chem.* **2013**, 62, 545–555, DOI: 10.1016/j.ejmech.2013.01.027

18. Liu, Z.; Tang, L.; Zou, P.; Zhang, Y.; Wang, Z.; Fang, Q.; Jiang, L.; Chen, G.; Xu, Z.; Zhang, H.; Liang, G. Synthesis and Biological Evaluation of Allylated and Prenylated

doi:10.6342/NTU202400256

Mono-Carbonyl Analogs of Curcumin as Anti-Inflammatory Agents. *Eur. J. Med. Chem.* **2014**, *74*, 671–682, DOI: 10.1016/j.ejmech.2013.10.061

19. Reichwald, C.; Shimony, O.; Dunkel, U.; Sacerdoti-Sierra, N.; Jaffe, C. L.; Kunick, C. 2-(3-Aryl-3-Oxopropen-1-yl)-9-Tert-Butyl-Paullones: a New Antileishmanial Chemotype. *J. Med. Chem.* **2008**, *51* (3), 659–665, DOI: 10.1021/jm7012166
20. Carvalho, S. A.; Feitosa, L. O.; Soares, M.; Costa, T. E. M. M.; Henriques, M. G.; Salomao, K.; Castro, S. L. D.; Kaiser, M.; Brun, R.; Wardell, J. L.; Wardell, S. M. S. V.; Trossini, G. H. G.; Andricopulo, A. D.; Silva, E. F. D.; Fraga, C. A. M. Design and Synthesis of New (E)-Cinnamic N-Acylhydrazones as Potent Antitrypanosomal Agents. *Eur. J. Med. Chem.* **2012**, *54*, 512–521, DOI: 10.1016/j.ejmech.2012.05.041
21. Sharma, H.; Patil, S.; Sanchez, T. W.; Neamati, N.; Schinazi, R. F.; Buolamwini, J. K. Synthesis, Biological Evaluation and 3D-QSAR Studies of 3-Keto Salicylic Acid Chalcones and Related Amides as Novel HIV-1 Integrase Inhibitors. *Bioorg. Med. Chem.* **2011**, *19* (6), 2030–2045, DOI: 10.1016/j.bmc.2011.01.047
22. Sivakumar, P. M.; Prabhakar, P. K.; Doble, M. Synthesis, Antioxidant Evaluation, and Quantitative Structure-Activity Relationship Studies of Chalcones. *Med. Chem. Res.* **2011**, *20* (4), 482–492, DOI: 10.1007/s00044-010-9342-1
23. Sashidhara, K. V.; Avula, S. R.; Mishra, V.; Palnati, G. R.; Singh, L. R.; Singh, N.; Chhonker, Y. S.; Swami, P.; Bhatta, R. S.; Palit, G. Identification of Quinoline-Chalcone Hybrids as Potential Antiulcer Agents. *Eur. J. Med. Chem.* **2015**, *89*, 638–653, DOI: 10.1016/j.ejmech.2014.10.068

doi:10.6342/NTU202400256

24. Greeff, J.; Joubert, J.; Malan, S. F.; Dyk, S. Antioxidant Properties of 4-Quinolones and Structurally Related Flavones. *Bioorg. Med. Chem.* **2012**, *20* (2), 809–818, DOI: 10.1016/j.bmc.2011.11.068
25. Ghani, S. B. A.; Weaver, L.; Zidan, Z. H.; Ali, H. M.; Keevil, C. W.; Brown, R. Microwave Assisted Synthesis and Antimicrobial Activities of Flavonoid Derivatives. *Bioorg. Med. Chem. Lett.* **2008**, *18* (2), 518–522, DOI: 10.1016/j.bmcl.2007.11.081
26. Yuan, Q.; Liu, Z.; Xiong, C.; Wu, L.; Wang, J.; Ruan, J. A Novel, Broad-Spectrum Antitumor Compound Containing the 1-Hydroxycyclohexa-2,5-Dien-4-One group: the Disclosure of a New Antitumor Pharmacophore in Protoapigenone 1. *Bioorg. Med. Chem. Lett.* **2011**, *21* (11), 3427–3430, DOI: 10.1016/j.bmcl.2011.03.108
27. Auffret, G.; Labaied, M.; Frappier, F.; Rasoanaivo, P.; Grellier, P.; Lewin, G. Synthesis and Antimalarial Evaluation of a Series of Piperazinyl Flavones. *Bioorg. Med. Chem. Lett.* **2007**, *17* (4), 959–963, DOI: 10.1016/j.bmcl.2006.11.051
28. Nakatsuka, T.; Tomimori, Y.; Fukuda, Y.; Nukaya, H. First Total Synthesis of Structurally Unique Flavonoids and Their Strong Anti-Inflammatory Effect. *Bioorg. Med. Chem. Lett.* **2004**, *14* (12), 3201–3203, DOI: 10.1016/j.bmcl.2004.03.108
29. Ares, J. J.; Outt, P. E.; Randall, J. L.; Johnston, J. N.; Murray, P. D.; O'Brien, L. M.; Weisshaar, P. S.; Ems, B. L. Synthesis and Biological Evaluation of Flavonoids and Related Compounds as Gastroprotective Agents. *Bioorg. Med. Chem. Lett.*, **1996**, *6* (8), 995–998, DOI: 10.1016/0960-894X(96)00134-5
30. Harborne, J.B.; Williams, C. A. Advances in Flavonoid Research Since 1992. *Phytochemistry* **2000**, *55* (6), 481–504, DOI: 10.1016/s0031-9422(00)00235-1

doi:10.6342/NTU202400256

31. Casano, G.; Dumetre, A.; Pannecouque, C.; Hutter, S.; Azas, N.; Robin, M. Synthesis and Biological Evaluation of Pyrazole Derivatives Containing Thiourea Skeleton as Anticancer Agents. *Bioorg. Med. Chem.* **2010**, *18* (16), 6012–6023, DOI: 10.1016/j.bmc.2010.06.067

32. Chu, W. C.; Baia, P. Y.; Yanga, Z. Q.; Cuia, D. Y.; Huaa, Y. G.; Yang, Y.; Yanga, Q. Q.; Zhanga, E.; Qina, S. Synthesis and Antibacterial Evaluation of Novel Cationic Chalcone Derivatives Possessing Broad Spectrum Antibacterial Activity. *Eur. J. Med. Chem.* **2018**, *143*, 905–921, DOI: 10.1016/j.ejmech.2017.12.009

33. Yin, B. T.; Yan, C. Y.; Peng, X. M.; Zhang, S. L.; Rasheed, S.; Geng, R. X.; Zhou, C. H. Synthesis and Biological Evaluation of α-Triazolyl Chalcones as a New Type of Potential Antimicrobial Agents and Their Interaction with Calf Thymus DNA and Human Serum Albumin. *Eur. J. Med. Chem.* **2014**, *71*, 148–159, DOI: 10.1016/j.ejmech.2013.11.003

34. Liu, X. F.; Zheng, C. J.; Sun, L. P.; Liu, X. K.; Piao, H. R. Synthesis of New Chalcone Derivatives Bearing 2,4-Thiazolidinedione and Benzoic Acid Moieties as Potential Anti-Bacterial Agents. *Eur. J. Med. Chem.* **2011**, *46*(8):3469–73, DOI: 10.1016/j.ejmech.2011.05.012.

35. Nielsen, S. F.; Larsen, M.; Boesen, T.; Schønning, K.; Kromann, H. Cationic Chalcone Antibiotics. Design, Synthesis, and Mechanism of Action. *J. Med. Chem.* **2005**, *48* (7), 2667–2677, DOI: 10.1021/jm049424k

36. Teng, K. H.; Liang, P. H. Structures, Mechanisms and Inhibitors of Undecaprenyl Diphosphate Synthase: A cis-Prenyltransferase for Bacterial Peptidoglycan Biosynthesis. *Bioorg. Chem.* **2012**, *43*, 51–57, DOI: 10.1016/j.bioorg.2011.09.004

doi:10.6342/NTU202400256

37. Sinko, W.; Wang, Y.; Zhu, W.; Zhang, Y.; Feixas, F.; Cox, C. L.; Mitchell, D. A.; Oldfield, E.; McCammon, J. A. Undecaprenyl Diphosphate Synthase Inhibitors: Antibacterial Drug Leads. *J. Med. Chem.* **2014**, *57* (13), 5693–5701, DOI: 10.1021/jm5004649.

38. Fatha, M. A.; Czarny, T. L.; Myers, C. L.; Worrall, L. J.; French, S.; Conrady, D. G.; Wang, Y.; Oldfield, E.; Strynadka, N. C.; Brown, E. D. Antagonism Screen for Inhibitors of Bacterial Cell Wall Biogenesis Uncovers an Inhibitor of Undecaprenyl Diphosphate Synthase. *Proc. Natl. Acd. Sci., USA* **2015**, *112* (35), 11048–11053, DOI: 10.1073/pnas.1511751112

39. Wang, Y.; Desai, J.; Zhang, Y.; Malwal, S. R.; Shin, C. J.; Feng, X.; Sun, H.; Liu, G.; Guo, R. T.; Oldfield, E. Bacterial Cell Growth Inhibitors Targeting Undecaprenyl Diphosphate Synthase and Undecaprenyl Diphosphate Phosphatase. *ChemMedchem.* **2016**, *11* (20), 2311–219, DOI: 10.1002/cmdc.201600342

40. Malwal, S. R.; Chen, L.; Hicks, H.; Qu, F.; Liu, W.; Shillo, A.; Law, W. X.; Zhang, J.; Chandnani, N.; Han, X.; Zheng, Y.; Chen, C. C.; Guo, R. T.; AbdelKhalek, A.; Seleem, M. N.; Oldfield, E. Discovery of Lipophilic Bisphosphonates that Target Bacterial Cell Wall and Quinone Biosynthesis. *J. Med. Chem.* **2019**, *62* (5), 2564–2581, DOI: 10.1021/acs.jmedchem.8b01878.

41. Song, J.; Malwal, S. R.; Baig, N.; Schurig-Briccio, L. A.; Gao, Z.; Vaidya, G. S.; Yang, K.; Abutaleb, N. S.; Seleem, M. N.; Gennis, R. B.; Pogorelov, T. V.; Oldfield, E.; Feng, X. Discovery of Prenyltransferase Inhibitors with In Vitro and In Vivo Antibacterial Activity. *ACS Infect. Dis.* **2020**, *6* (11), 2979–2993, DOI: 10.1021/acsinfecdis.0c00472.

doi:10.6342/NTU202400256

42. Kuo, C. J.; Guo, R. T.; Lu, I. L.; Liu, H. G.; Wu, S. Y.; Ko, T. P.; Wang, A. H.-J.; Liang, P. H. Structure-Based Inhibitors Exhibited Differential Activities against H. pylori and E. coli Undecaprenyl Pyrophosphate Synthases. *J. Biomed. Biotechnol.* **2008**, *2008*, 841312, DOI: 10.1155/2008/841312

43. Voskiene, A.; Mickevicius, V.; Mikulskiene, G. Synthesis and Structural Characterization of Products Condensation 4-Carboxy-1-(4-Styrylcarbonylphenyl)-2-Pyrrolidinones with Hydrazines. *Arkivoc* **2007**, *XV*, 303–314, DOI: 10.3998/ark.5550190.0008.f29.

44. O'Boyle, N. M.; Banck, M.; James, C. A.; Morley, C.; Vandermeersch, T.; Hutchison, G. R.; Open Babel: An Open Chemical Toolbox 2011. *J. Cheminform.* **2011**, *3*, 33, DOI: 10.1186/1758-2946-3-33.

45. Lipinski, C. A., Lead-and Drug-Like Compounds: the Rule-of-Five Revolution. *Drug Discov.* Today Technol. **2004**, *1* (4), 337–341, DOI: 10.1016/j.ddtec.2004.11.007.

46. Jayaram, B.; Singh, T.; Mukherjee, G.; Mathur, A.; Shekhar, S.; Shekhar, V. A Freely Accessible Web-Server for Target Directed Lead Molecule Discovery. *BMC bioinformatics* **2012**, *13* (Suppl 17), 1−13. doi: 10.1186/1471-2105-13-S17-S7.

47. Pires, D. E. V.; Blundell, T. L.; Ascher, D. B. pkCSM: Predicting Small-Molecule Pharmacokinetic and Toxicity Properties Using Graph-Based Signatures. *J. Med. Chem.* **2015**, *58*, 4066–4072. doi: 10.1021/acs.jmedchem.5b00104.

48. Palla. S. R.; Li, C. W.; Chao, T. L.; Lo, H. L. V.; Liu, J. J.; Pan, M. Y. C.; Chiu, Y. T.; Lin, W. C.; Hu, C. W.; Yang, C. M.; Chen, Y. Y.; Fang, J. T.; Lin, S. W.; Lin, Y. T.; Lin, H. C.; Kuo, C.J.; Wang, L. H. C.; Chang, S. Y.; Liang, P. H. Synthesis, Evaluation, and Mechanism of 1-(4-(Arylethylenylcarbonyl)phenyl)-4-Carboxy-2-Pyrrolidinones

doi:10.6342/NTU202400256

as Potent Reversible SARS-CoV-2 Entry Inhibitors. Antiviral Res. **2023**, *219*, 105735, DOI: 10.1016/j.antiviral.2023.105735

49. Wang, J.; Liu, H.; Zhao, J.; Gao, H.; Zhou, L.; Liu, Z.; Chen, Y.; Sui, P. Antimicrobial and Antioxidant Activities of the Root Bark Essential Oil of Periploca Sepium and Its Main Component 2-Hydroxy-4-Methoxybenzaldehyde. *Molecules* **2010**, *15* (8), 5807–5817. https://doi.org/10.3390/molecules15085807

doi:10.6342/NTU202400256

NMR spectra (^{1}H top and ^{13}C bottom) of the synthesized compounds

1

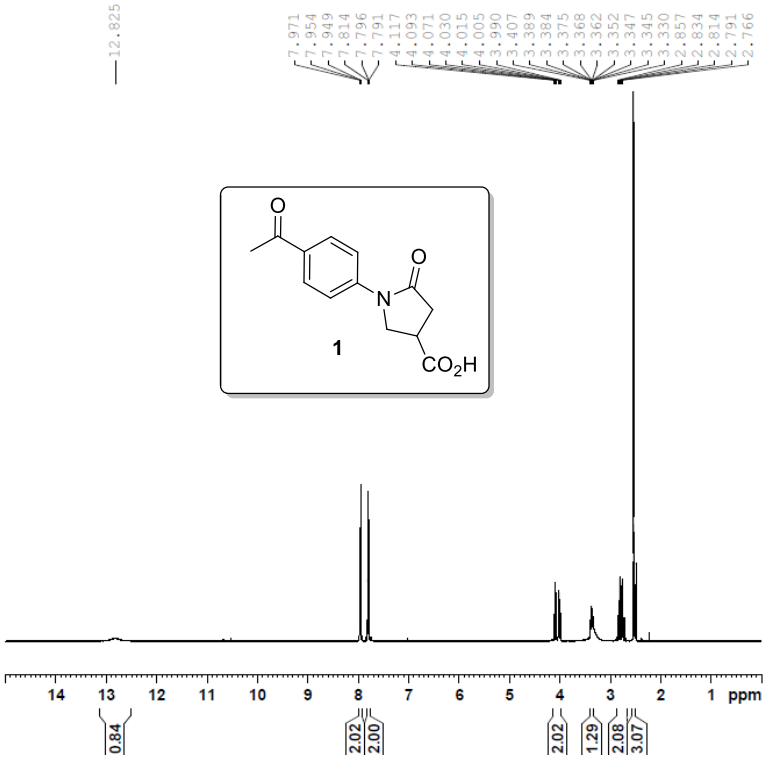

BRUKER

Current Data Parameters
NAME compound 1
EXPNO 1
PROCNO 1

F2 - Acquisition Parameters
Date_ 20170808
Time 15.37 h
INSTRUM spect
PROBHD Z108618_0411 (
PULPROG zg30
TD 32768
SOLVENT DMSO
NS 10
DS 0
SWH 8802.817 Hz
FIDRES 0.537281 Hz
AQ 1.8612224 sec
RG 165.3
DW 56.800 usec
DE 14.47 usec
TE 298.9 K
D1 1.00000000 sec
TD0 1
SFO1 400.1328009 MHz
NUC1 1H
P1 15.50 usec
PLW1 10.89999962 W

F2 - Processing parameters
SI 131072
SF 400.1300076 MHz
WDW EM
SSB 0
LB 0 Hz
GB 0
PC 1.00

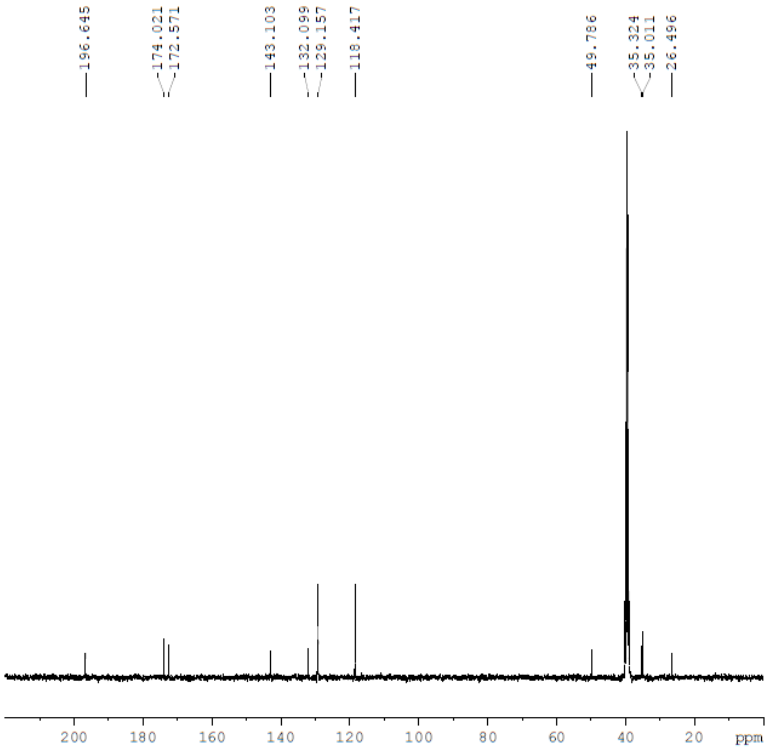

Current Data Parameters
NAME compound 1
EXPNO 2
PROCNO 1

F2 - Acquisition Parameters
Date_ 20170808
Time 15.58 h
INSTRUM spect
PROBHD Z108618_0411 (
PULPROG zgpg30
TD 65536
SOLVENT DMSO
NS 123
DS 4
SWH 28409.092 Hz
FIDRES 0.866977 Hz
AQ 1.1534336 sec
RG 212.49
DW 17.600 usec
DE 6.50 usec
TE 298.9 K
D1 2.00000000 sec
D11 0.03000000 sec
TD0 1
SFO1 100.6258487 MHz
NUC1 13C
P1 10.50 usec
PLW1 47.29999924 W
SFO2 400.1316005 MHz
NUC2 1H
CPDPRG[2 waltz16
PCPD2 90.00 usec
PLW2 10.89999962 W
PLW12 0.32330000 W
PLW13 0.16236000 W

F2 - Processing parameters
SI 32768
SF 100.6128735 MHz
WDW EM
SSB 0
LB 3.00 Hz
GB 0
PC 1.40

doi:10.6342/NTU202400256

2a (100)

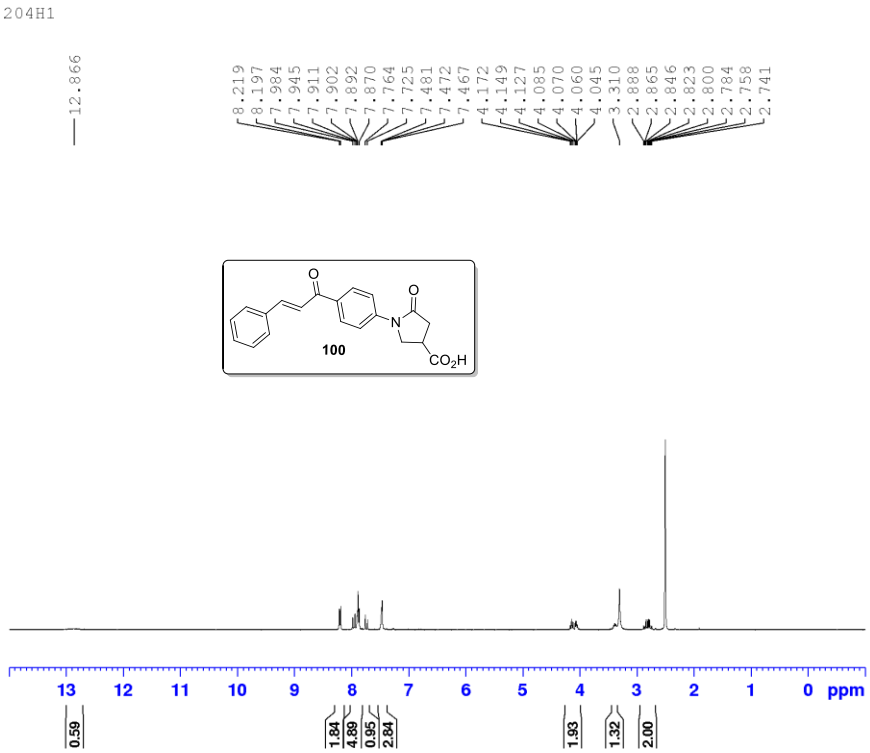


```
Current Data Parameters
NAME                 204H1
EXPNO                    3
PROCNO                   1

F2 - Acquisition Parameters
Date_             20210819
Time                 11.05 h
INSTRUM              spect
PROBHD    Z108618_0411 (
PULPROG               zg30
TD                   32768
SOLVENT               DMSO
NS                      30
DS                       0
SWH               8802.817 Hz
FIDRES            0.537281 Hz
AQ               1.8612224 sec
RG                  212.49
DW                  56.800 usec
DE                   14.47 usec
TE                   297.8 K
D1               1.00000000 sec
TD0                      1
SFO1            400.1328009 MHz
NUC1                    1H
P1                   15.50 usec
PLW1            9.89999962 W

F2 - Processing parameters
SI                     131072
SF              400.1300000 MHz
WDW                        EM
SSB                         0
LB                          0 Hz
GB                          0
PC                       1.00
```

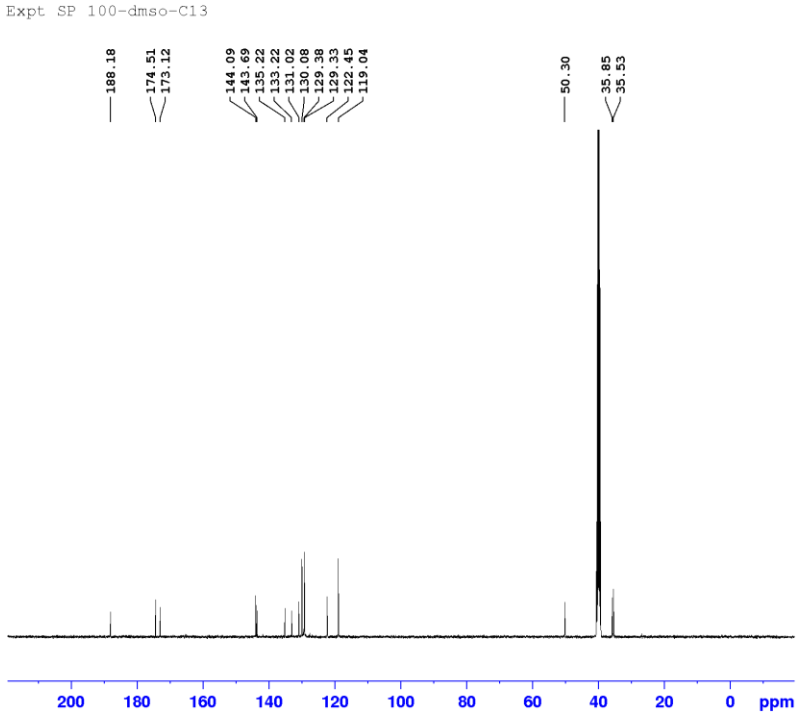


```
Current Data Parameters
NAME      Expt SP 100-dmso-C13
EXPNO                      16
PROCNO                      2

F2 - Acquisition Parameters
Date_             20230117
Time                 10.52
INSTRUM              spect
PROBHD   5 mm PABBO BB/
PULPROG             zgpg30
TD                   32768
SOLVENT               DMSO
NS                     2445
DS                        0
SWH              24038.461 Hz
FIDRES            0.733596 Hz
AQ               0.6815744 sec
RG                  198.09
DW                  20.800 usec
DE                    6.50 usec
TE                   300.8 K
D1               2.00000000 sec
D11              0.03000000 sec
TD0                       1

======== CHANNEL f1 ========
SFO1            100.6228298 MHz
NUC1                    13C
P1                   10.00 usec
PLW1            49.50000000 W

======== CHANNEL f2 ========
SFO2            400.1316005 MHz
NUC2                     1H
CPDPRG[2            waltz16
PCPD2                90.00 usec
PLW2            12.50000000 W
PLW12            0.34722000 W
PLW13            0.28125000 W

F2 - Processing parameters
SI                     32768
SF              100.6127685 MHz
WDW                        EM
SSB                         0
LB                       2.00 Hz
GB                          0
PC                       1.00
```


doi:10.6342/NTU202400256

2b (22)

Expt SP 22-223-3

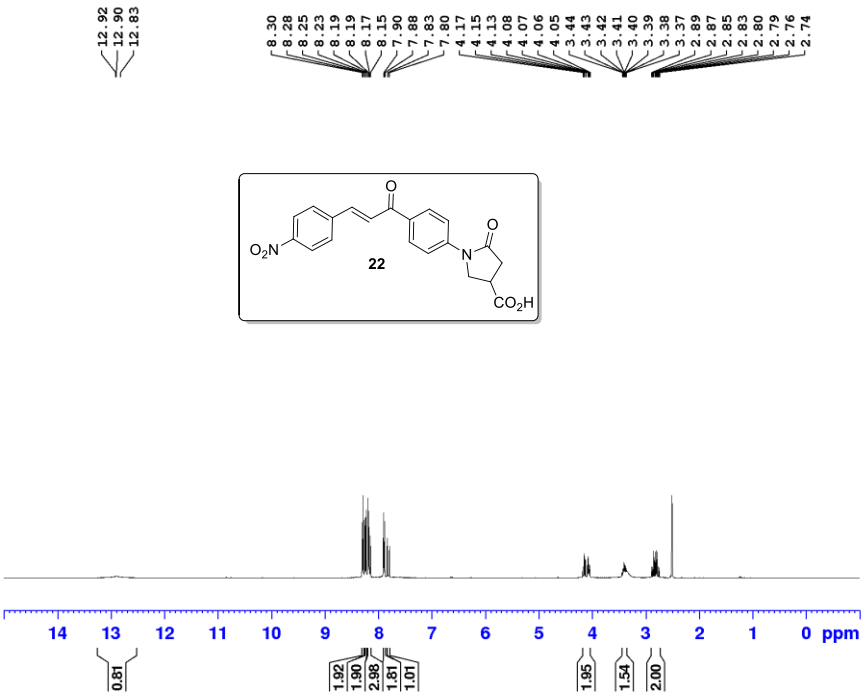


```
Current Data Parameters
NAME      Expt SP 22-223-3
EXPNO                    5
PROCNO                   1

F2 - Acquisition Parameters
Date_            20211223
Time                 9.42
INSTRUM             spect
PROBHD    5 mm PABBO BB/
PULPROG             zg30
TD                  32768
SOLVENT              DMSO
NS                     16
DS                      0
SWH             7211.539 Hz
FIDRES          0.220079 Hz
AQ             2.2719147 sec
RG                 128.9
DW                69.333 usec
DE                 10.06 usec
TE                 296.1 K
D1             2.00000000 sec
TD0                     1

======== CHANNEL f1 =======
SFO1          400.1324008 MHz
NUC1                    1H
P1                  15.00 usec
PLW1          11.39999962 W

F2 - Processing parameters
SI                  16384
SF            400.1300000 MHz
WDW                    EM
SSB                     0
LB                      0 Hz
GB                      0
PC                   1.00
```

Expt SP 22-223-3 carbon

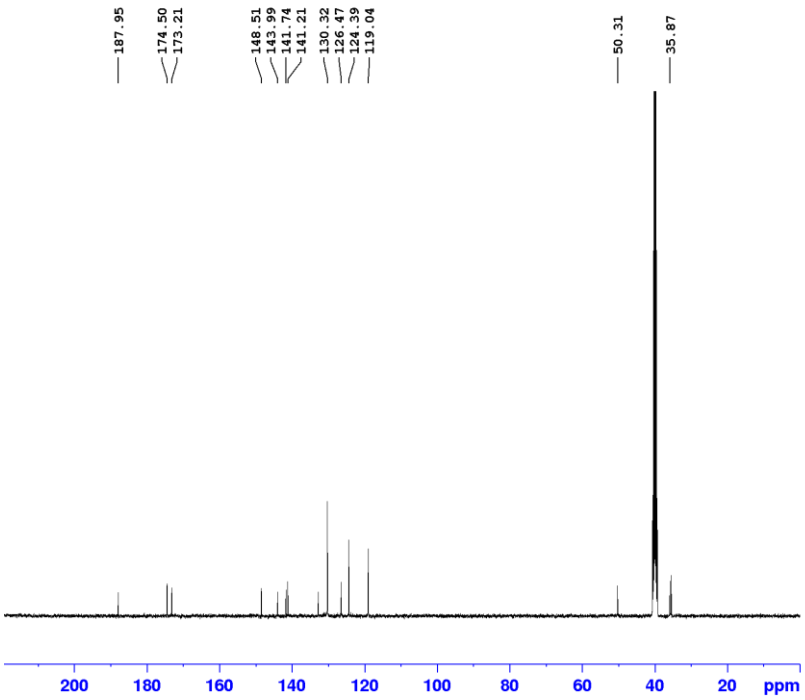


```
Current Data Parameters
NAME      Expt SP 22-223-3 carbor
EXPNO                    7
PROCNO                   2

F2 - Acquisition Parameters
Date_            20211223
Time                14.02
INSTRUM             spect
PROBHD    5 mm PABBO BB/
PULPROG            zgpg30
TD                  32768
SOLVENT              DMSO
NS                   1346
DS                      0
SWH            24038.461 Hz
FIDRES          0.733596 Hz
AQ             0.6815744 sec
RG                 198.09
DW                 20.800 usec
DE                  6.50 usec
TE                 297.9 K
D1             2.00000000 sec
D11            0.03000000 sec
TD0                     1

======== CHANNEL f1 =======
SFO1          100.6228298 MHz
NUC1                   13C
P1                  10.00 usec
PLW1          49.50000000 W

======== CHANNEL f2 =======
SFO2          400.1316005 MHz
NUC2                    1H
CPDPRG[2          waltz16
PCPD2               90.00 usec
PLW2          12.50000000 W
PLW12          0.34722000 W
PLW13          0.28125000 W

F2 - Processing parameters
SI                  32768
SF            100.6127685 MHz
WDW                    EM
SSB                     0
LB                   2.00 Hz
GB                      0
PC                   1.00
```


doi:10.6342/NTU202400256

2c (89)

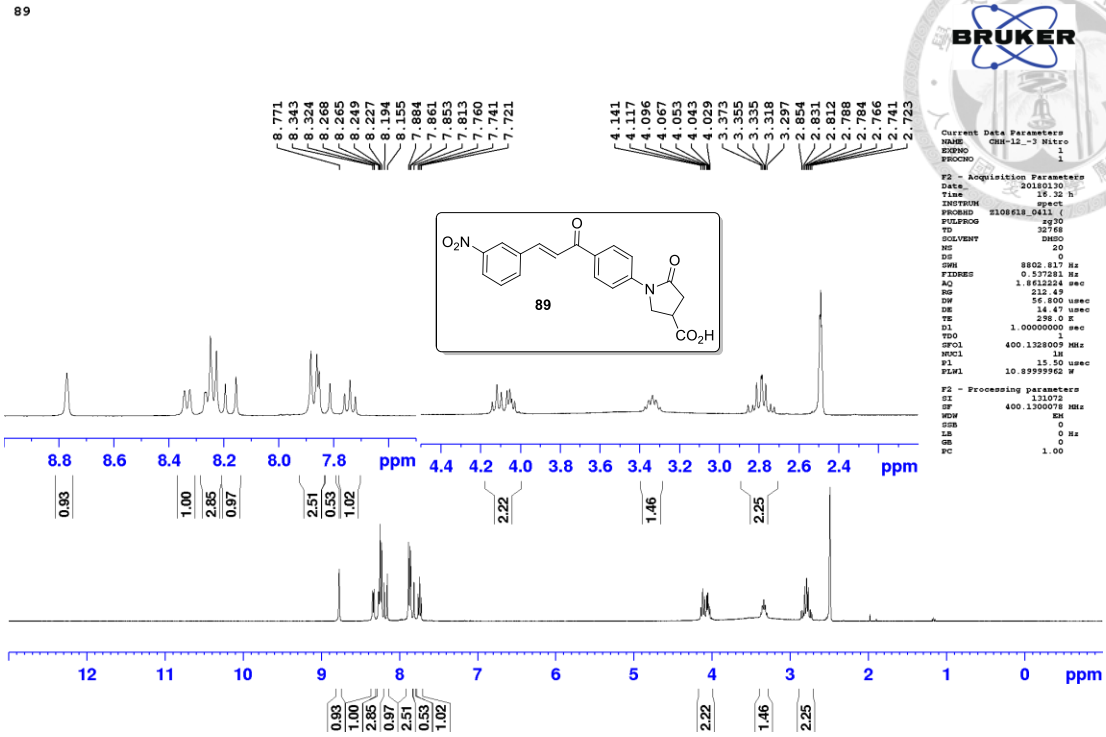

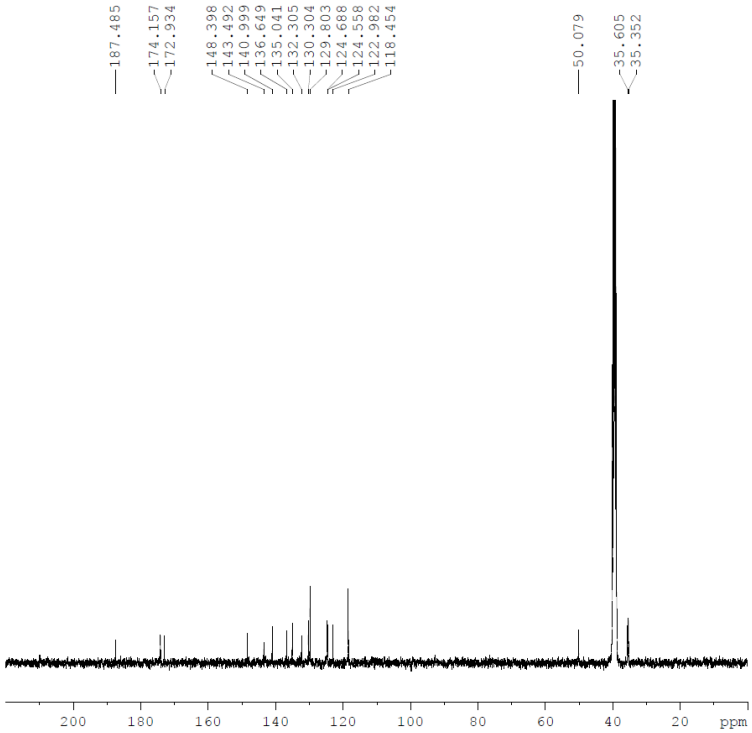

doi:10.6342/NTU202400256

2d (105)

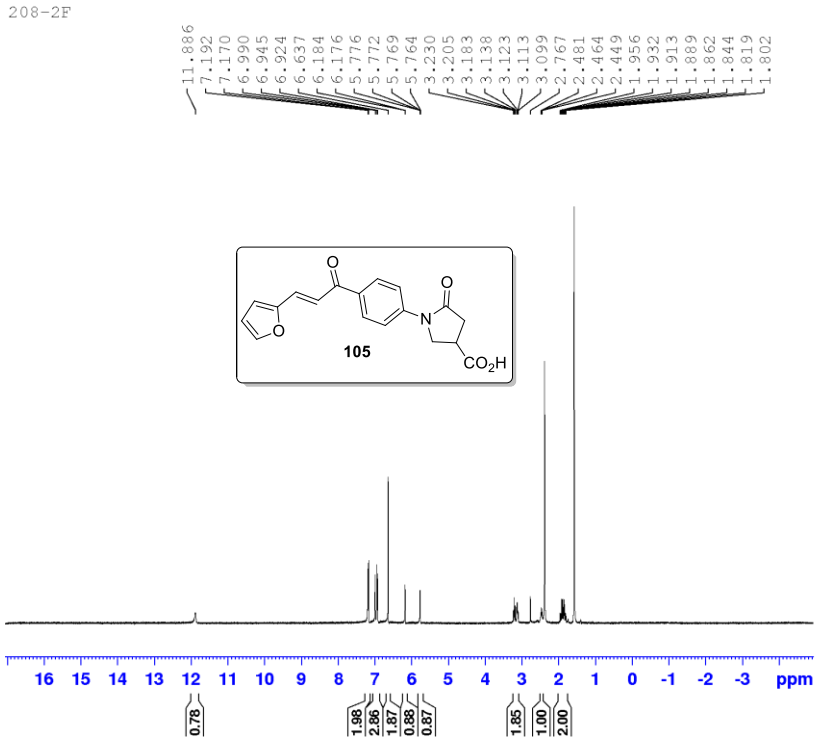


```
Current Data Parameters
NAME                 208-2F
EXPNO                     5
PROCNO                    1

F2 - Acquisition Parameters
Date_              20210820
Time                   9.00 h
INSTRUM               spect
PROBHD   Z108618_0411 (
PULPROG                zg30
TD                    32768
SOLVENT               DMSO
NS                       50
DS                        0
SWH               8802.817 Hz
FIDRES            0.537281 Hz
AQ               1.8612224 sec
RG                  212.49
DW                  56.800 usec
DE                   14.47 usec
TE                   298.3 K
D1              1.00000000 sec
TD0                       1
SFO1           400.1328009 MHz
NUC1                     1H
P1                    15.50 usec
PLW1            9.89999962 W

F2 - Processing parameters
SI                   131072
SF             400.1303738 MHz
WDW                      EM
SSB                       0
LB                        0 Hz
GB                        0
PC                     1.00
```

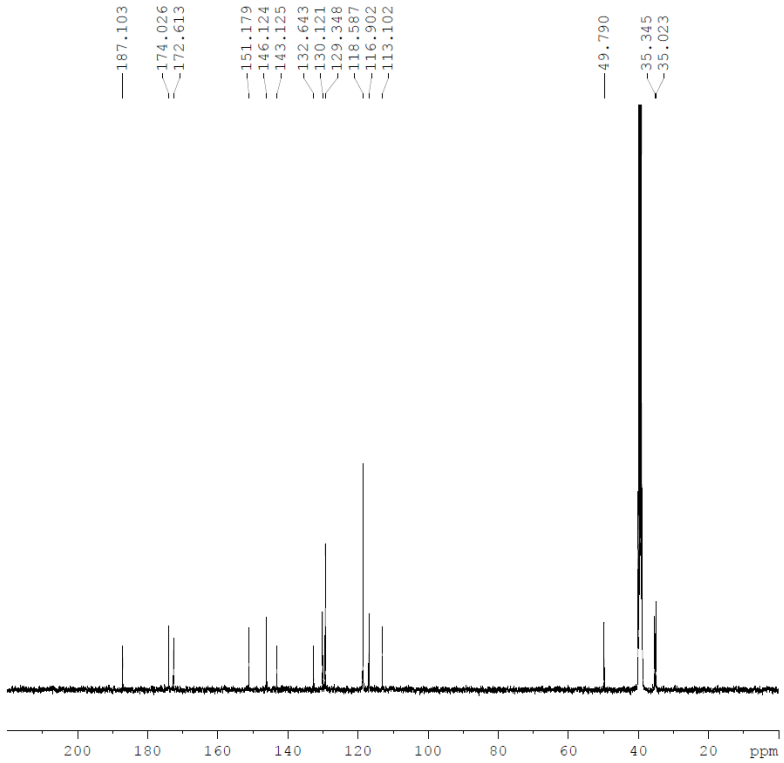


```
Current Data Parameters
NAME          compound 2k
EXPNO               11112
PROCNO                  1

F2 - Acquisition Parameters
Date_            20190611
Time                16.51 h
INSTRUM             spect
PROBHD   Z108618_0411 (
PULPROG            zgpg30
TD                  65536
SOLVENT              DMSO
NS                    718
DS                      4
SWH             28409.092 Hz
FIDRES           0.866977 Hz
AQ              1.1534336 sec
RG                 212.49
DW                 17.600 usec
DE                   6.50 usec
TE                  297.7 K
D1             2.00000000 sec
D11            0.03000000 sec
TD0                     1
SFO1          100.6258487 MHz
NUC1                  13C
P1                  10.50 usec
PLW1          42.50000000 W
SFO2          400.1316005 MHz
NUC2                    1H
CPDPRG[2          waltz16
PCPD2               90.00 usec
PLW2           9.89999962 W
PLW12          0.29363999 W
PLW13          0.14747000 W

F2 - Processing parameters
SI                   32768
SF            100.6128180 MHz
WDW                     EM
SSB       0
LB                   3.00 Hz
GB        0
PC                   1.40
```


doi:10.6342/NTU202400256

2e (143)

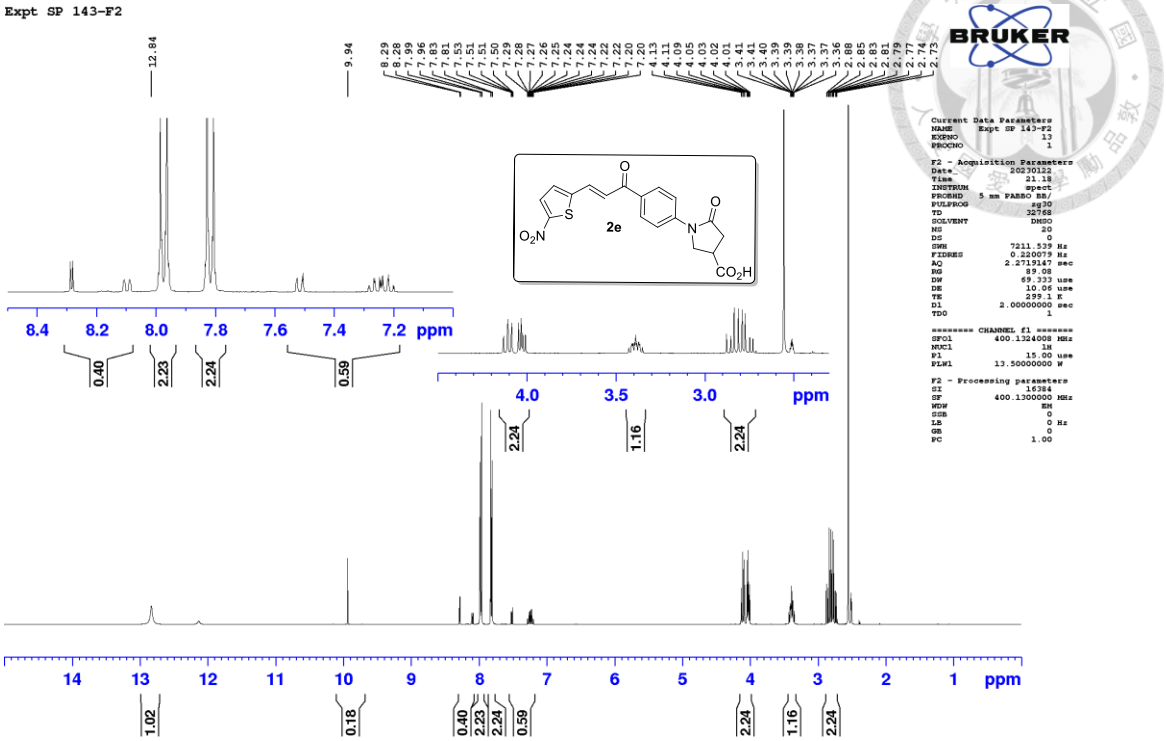

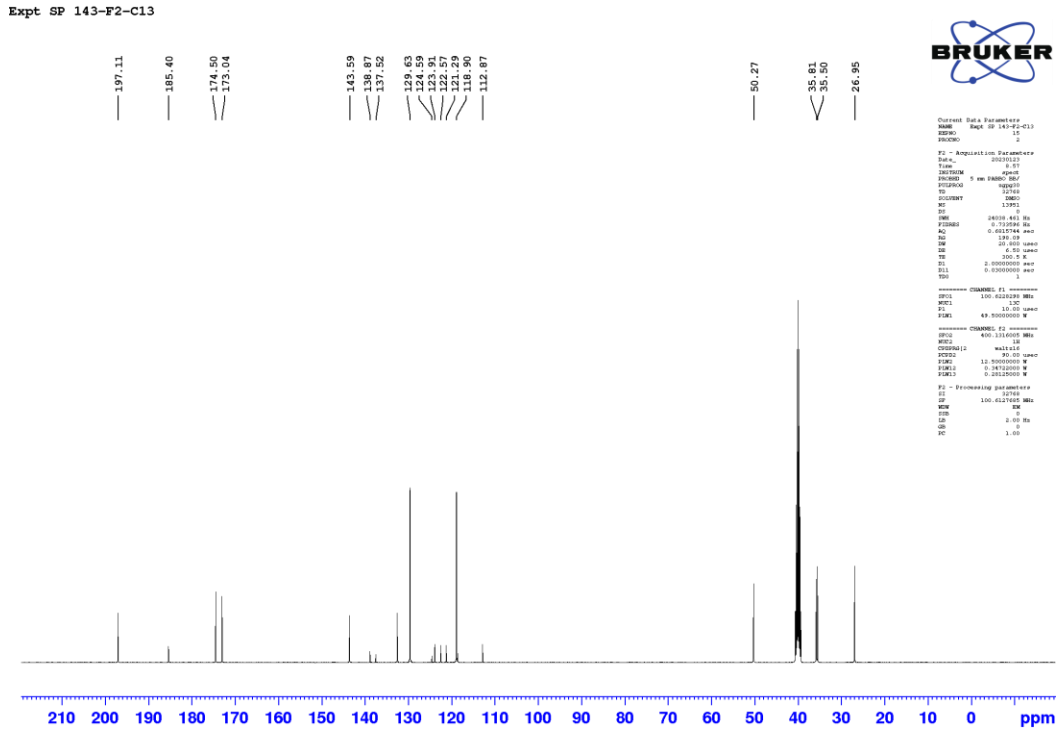

doi:10.6342/NTU202400256

2f (81)

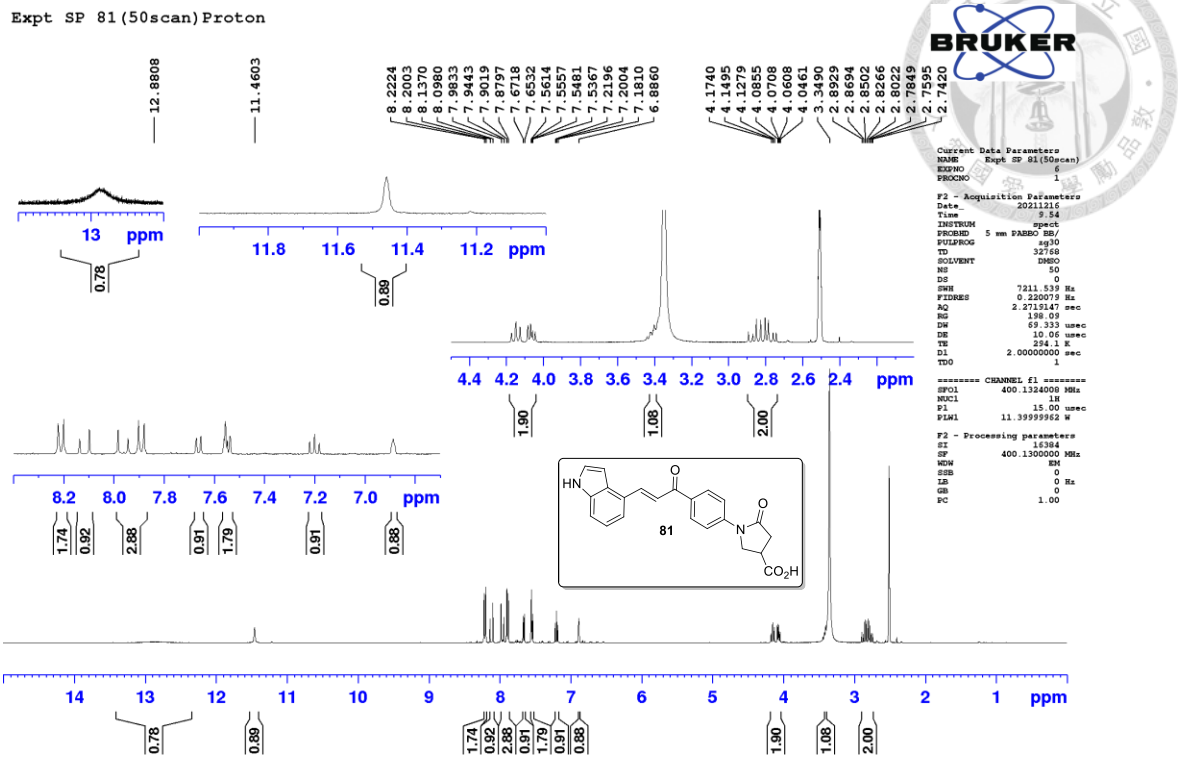

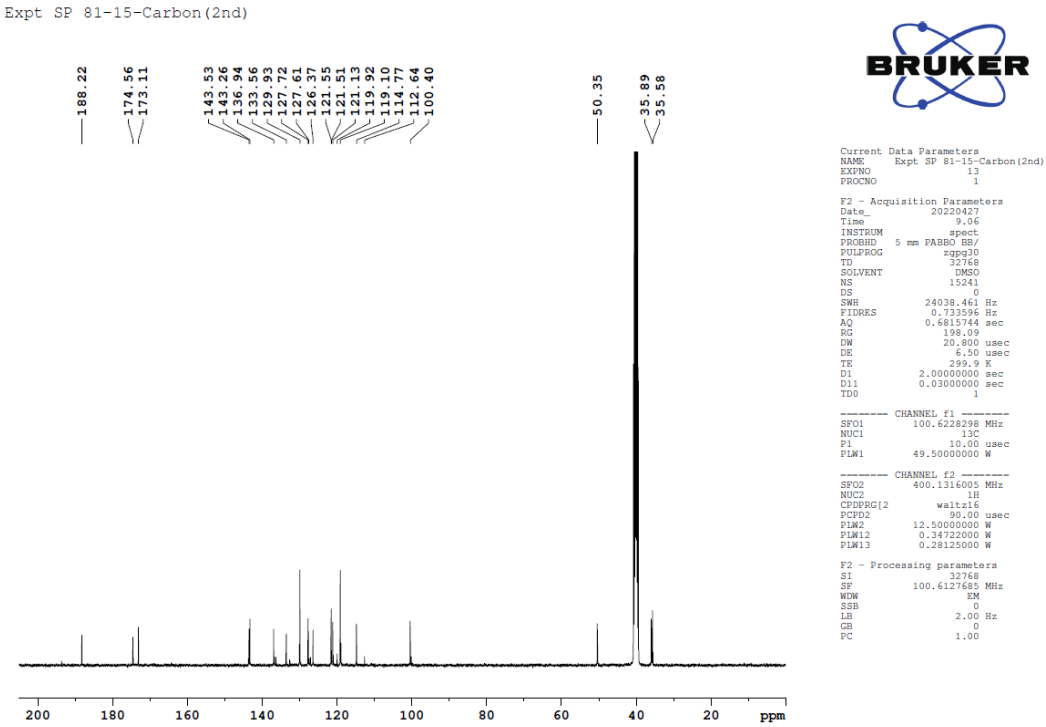

doi:10.6342/NTU202400256

2g (321)

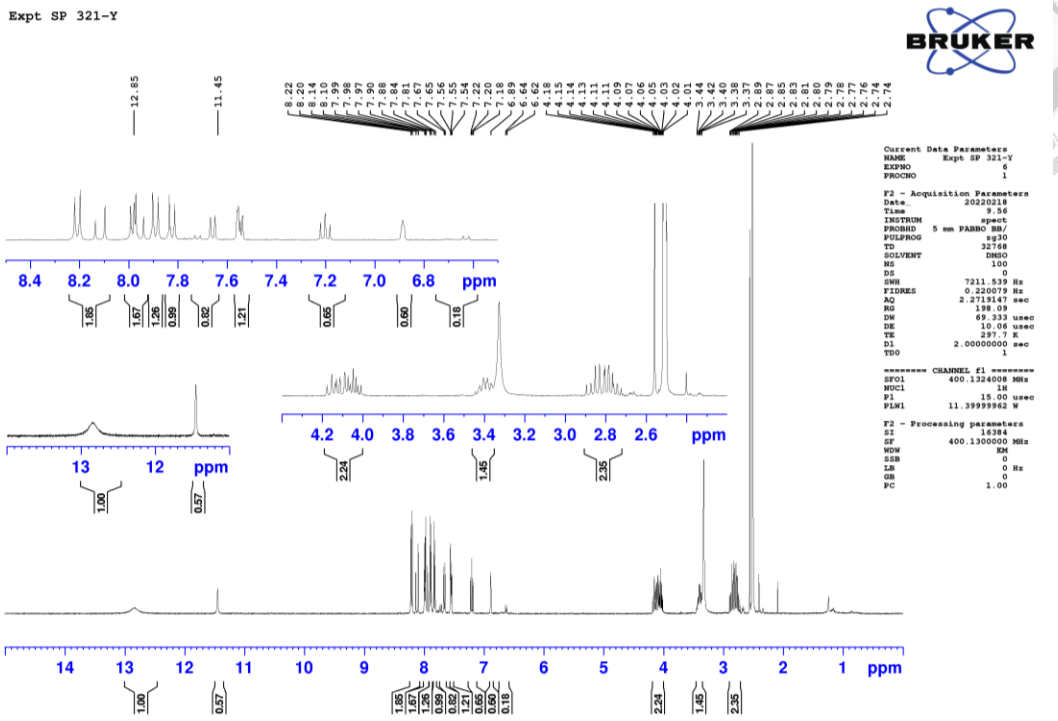

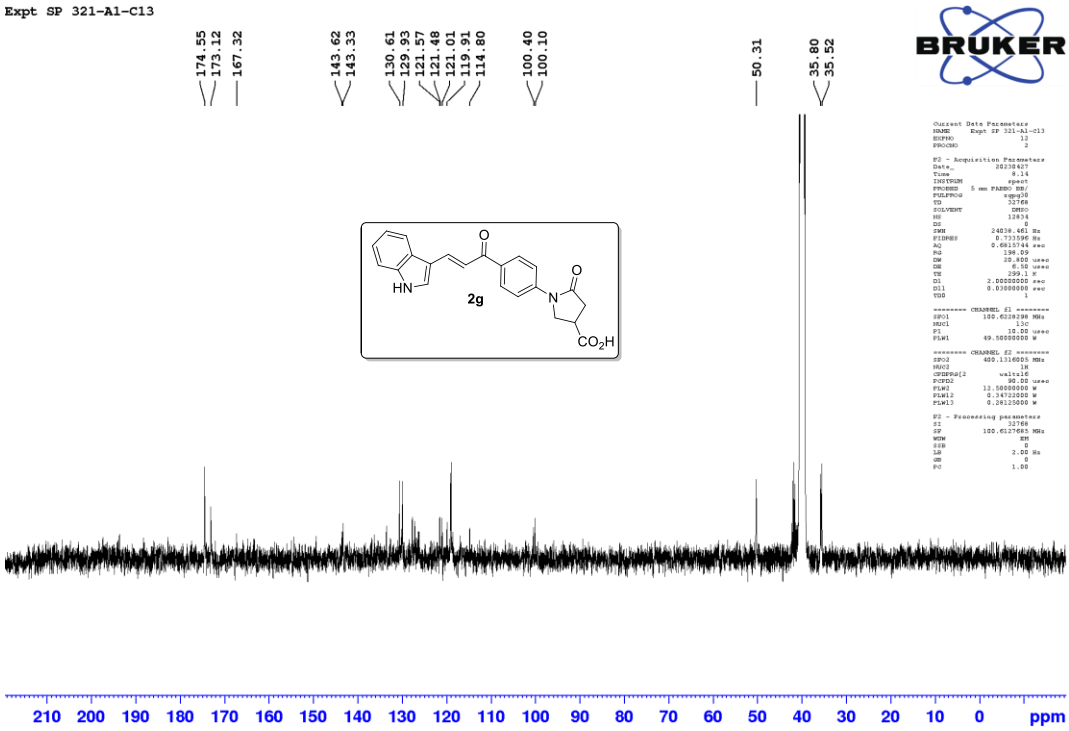

doi:10.6342/NTU202400256

3

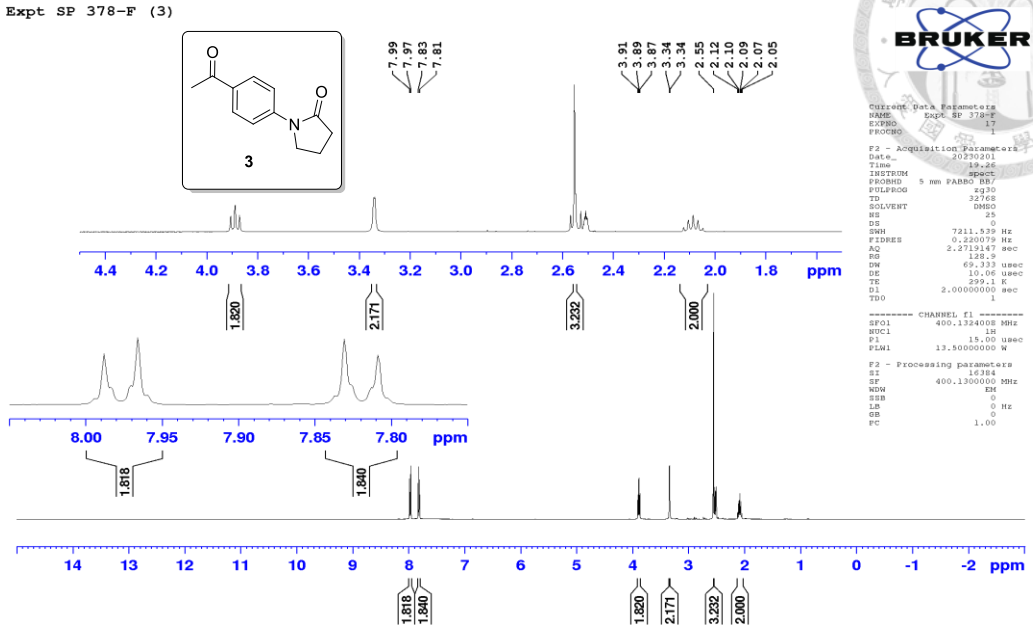

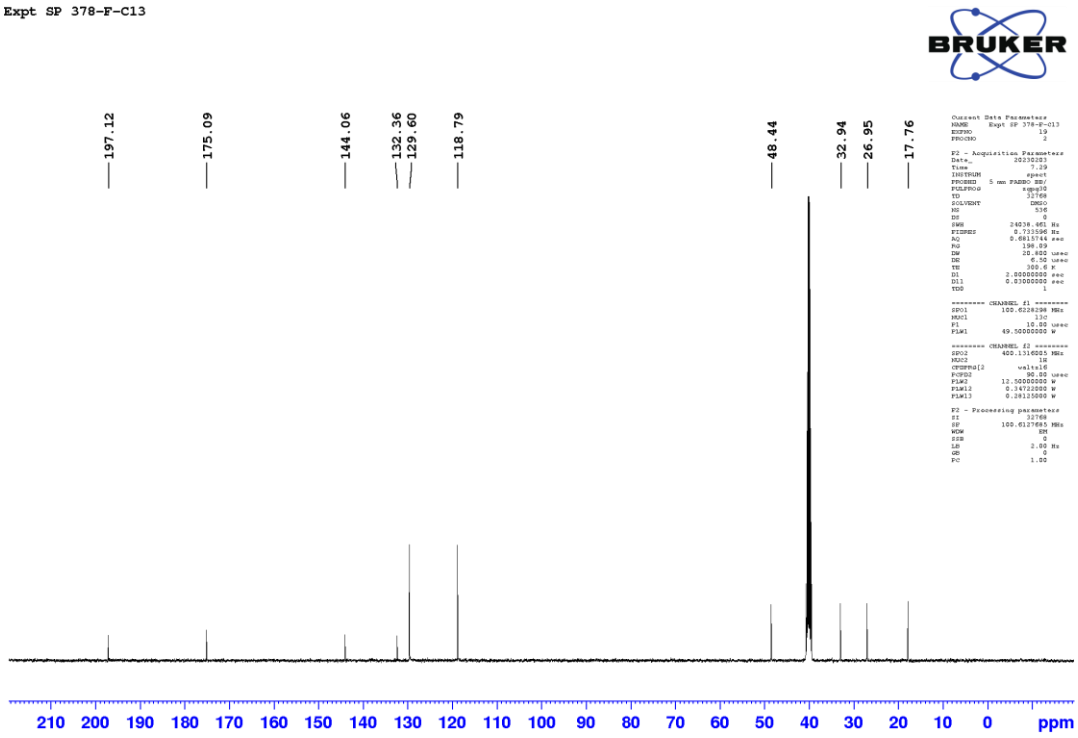

doi:10.6342/NTU202400256

4a (180)

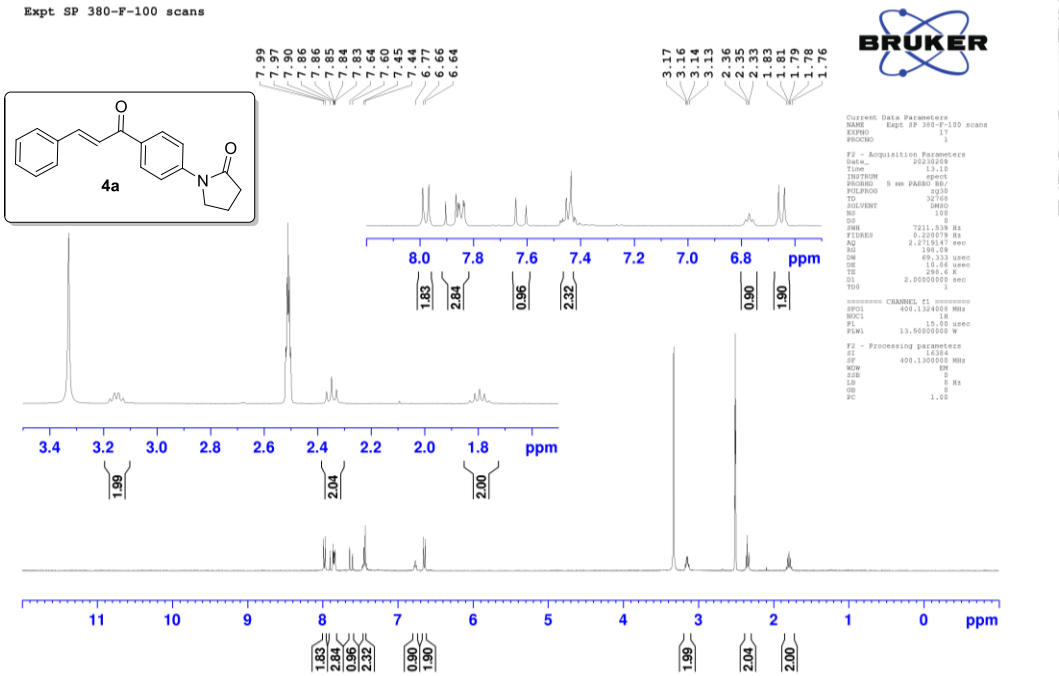

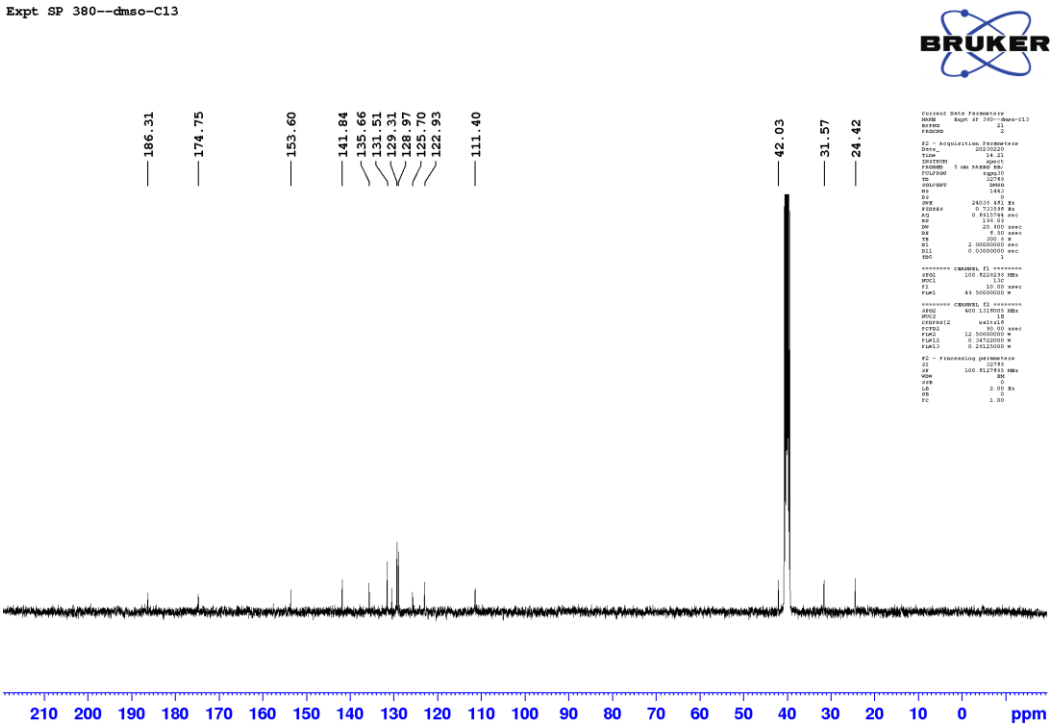

doi:10.6342/NTU202400256

4b (285)

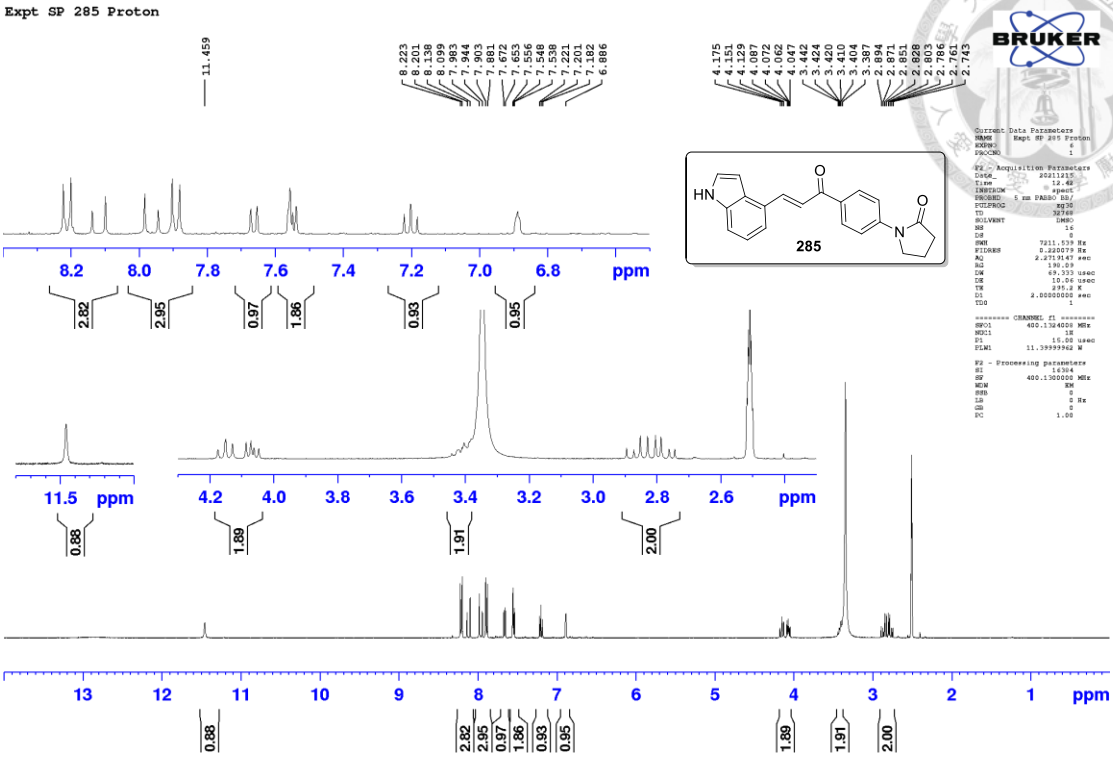

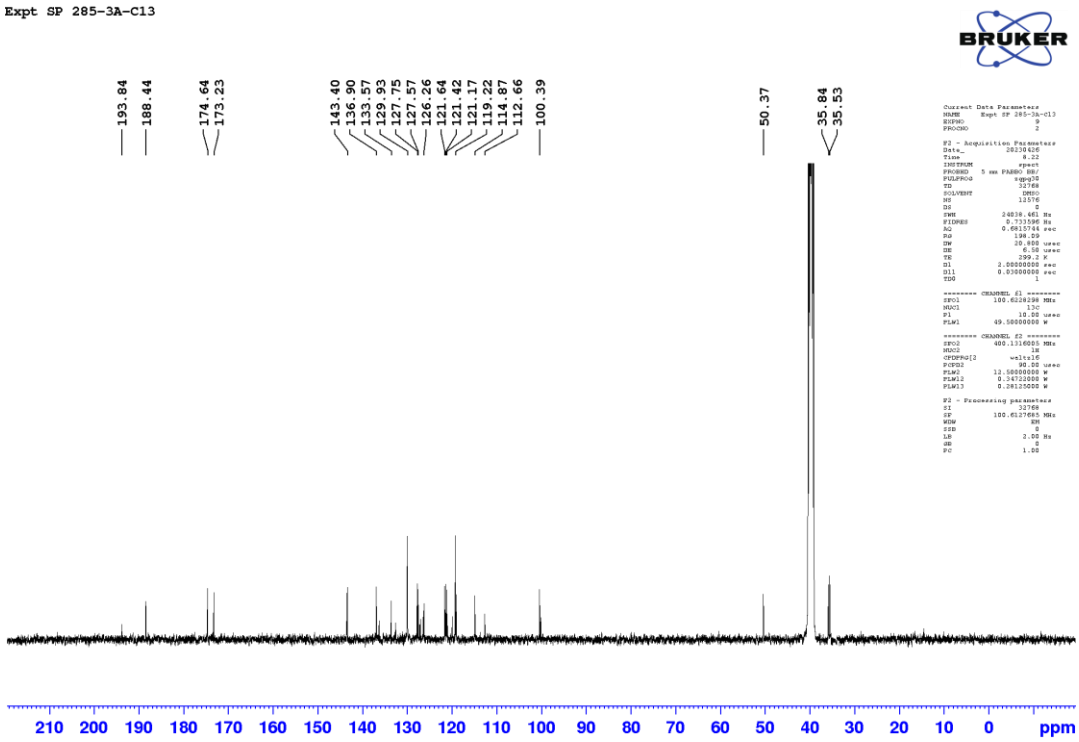

doi:10.6342/NTU202400256

219

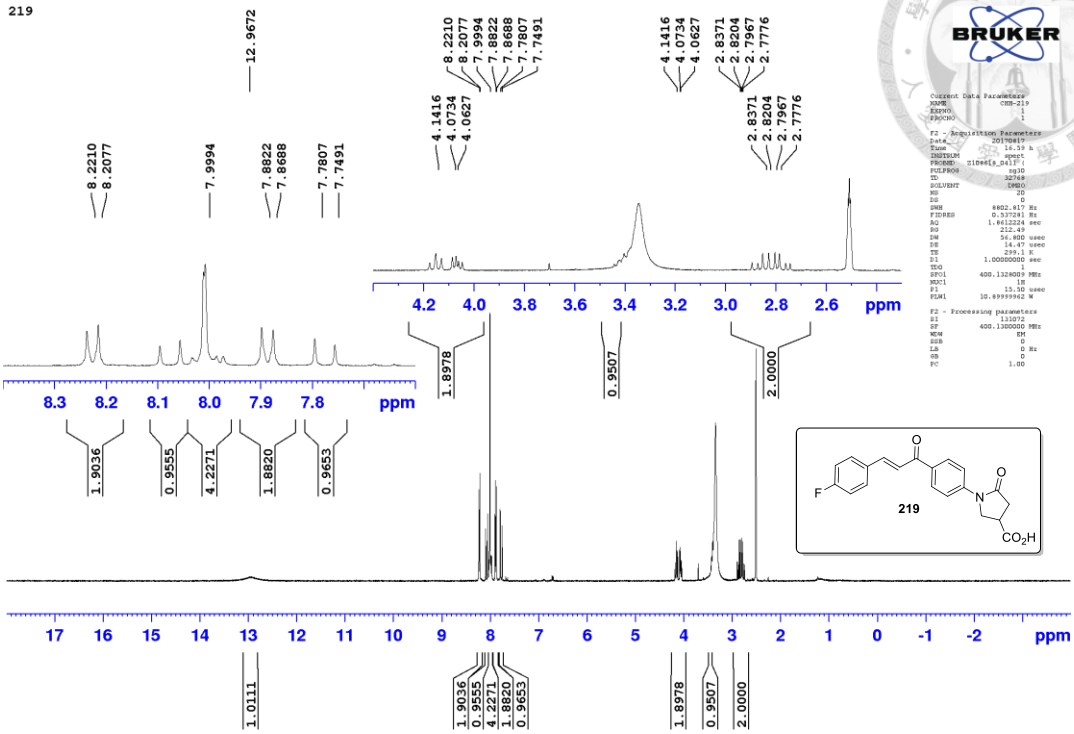

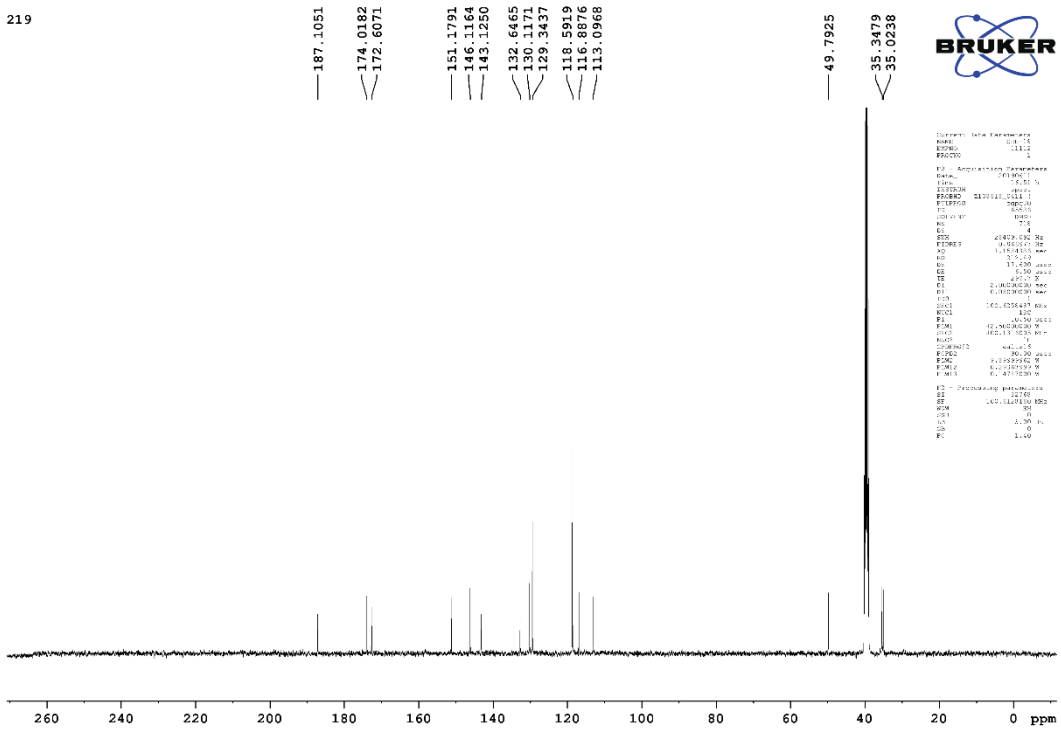

doi:10.6342/NTU202400256

101

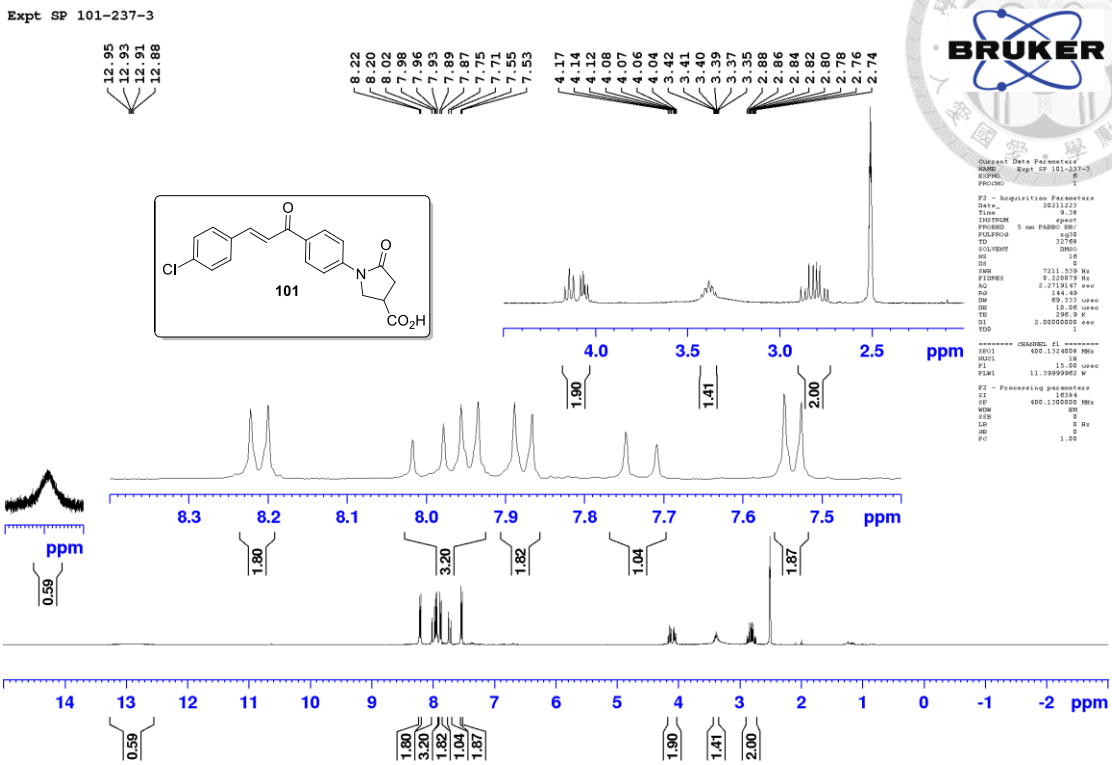

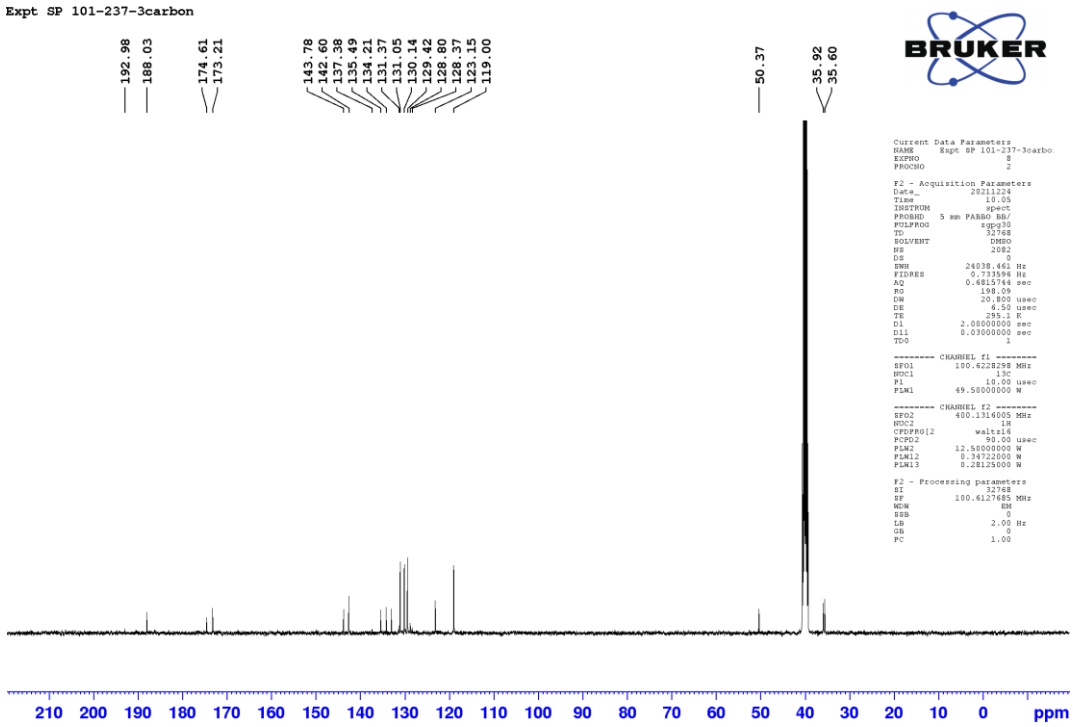

doi:10.6342/NTU202400256

91

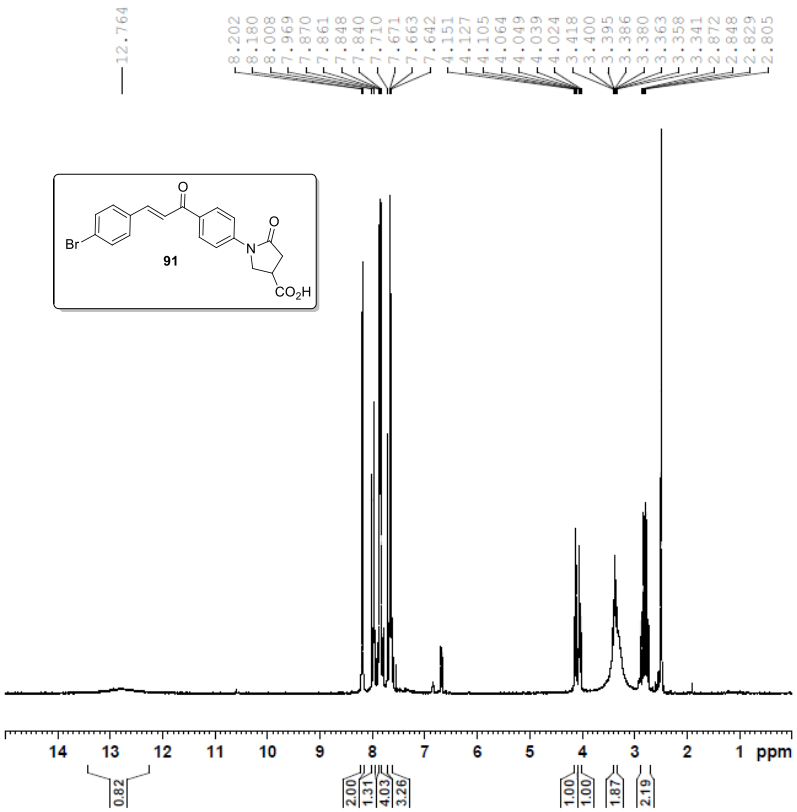

Current Data Parameters
NAME compound 2d
EXPNO 111
PROCNO 1

F2 - Acquisition Parameters
Date_ 20180123
Time 16.47 h
INSTRUM spect
PROBHD Z108618_0411 (
PULPROG zg30
TD 32768
SOLVENT DMSO
NS 20
DS 0
SWH 8802.817 Hz
FIDRES 0.537281 Hz
AQ 1.8612224 sec
RG 188.2
DW 56.800 usec
DE 14.47 usec
TE 298.6 K
D1 1.00000000 sec
TD0 1
SFO1 400.1328009 MHz
NUC1 1H
P1 15.50 usec
PLW1 10.89999962 W

F2 - Processing parameters
SI 131072
SF 400.1300078 MHz
WDW EM
SSB 0
LB 0 Hz
GB 0
PC 1.00

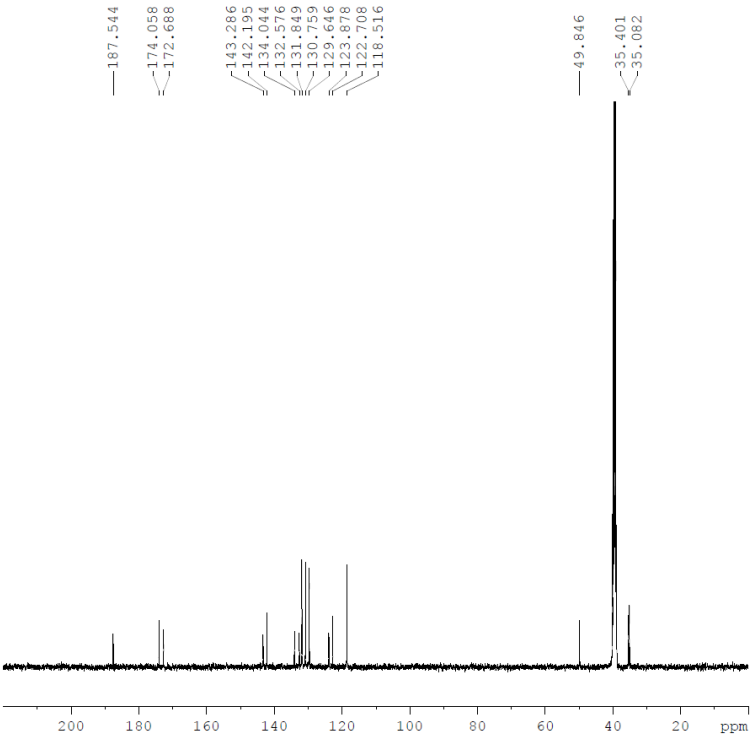

Current Data Parameters
NAME compound 2d
EXPNO 113
PROCNO 1

F2 - Acquisition Parameters
Date_ 20190508
Time 16.34 h
INSTRUM spect
PROBHD Z108618_0411 (
PULPROG zgpg30
TD 65536
SOLVENT DMSO
NS 500
DS 4
SWH 28409.092 Hz
FIDRES 0.866977 Hz
AQ 1.1534336 sec
RG 212.49
DW 17.600 usec
DE 6.50 usec
TE 297.8 K
D1 2.00000000 sec
D11 0.03000000 sec
TD0 1
SFO1 100.6258487 MHz
NUC1 13C
P1 10.50 usec
PLW1 42.50000000 W
SFO2 400.1316005 MHz
NUC2 1H
CPDPRG[2 waltz16
PCPD2 90.00 usec
PLW2 9.89999962 W
PLW12 0.29363999 W
PLW13 0.14747000 W

F2 - Processing parameters
SI 32768
SF 100.6128179 MHz
WDW EM
SSB 0
LB 3.00 Hz
GB 0
PC 1.40

doi:10.6342/NTU202400256

400

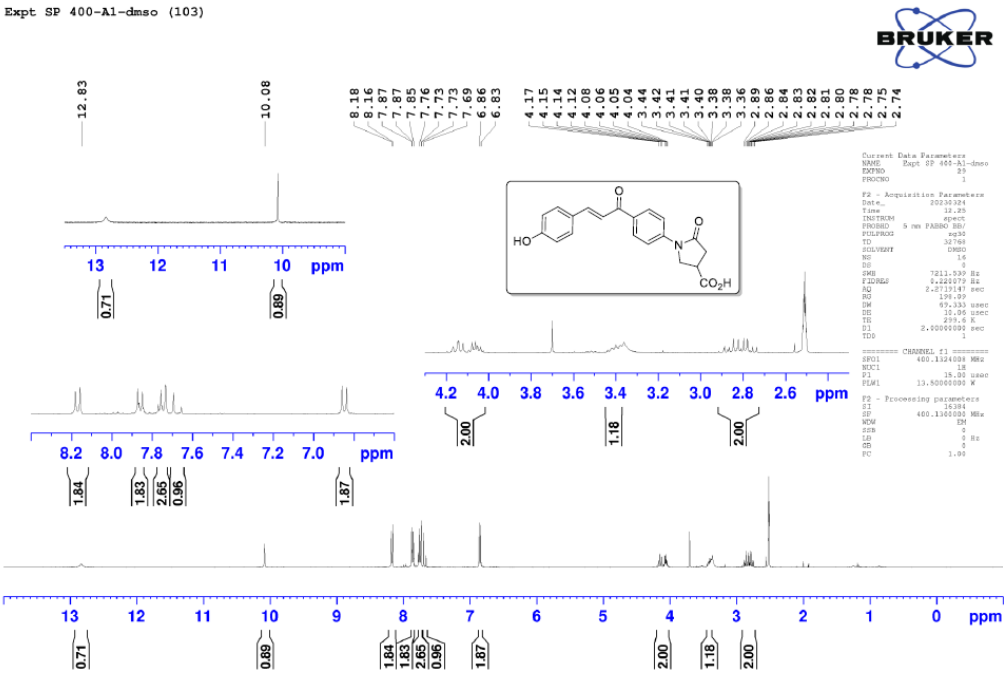

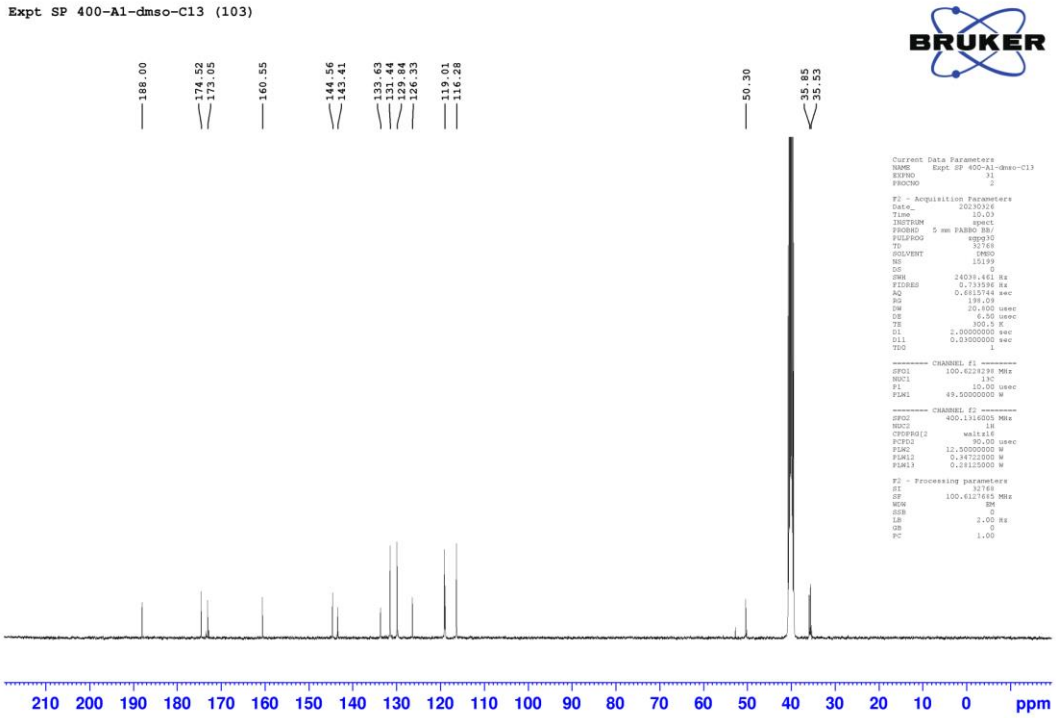

doi:10.6342/NTU202400256

221

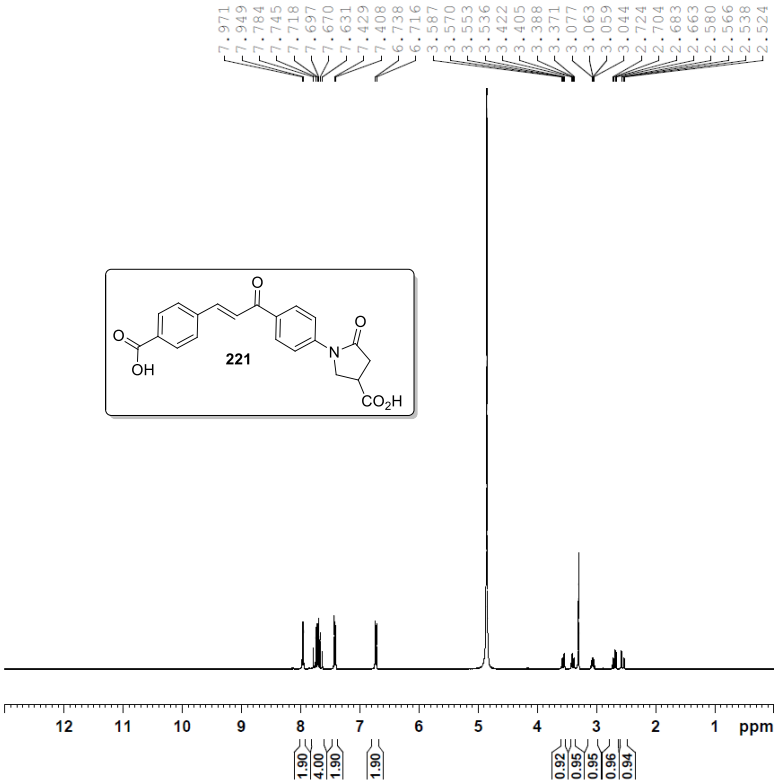

Current Data Parameters
NAME compound 2e
EXPNO 11
PROCNO 1

F2 - Acquisition Parameters
Date_ 20170922
Time 16.04 h
INSTRUM spect
PROBHD Z108618_0411 (
PULPROG zg30
TD 32768
SOLVENT MeOD
NS 20
DS 0
SWH 8802.817 Hz
FIDRES 0.537281 Hz
AQ 1.8612224 sec
RG 188.2
DW 56.800 usec
DE 14.47 usec
TE 299.0 K
D1 1.00000000 sec
TD0 1
SFO1 400.1328009 MHz
NUC1 1H
P1 15.50 usec
PLW1 10.89999962 W

F2 - Processing parameters
SI 131072
SF 400.1300121 MHz
WDW EM
SSB 0
LB 0 Hz
GB 0
PC 1.00

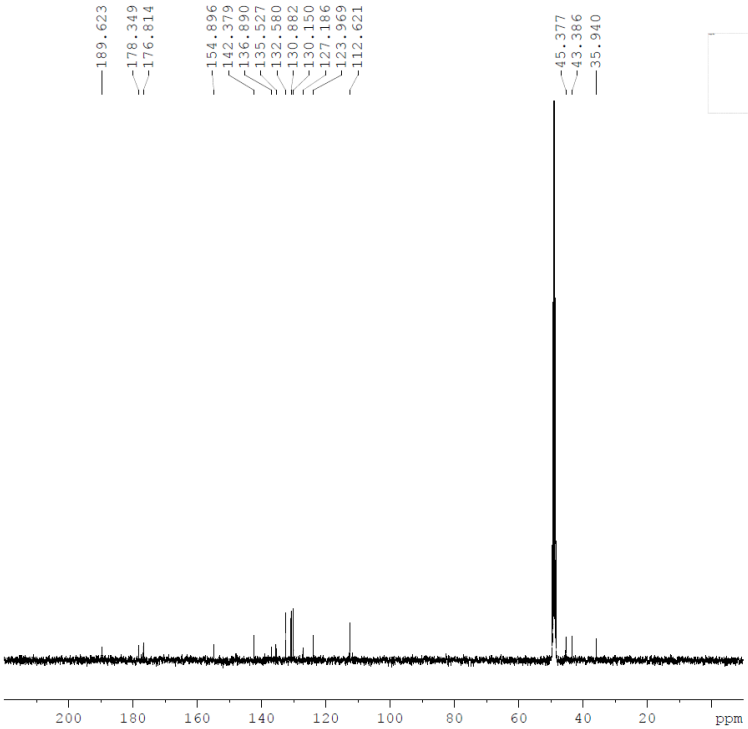

Current Data Parameters
NAME compound 2e
EXPNO 22
PROCNO 1

F2 - Acquisition Parameters
Date_ 20170922
Time 17.01 h
INSTRUM spect
PROBHD Z108618_0411 (
PULPROG zgpg30
TD 65536
SOLVENT MeOD
NS 443
DS 4
SWH 28409.092 Hz
FIDRES 0.866977 Hz
AQ 1.1534336 sec
RG 212.49
DW 17.600 usec
DE 6.50 usec
TE 299.3 K
D1 2.00000000 sec
D11 0.03000000 sec
TD0 1
SFO1 100.6258487 MHz
NUC1 13C
P1 10.50 usec
PLW1 47.29999924 W
SFO2 400.1316005 MHz
NUC2 1H
CPDPRG[2 waltz16
PCPD2 90.00 usec
PLW2 10.89999962 W
PLW12 0.32330000 W
PLW13 0.16236000 W

F2 - Processing parameters
SI 32768
SF 100.6126279 MHz
WDW EM
SSB 0
LB 3.00 Hz
GB 0
PC 1.40

doi:10.6342/NTU202400256

182

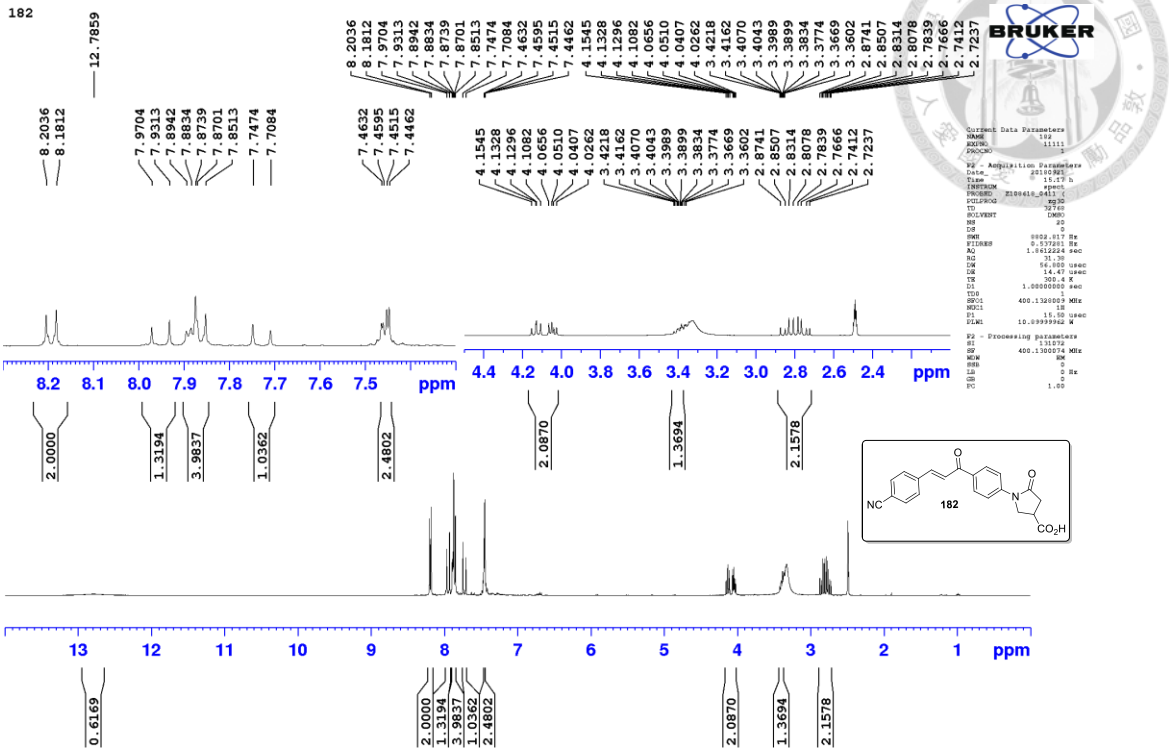

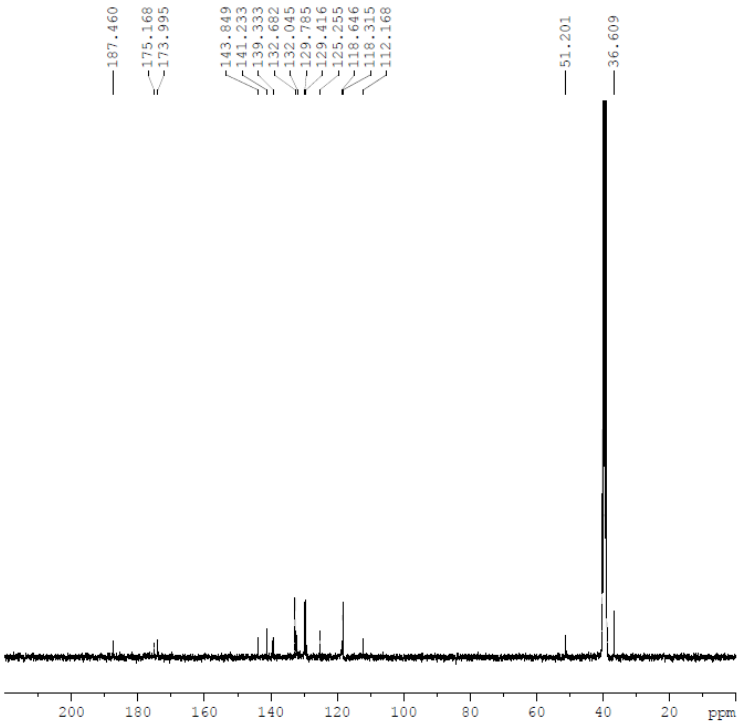


```
Current Data Parameters
NAME          compound 2f
EXPNO               11112
PROCNO                  1

F2 - Acquisition Parameters
Date_            20190507
Time                17.47 h
INSTRUM             spect
PROBHD   Z108618_0411 (
PULPROG           zgpg30
TD                 65536
SOLVENT             DMSO
NS                   700
DS                     4
SWH            28409.092 Hz
FIDRES          0.866977 Hz
AQ            1.1534336 sec
RG                212.49
DW                17.600 usec
DE                  6.50 usec
TE                297.6 K
D1            2.00000000 sec
D11           0.03000000 sec
TD0                    1
SFO1         100.6258487 MHz
NUC1                 13C
P1                 10.50 usec
PLW1         42.50000000 W
SFO2         400.1316005 MHz
NUC2                  1H
CPDPRG[2          waltz16
PCPD2             90.00 usec
PLW2          9.89999962 W
PLW12         0.29363999 W
PLW13         0.14747000 W

F2 - Processing parameters
SI                 32768
SF           100.6128187 MHz
WDW                   EM
SSB       0
LB                  3.00 Hz
GB        0
PC                  1.40
```


doi:10.6342/NTU202400256

118

Expt SP 31-F2-H1

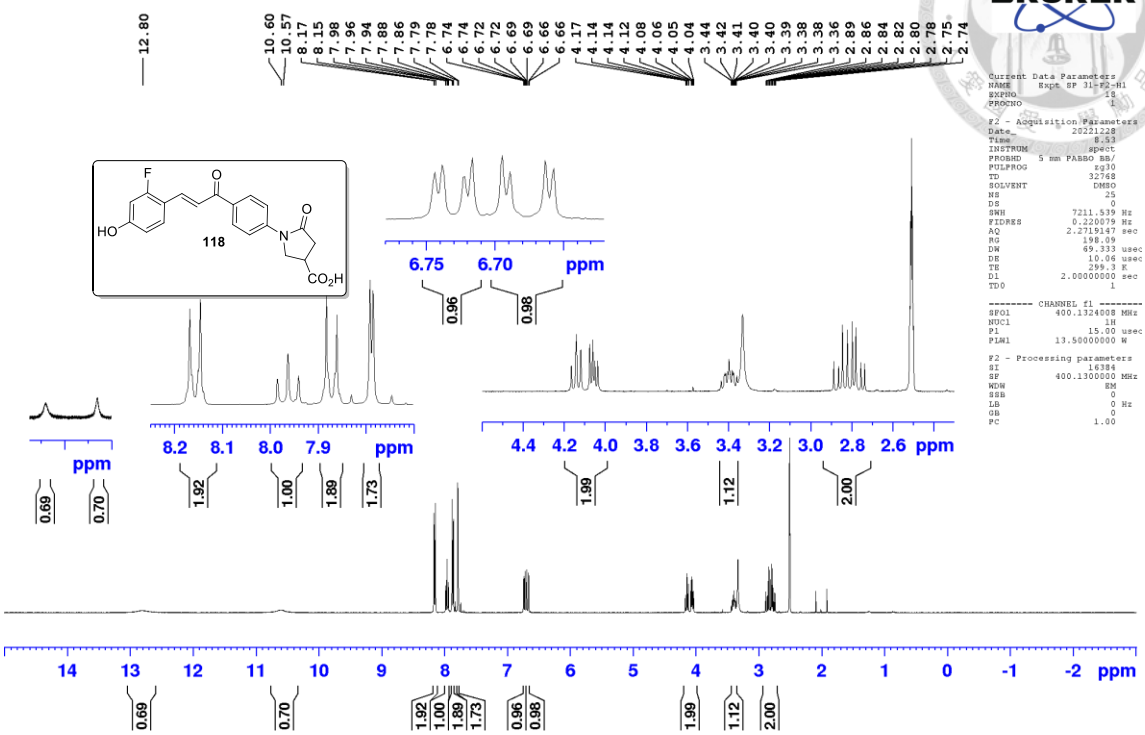

Expt SP 31-F2-C13

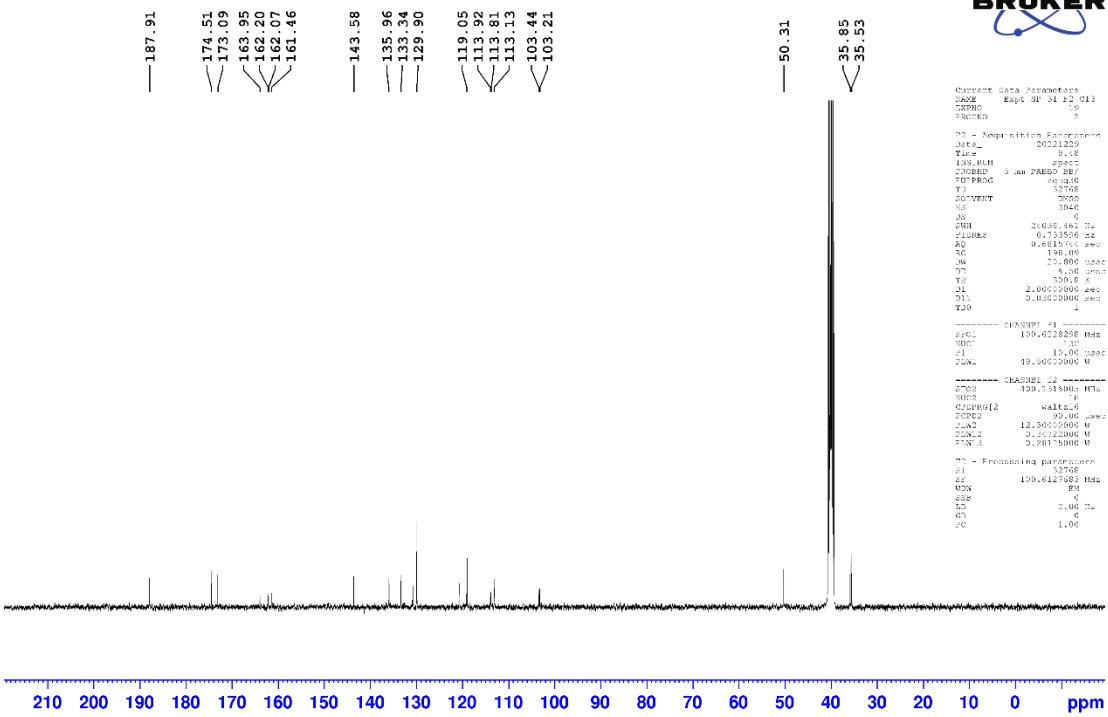

doi:10.6342/NTU202400256

452

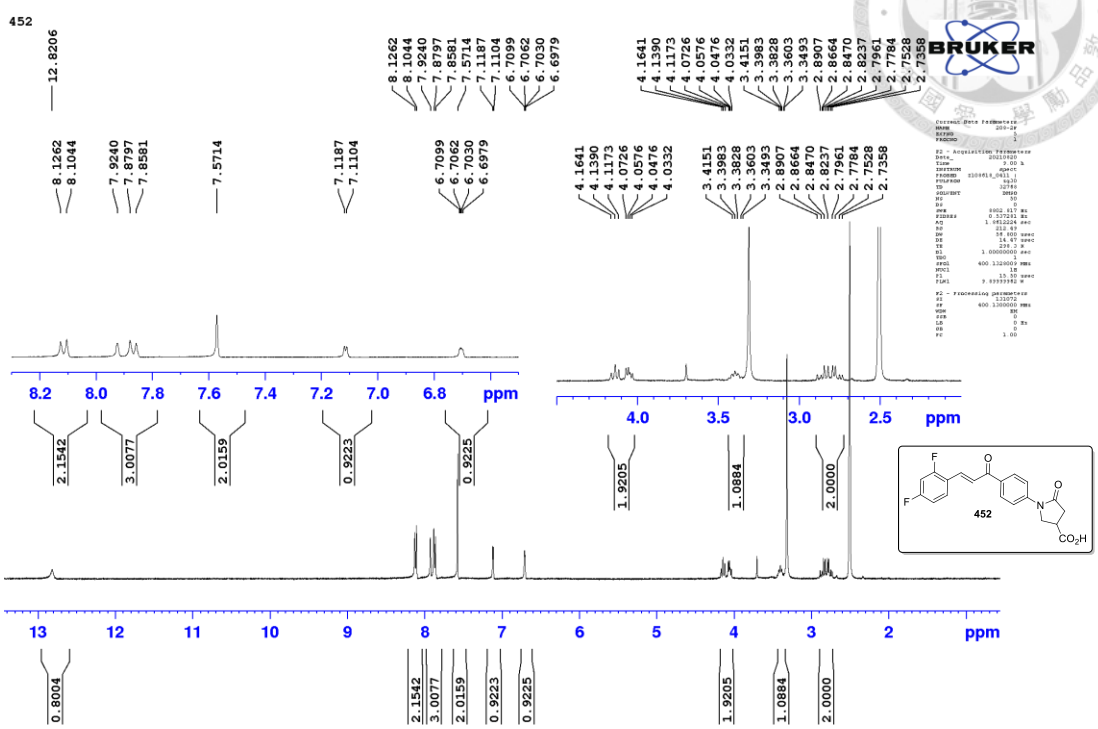

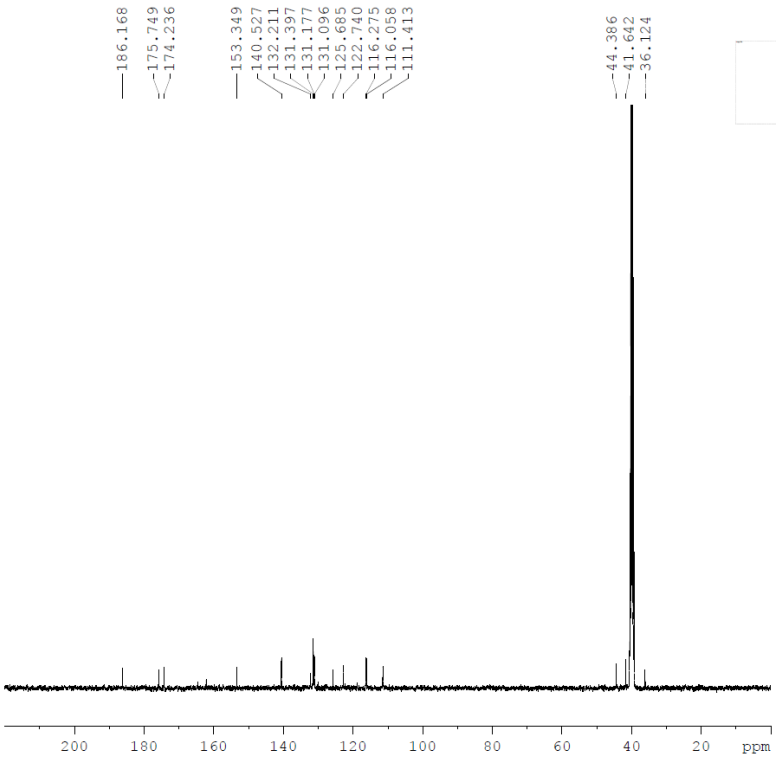


```
Current Data Parameters
NAME          compound 2b
EXPNO                 12
PROCNO                 1

F2 - Acquisition Parameters
Date_           20190505
Time               10.36 h
INSTRUM            spect
PROBHD   Z108618_0411 (
PULPROG          zgpg30
TD                65536
SOLVENT            DMSO
NS                   500
DS                     4
SWH           28409.092 Hz
FIDRES         0.866977 Hz
AQ            1.1534336 sec
RG               212.49
DW               17.600 usec
DE                 6.50 usec
TE                297.8 K
D1           2.00000000 sec
D11          0.03000000 sec
TD0                    1
SFO1        100.6258487 MHz
NUC1                 13C
P1                10.50 usec
PLW1        42.50000000 W
SFO2        400.1316005 MHz
NUC2                  1H
CPDPRG[2        waltz16
PCPD2             90.00 usec
PLW2         9.89999962 W
PLW12        0.29363999 W
PLW13        0.14747000 W

F2 - Processing parameters
SI                32768
SF          100.6127792 MHz
WDW                  EM
SSB       0
LB                3.00 Hz
GB        0
PC                1.40
```


doi:10.6342/NTU202400256

456

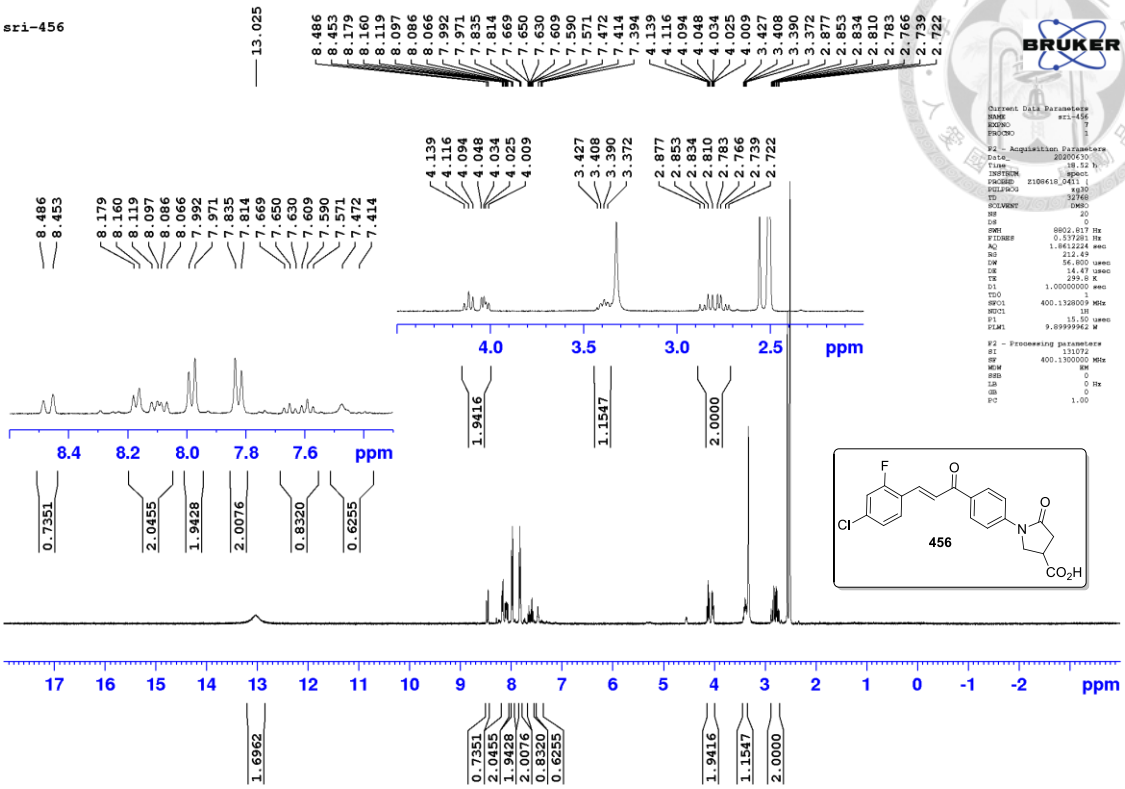

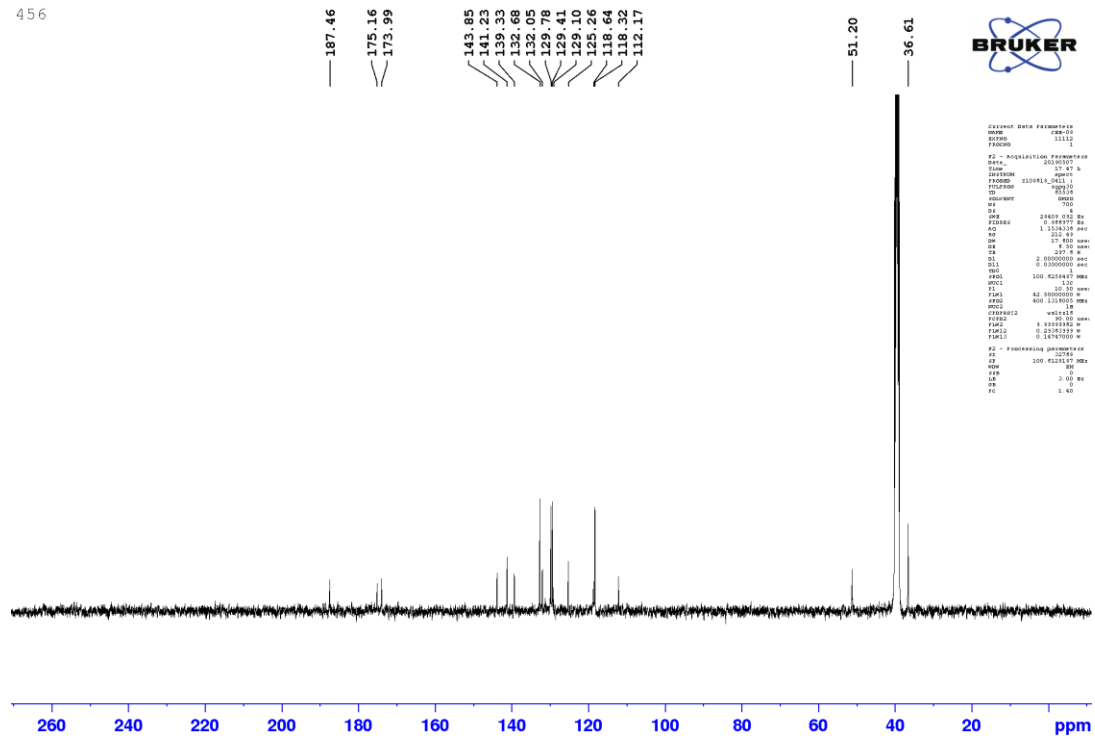

doi:10.6342/NTU202400256

List of Publications

1. **Palla. S. R.**; Li, C. W.; Chao, T. L.; Lo, H. L. V.; Liu, J. J.; Pan, M. Y. C.; Chiu, Y. T.; Lin, W. C.; Hu, C. W.; Yang, C. M.; Chen, Y. Y.; Fang, J. T.; Lin, S. W.; Lin, Y. T.; Lin, H. C.; Kuo, C.J.; Wang, L. H. C.; Chang, S. Y.; Liang, P. H. Synthesis, Evaluation, and Mechanism of 1-(4-(Arylethylenylcarbonyl)phenyl)-4-Carboxy-2-Pyrrolidinones as Potent Reversible SARS-CoV-2 Entry Inhibitors. Antiviral Res. **2023**, *219*, 105735, DOI: 10.1016/j.antiviral.2023.105735.

Note for the originality of this thesis

Most of the results mentioned in this thesis Part-I have been published in the paper "Synthesis, Evaluation, and Mechanism of 1-(4-(Arylethylenylcarbonyl)phenyl)-4-Carboxy-2-Pyrrolidinones as Potent Reversible SARS-CoV-2 Entry Inhibitors" where I served as the first author.

doi:10.6342/NTU202400256